TU Clausthal

Materialwissenschaft und
Werkstofftechnik

Band 1/03

Mohamed Soliman

Phase Transformation and Mechanical Properties of New Austenite-Stabilised Bainite Steels

Professor Dr.-Ing. Heinz Palkowski
Werkstoffumformung

Institut für Metallurgie

Phase Transformation and Mechanical Properties of New Austenite-Stabilised Bainite Steels

Dissertation

Zur Erlangung des Grades eines Doktors
der Ingenieurwissenschaften

vorgelegt von

Mohamed A. Soliman

aus Gizeh / Ägypten

genehmigt von der
Fakultät für Natur- und Materialwissenschaftlichen
der Technischen Universität Clausthal

Tag der mündlichen Prüfung:

26.11.2007

Soliman, Mohamed
Phase Transformation and Mechanical Properties
of New Austenite-Stabilised Bainite Steels
Mohamed Soliman – Clausthal-Zellerfeld – 2008
Druck & Verlag: Piepersche Druckerei & Verlag GmbH
Zugl.: Clausthal, Technische Universität, Dissertation 2007

CIP-Titelaufnahme der Deutschen Bibliothek
ISBN 3-923605-58-7

Bibliografische Information der Deutschen Bibliothek
Die Deutsche Bibliothek verzeichnet diese Publikation in
der Nationalbibliografie; detaillierte Bibliografische Daten
sind im Internet über http://dnb.ddb.de abrufbar.

Vorsitzender der Prüfungskommission:	Professor Dr.-Ing. Lothar Wagner
Hauptberichterstatter:	Professor Dr.-Ing. Heinz Palkowski
Berichterstatter:	Professor Dr.-Ing. Wolfgang Bleck
	Professor Dr.-Ing. Nabil Fatahalla

D 104

1. Auflage 2008

ISBN 3-923605-58-7

Bezugsadresse: Professor Dr.-Ing. Heinz Palkowski
Werkstoffumformung
Institut für Metallurgie (IMET)
Technische Universität Clausthal
Robert-Koch-Str. 42
38678 Clausthal-Zellerfeld

Acknowledgements

I would like to express my sincere thanks to my supervisor Prof. Dr.-Ing. H. Palkowski for his strong support, guidance and giving me the opportunity to pursue my Ph.D. degree at TU-Clausthal.

I acknowledge the financial support from DAAD, Deutsche Akademische Austauschdienst, for providing me the opportunity to perform the research during the first two years.

This work is dedicated to the soul of Dr. Ibrahim Moustafa with his help I got the DAAD scholarship and with his help I cast a part of the research-material at CMRDI-Egypt.

I would like to express my deep gratitude to Prof. Dr.-Ing. Wolfgang Bleck and Prof. Dr.-Ing. Nabil Fatahalla for agreeing to be on my thesis committee despite their extremely busy schedules and the long travelling-distance.

This thesis would not be what it is without the help and cooperation of the technicians of the Institute of Metallurgy at TU-Clausthal. Particularly, I would like to thank Herr Schubert, Ernst, Mathias, Mr. Brinkhaus, Mr. Dittelbach, Mrs. Lenk and Mr. Koch.

I owe thanks to Prof. Dr.-Ing. K.-H. Spitzer for providing the facilities of the casting laboratory and to Dr.-Ing. Bernd Weidenfeller and Dipl-Ing. Mathias Anhalt for the help in the magnetic measurements.

I will never forget the first metallurgical experiences that I got under the supervision of Prof. Dr.-Ing. Nabil Fatahalla during the master work.

I would like to express my thanks to the past and present colleagues at the institute for metallurgy for their continuous help, friendship and kindness.

I am greatly appreciating the patience, understanding and support of my parents and parents-in-law during these busy years.

Finally, I record my deep sense of appreciation for my wife, Enas, for relentless supporting in spite of all the hardship.

Table of Contents

Nomenclature

a.u.	Arbitrary unit
A/M	Austenite and martensite
Ac1	Temperature at which austenite begins to be formed when heating up
Ac3	Temperature at which the transformation of ferrite to austenite is completed when heating up
Ae1	Temperature separating α and $\alpha+\gamma$ phase fields under equilibrium
Ae3	Temperature separating $\alpha+\gamma$ and γ phase fields under equilibrium
Ar1	Temperature at which conversion of austenite to ferrite or to ferrite plus cementite is completed when cooling steel
Ar3	Temperature at which austenite begins to convert to ferrite when cooling steel
a_α	Ferrite lattice parameter
a_γ	Austenite lattice parameter
bcc	Body-centred cubic
$\overline{C}$	Alloy average carbon concentration
CCT	Continues cooling transformation
CHT	Continues heating transformation
C_γ	Retained austenite carbon concentration
d	Lattice interplanner spacings
d_f	Polygonal ferrite grain size
DRX	Dynamic recrystallisation
F	Structure factor
fcc	Face-centred cubic
Fer. %	Polygonal ferrite percentage
f_{fe}	Atomic scattering factor of iron
f_γ	Intercritical austenite volume fraction

H	Applied magnetic field
HF	High frequency
hkl	Miller indices
l_α	Coefficient of thermal expansion of α phase
l_γ	Coefficient of thermal expansion of γ phase
I_i^γ	Integrated intensity of γ phase at hkl reflection
I_i^α	Integrated intensity of α phase at hkl reflection
J	Measured polarisation
J_s	Saturation polarisation
J_s^A	Saturation polarisation of the specimen with retained austenite
J_s^{alloy}	Saturation polarisation of austenite-free specimen containing certain amount of alloying elements
l	Length
LOM	Light optical microscope
L_p	Lorentz-polarisation factor
L_t	Mean linear intercept through the bainite plates
LVDT	Linear variable differential transducer
MDRX	Metadynamic recrystallisation
MFS	Mean flow stress
M_S	Martensite-start
norm. Δl	Normalised change in length
PF	Polygonal ferrite
R_e	Yield strength or 0.2% proof stress in case of absence of yield point
R_m	Ultimate tensile strength
RT	Room temperature
R_i^γ	Relative intensity of γ phase at hkl reflection
R_i^α	Relative intensity of α phase at hkl reflection

s	Carbon concentration in the bainitic ferrite
Schedule-P	Hot-rolling schedule results in microstructure formed from the pancaked-austenite
Schedule-R	Hot-rolling schedule results in microstructure formed from the recrystallised-austenite
Schedule-RP	Hot-rolling schedule results in microstructure formed from the recrystallised- and then pancaked-austenite
SEM	Scanning electron microscope
SRX	Static recrystallisation
STM	Scanning tunnel microscope
t	Thickness of bainite plate
T_0	Temperature at which both bainitic ferrite and austenite of similar composition have identical free energy
T'_0	Same as T_0, but considering the stored energy in bainite
T_A	Annealing temperature
T_B	Isothermal bainitic transformation temperature
T_c	Temperature in the intercritical region at which carbides entirely dissolve
T_{CU}	Curie temperature
TEl%	Total elongation (%)
TEM	Transmission electron microscope
T_{nRX}	Temperature of non-recrystallisation
TRIP	Transformation induced plasticity
TTT	Time temperature transformation
2θ	Scanned range in degrees using X-ray diffraction
v	Volume of the unit cell
V_b	Bainitic ferrite volume fraction
V_γ	Retained austenite volume percentage
x_A	Austenite volume fraction

x_{Mn}	Manganese concentration
μ_0	Permeability of vacuum (the magnetic constant)
μ_r	Relative permeability of the material
$\Delta G^{\gamma\alpha}$	Driving force for bainite transformation
$\Delta l/l_0$	Relative change in length
$\Delta_{\gamma\alpha}$	Change in length resembling the dilatation if 100% austenite transforms into ferrite at a certain temperature.
α	Ferrite phase
α_b	Bainitic ferrite
ε_c	Critical strain where the onset of DRX is reached
γ	Austenite phase
γ_{hc}	High carbon austenite
γ_i	Intercritical austenite
γ_r	Retained austenite
λ	X-ray radiation wave length
ρ	Multiplicity factor
φ	True strain

Chapter 1
Introduction

In early 1965 Deliry reported that silicon strongly retards the precipitation of cementite during the bainite reaction [Del65]. Consequently, in silicon-alloyed steel the martensite start temperature "M_S" of carbon-enriched austenite may, after a certain transformation time, decrease to the level where the martensite formation during cooling from the transformation temperature is avoided. Thus, a certain amount of austenite can be stabilised to room temperature through the bainite transformation. This austenite is known as retained austenite.

More than 20 years later, Matsumura et al. [Mat87] reported the improvement of the mechanical properties of steels due to the transformation of the retained austenite into martensite during straining (TRIP effect). This was the first report concerning the low alloyed TRIP-aided steels. In these steels, the mechanically induced martensite transformation of the metastable austenite results in geometrical changes at the microscopic level; these geometrical changes have the effect of strain hardening of the surrounding ferrite matrix. Consequently, the failure due to necking is shifted to higher values of stress and strain. In the past decade there has been a resurgence of interest in these steels, especially for use in the automotive industry [Uls01, Ble02].

More recently, another category of bainitic steels, which uses the bainitic stabilisation of austenite, in combination with high carbon content and low transformation temperature, has been developed. Due to their ultra-fine carbide-free structure, these steels are characterised by very high strength together with enhanced ductility [Cab02, Gar03a, Gar05].

It is of technological interest to exploit the full potential of these materials by optimisation of alloy and process design. This can be achieved by developing a clear understanding of their behaviour along the processing route of reheating, annealing, cooling and the bainitic transformation. Many metallurgical phenomena take place during these processing routes, such as recrystallisation, austenite formation and austenite decomposition. Knowledge of the kinetics of these metallurgical phenomena allows control of the microstructure by controlling the processing conditions. This is of prime interest because the properties of steels are, to a great extent, determined by their microstructure

which is a result of various phase transformations occurring during manufacturing.

This work helps to achieve better understanding of the microstructure development of the TRIP-aided and ultra-fine, carbide-free bainite steels throughout the entire integrated processing routes aimed at further development of these steels in terms of strength and ductility via affordable addition of alloying elements together with optimisation of the processing routes.

The outline of the present thesis is as follows:

Chapter 2 presents a literature review. The topics of review provide the basics for stabilisation of austenite by the bainite transformation. The retained austenite and the bainite characteristics and the characterisation methods of the multiphase steels are reviewed. A review on the chemistries' effects is also provided.

Chapter 3 describes the instrumentations and the experimental techniques used through out the current study.

Chapter 4 shows the experimental results of the aluminium-containing TRIP-aided steels and discusses the effect of the aluminium-content and the processing roots on both, the microstructure and the mechanical properties.

Chapter 5 presents the results of producing an ultra-fine carbide-free bainite structure in hypo-eutectoid steels. The effects of decreasing the carbon-content and the heat-treatments parameters on the microstructure and mechanical properties are discussed.

Chapter 6 gives a summary of the present work.

Chapter 2
Theoretical Background

2.1 Basics of Bainitic Stabilisation of Austenite

Bainite is the a non-equilibrium transformation product of austenite which is produced by cooling rates such that the diffusion-controlled transformation of pearlite are not possible, yet the cooling is sufficient slow to avoid the diffusionless transformation into athermal martensite [Bha2001]. This can be achieved by either continuous cooling or by austempering. Normally, bainite forms in two stages:

Stage I: $\gamma \rightarrow \gamma_{hc} + \alpha_b$

Stage II: $\gamma_{hc} \rightarrow \alpha_b + \text{carbides}$

where, γ_{hc} is high carbon austenite and α_b is bainitic-ferrite.

However, it had been reported that silicon strongly retards the precipitation of carbides during the bainite-reaction [Del65]. As the precipitation of carbides during the bainite-reaction is slow, the residual austenite becomes enriched in carbon. This can shift martensite start temperature (M_S) down to room temperature (RT) and hence a large proportion of γ_{hc} can be retained.

The effect of retained austenite in low carbon steels on the mechanical properties was not fully recognised until 1980's during which many studies demonstrated that retained austenite improves the mechanical properties of steels through the TRIP effect, if the stability of the retained austenite can be increased [Mat87]. Actually, the TRIP effect was originally observed in fully austenitic steels with sufficient Ni and Mn to maintain the M_S temperature below RT [Zac67]. In 1987, Matsumura et al. reported the potential of bainite in TRIP-aided carbide-free steels, where as a result of the transformation, austenite carbon-enrichment takes place [Mat87]. Depending on his result, expensive elements are no longer necessary to retain the austenite.

In summary the mechanism of TRIP is believed to be in that way that during plastic deformation some of the most severely strained portions of the material will transform to martensite by the action of the strain/stress. The martensite produced during straining prevents early failure due to necking, via stabilisation of the neck through increases in the strain hardening rate. This leads to an overall increase of both, tensile strength and elongation.

2.2 Retained Austenite Characteristics

2.2.1 Retained Austenite Morphology

Basuki et al. [Bas99a] have classified the morphology of retained austenite into granular type and needle-like types. The retained austenite can be designated by the location where it forms, between ferrite and bainite, surrounded by ferrite and surrounded by bainite. The needle-like retained austenite is between the bainite interlath regions. The different morphologies are shown in **Fig. 2.1**.

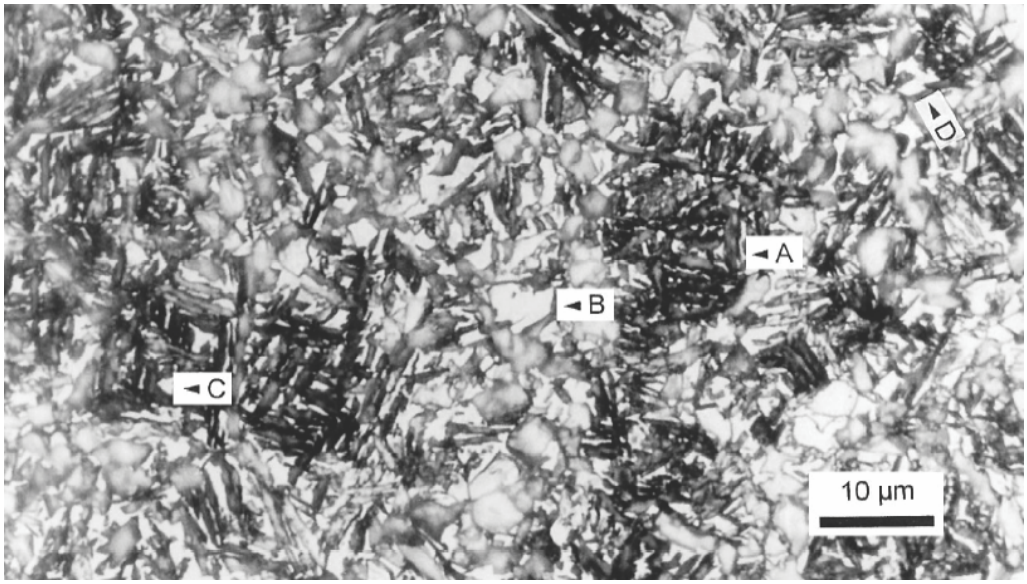

Fig. 2.1 Typical microstructure of TRIP steel ferrite: gray, bainite: black, retained austenite: white; A: Needle-like retained austenite, B: Granular retained austenite surrounded by the ferrite, C: Granular retained austenite enclosed by the bainite, D: Granular retained austenite in contact with bainite and ferrite [Bas99a].

2.2.2 Retained Austenite Stability

Austenite retained to ambient temperature after isothermal formation of bainitic-ferrite, especially the larger blocky austenite, can decompose to martensite even at relatively small stresses [Bha01]. The austenite, if decomposes under the influence of stress, can be detrimental to the steel since the resulting high-carbon, untempered martensite is expected to be brittle. The mechanical stability of retained austenite is therefore important in obtaining good toughness in bainitic steels. The parameters affecting the mechanical stability of the retained austenite which gives rise to the TRIP behaviour are particle size, morphology and solute enrichment.

a- Particle size: Small austenite particles are more stable than large particles. This has been explained by that a sufficiently small particle might not contain an effective martensite nucleation site [Rig79, Bra93].

b- Morphology: According to the classification of the retained austenite morphology and location (**Fig. 2.1**), the stability of the retained austenite can also be classified. The granular type surrounded by ferrite "type B" is unstable and can easily transform to martensite at the initial strain stage, so it has a little effect on enhancing the mechanical properties. The needle-like type "type A" is protected from the imposed stress by the surrounding hard phase; its deformation and transformation hardly occur. On the other hand, the other granular type retained austenite is stable enough to generate the TRIP effect of the retained austenite [Tim02, Bas99b].

c- Solute enrichment: The stability of the retained austenite is strongly related to the enrichment of C and Mn in the austenite, in other words the higher the solute enrichment the greater the stability is [Sak92, Tse87].

During steel making process, carbon content in the untransformed austenite increases because carbon diffuses to the remaining austenite during the intercritical annealing by transformation to ferrite and during austempering by transformation to bainite. Thus, together with the steel alloying elements, the processing parameters are also an important key-factor determining the retained austenite stability.

2.3 The Basics of Bainite

2.3.1 Bainite Definition

Bainite is a product of austenite decomposition in steels. It transforms either isothermally or during continuous cooling over a temperature range that is typically below that of the austenite-to-pearlite reaction and above M_S temperature for martensite formation. The transformation mechanisms applicable to bainite, and even the definition of bainite, have remained controversial since the earliest discussions on this subject.

The original microstructural definition of bainite is Widmanstätten ferrite plates or laths with carbide precipitation at the austenite: ferrite boundaries [Rob29, Dav30]. Hehmann defined bainite as a non-lamellar aggregate of ferrite and carbide with acicular morphology dictated by the ferrite component [Heh72]. This

definition has been subsequently generalised as a non-lamellar, competitive eutectoid reaction in which the eutectoid phases can have any morphology other than the alternating plates characteristic of pearlite [Aar06, Lee88].

2.3.2 Bainite Morphology

Bainite morphology consists of aggregates of platelets or laths of ferrite, separated by regions of residual phases consisting of untransformed austenite or of phases such as martensite or cementite which form subsequent to the growth of bainitic-ferrite. According to its morphology, bainite can be classified to upper and lower bainite. Upper bainite is formed at higher temperatures where the diffusion rates are enough for carbon to diffuse to the lath boundaries. Lower bainite forms at lower temperatures where the carbon is trapped within the growing ferrite lath resulting in carbide precipitation within ferrite (**Fig. 2.2**) [Tak90]. However, if the initial carbon content is very low, e.g. ultra-low carbon bainitic (ULCB) steels, or carbide precipitation suppressing elements such as Si, Al and P are present, carbide formation can be inhibited or lags for a long period of time. The resulting morphology is referred to as carbide-free bainite [Bha01].

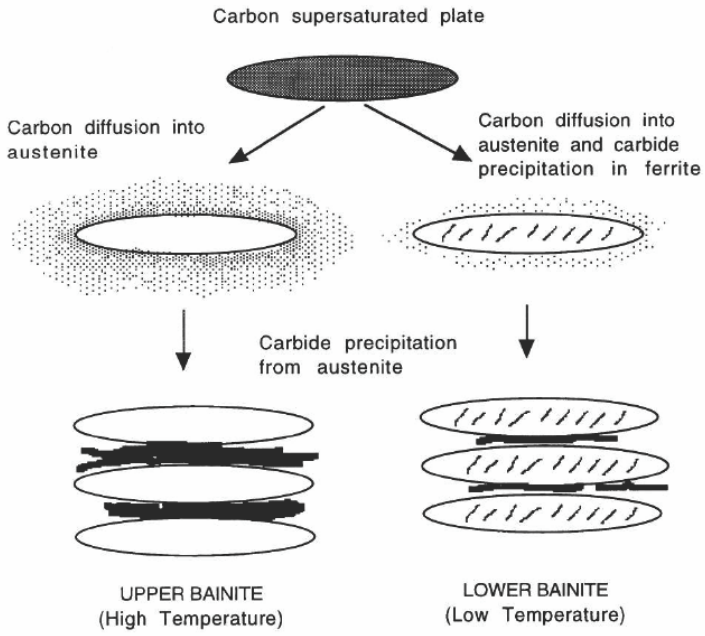

Fig. 2.2 Two different bainite morphologies formed from the supersaturated plates [Tak90].

The aggregates of the formed bainite-plates are called sheaves and the plates within each sheaf are called the subunits. The subunits are not isolated from each other but connected in three dimensions. It follows that they share a common crystallographic orientation (**Fig. 2.3-I**) [Bha01]. Furthermore, using scanning tunnel microscope (STM) (together with LOM, SEM and TEM), Wang et al. proved that those subunits are composed of sub-subunits as shown in **Fig. 2.3-II** [Wan95].

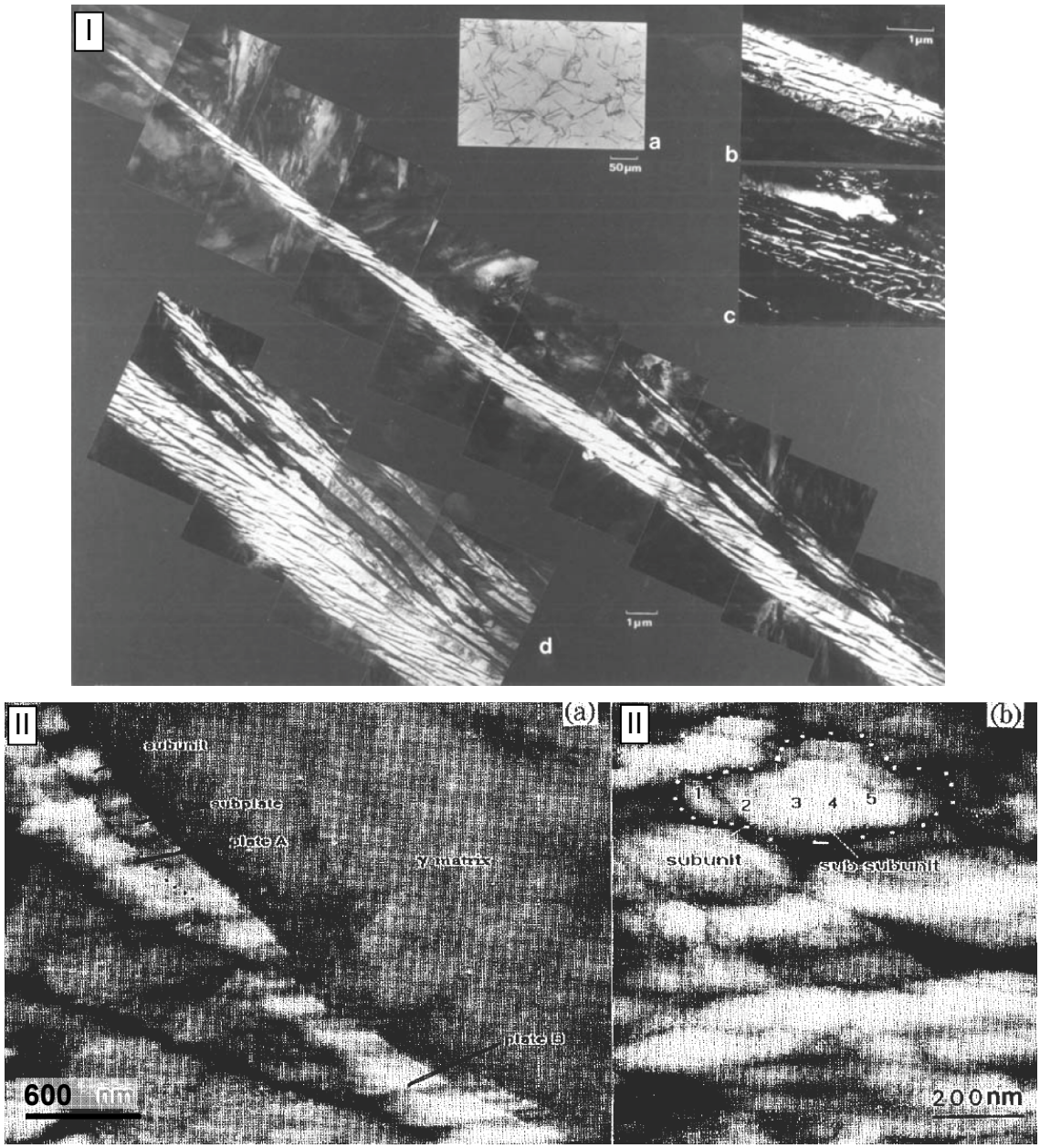

Fig. 2.3-I Transmition electron micrograph of a sheaf of upper bainite in a partially transformed Fe-0.43C-2Si-3Mn wt% alloy: (a) light micrograph; (b, c) bright field and corresponding dark-field image of retained austenite between the subunits; (d) montage showing the strucure of the sheaf [Bha01]. **Fig. 2.3-II** STM microstructure of bainite (a) lower and (b) higher magnification image indicating the existence of sub-subunits, shown by 1, 2, 3, 4, and 5 [Wan95].

2.3.3 Thickness of the Bainite Plates

The most important factors influencing the bainite plate-thickness are the austenite strength and the chemical free energy accompanying transformation (see **Fig. 2.4**) [Sin98, Bha01]. A quantitative analysis shows that temperature has only a small *independent* effect on the thickness of bainite plates. However, the perceived effect of temperature on the plate thickness could be indirect since both austenite strength and the nucleation rate are strongly dependent on temperature. The main conclusion is that strong austenite and high driving forces lead to a finer microstructure.

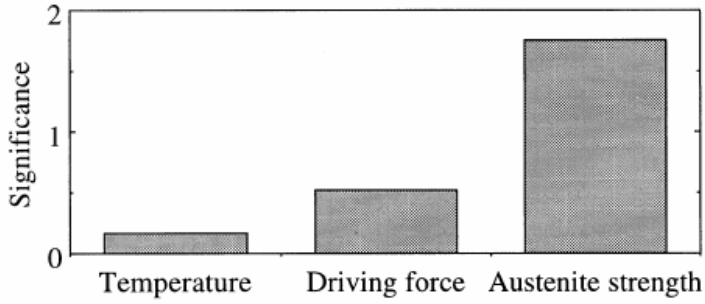

Fig. 2.4 The significance of the input variables in influencing the bainite plate-thickness [Bha01].

2.3.4 Kinetics of Bainite Transformation

The kinetics of bainite formation have a C-curve on the time-temperature-transformation (TTT) diagram because the reaction rate is slow both, at high and low temperatures. The diffusion of atoms becomes difficult at low temperatures where as the driving force for transformation is reduced as the temperature is raised [Bha01]. The bainite-reaction ceases entirely before all the austenite has decomposed. This has been known as the incomplete transformation phenomenon [Aar06, Bha01].

The incomplete transformation phenomenon is explained by Bhadeshia considering bainite transformation as a displacive transformation followed by subsequent partitioning of carbon into the residual austenite [Bha01, Bha90]. The displacive transformation is thermodynamically possible only below the T_0 temperature, where the austenite and ferrite of the same chemical composition have identical free energy. T_0 is modified to T_0' when considering the stored energy of bainite which comes from strain energy due to shape change accompanying transformation (**Fig. 2.5**). It is established by atom-probe

experiments that substitutional alloying elements do not redistribute during bainite transformation. Therefore, only carbon diffusion is involved in the growth of bainite. When the first plate of bainite forms without any diffusion, it will reject its excess carbon into the remaining austenite during the progress of the transformation as a whole. Because the austenite becomes enriched with carbon, a stage is eventually reached where it is thermodynamically impossible for further bainite to form by displacive transformation. At this point, the composition of bainite is given by the T_0 curve. If the alternative hypothesis is that para-equilibrium exists during all stages of transformation, then the reaction would stop when the carbon concentration of austenite is given by the A_{e3} curve. The transformation is experimentally found to stop when the average carbon concentration of the austenite is close to the T_0 curve rather than the A_{e3} boundary. Therefore, the transformation remains incomplete in the sense that there is no equilibrium between the austenite and ferrite and that the volume fraction of bainitic-ferrite does not satisfy the lever rule.

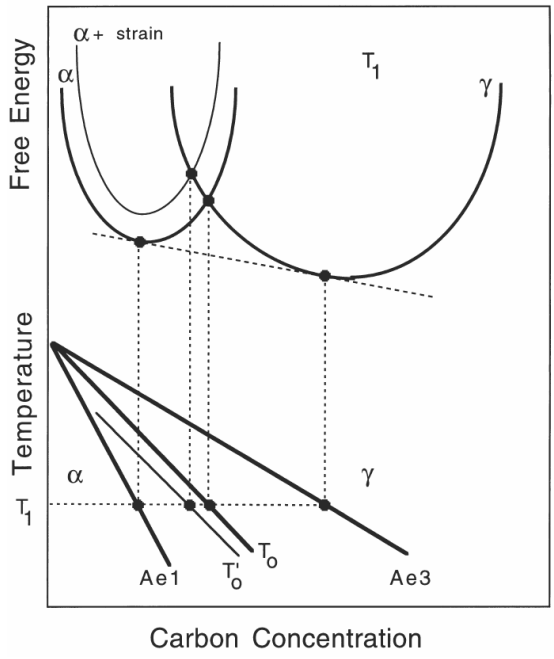

Fig. 2.5 Schematic illustration of the origin of the T_0 curve on the phase diagram. The T_0' curve incorporates a strain energy term for the ferrite, illustrated on the diagram by raising the free energy curve for ferrite by an appropriate quantity [Bha01].

2.4 Alloying Concepts in Steels

Numerous alloying concepts have been developed for steels in order to adjust the desired microstructure and properties. The alloying elements change the

thermodynamic stability of the phases and the kinetics of transformations whereby the transformation temperatures are shifted, the transformations are either promoted or hindered and the phase distribution is altered. Additionally, the elements might act as solid solution or precipitation hardeners and affect the grain size [Ble02]. **Fig. 2.6** depicts how the alloying elements affect the transformations during the different processing steps.

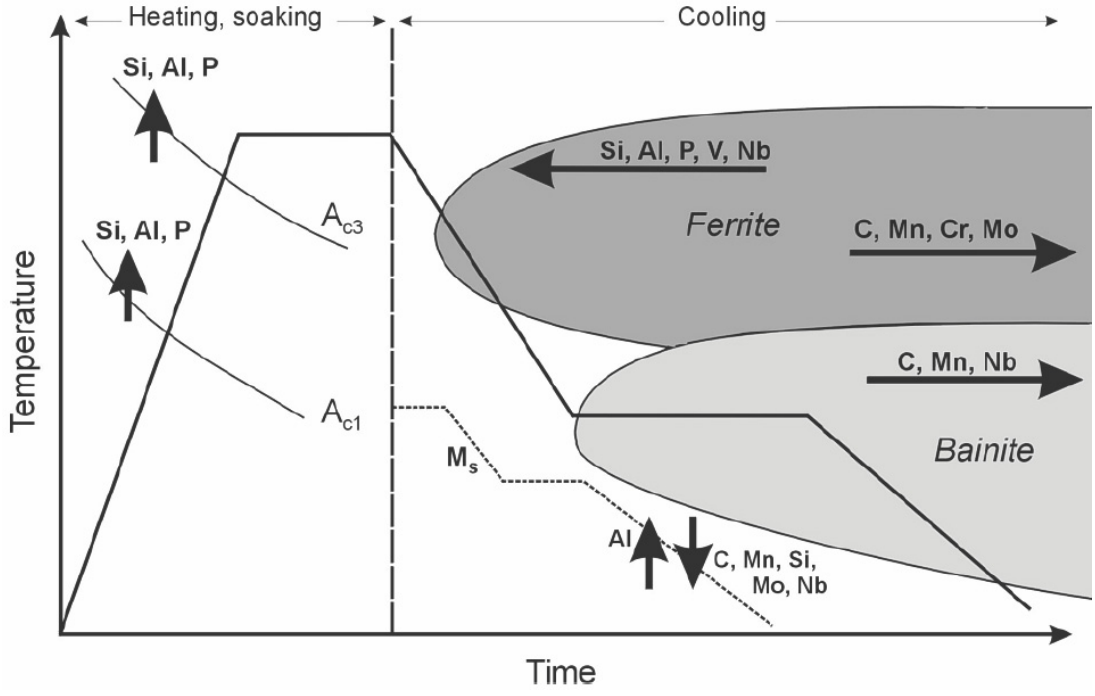

Fig. 2.6 Effect of alloying elements on the transformation behaviour during continuous annealing [Ble02].

Carbon: Carbon is the main alloying element by which all transformations are noticeably affected and by which the final microstructure and the mechanical properties are controlled. Carbon is the most hardenability enhancer and austenite stabiliser [Ble02].

Silicon: In this work, silicon is the key microstructural element in steel, which makes the retention of austenite feasible. Silicon, although a ferrite stabiliser, helps to retain carbon-enriched-austenite by suppressing cementite precipitation from austenite [Del65, Les78, Ray82]. Increasing the silicon-content results in increasing the retained austenite volume percentage (V_γ) as shown in **Fig. 2.7** [Che89]. Silicon also solid-solution strengthens ferrite and thus can enhance the overall strength of steel. On the other hand, Sugimoto and Usui [Sug92b] have

reported that increasing the silicon-content reduces the retained austenite carbon concentration, Cγ.

Manganese: Manganese increases carbon solubility in austenite, allowing for further enrichment, and slows the pearlitic reaction, which allows for a wider range of cooling rates. Furthermore, an increase in manganese may compensate for any reduction in silicon [Sak91, Shi02]. However, excessive levels of manganese can promote carbide precipitation in the austenite [Ble02]. Furthermore, Kim et al. have reported that the improvement of austenite hardenability because of excessive Mn content (2.52wt% in their studied case) results in martensite transformation during cooling after the isothermal bainite holding [Kim01]. Manganese, especially in conjunction with silicon, can affect the steel's surface chemistry and make hot-dip coating impossible [Mah02a, Mak03].

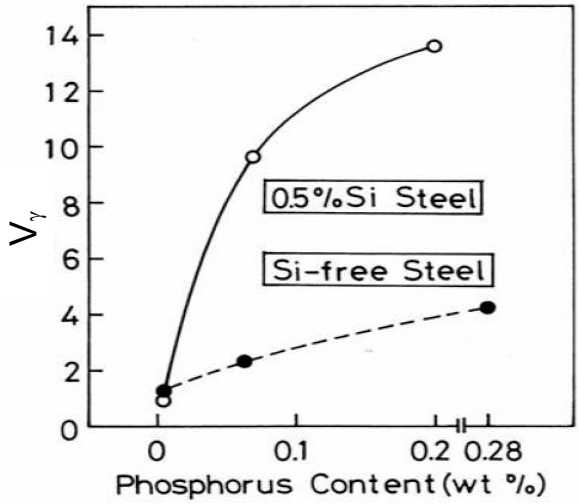

Fig. 2.7 Effects of silicon and phosphorus on retained austenite content [Che89].

Aluminium: In TRIP steels, aluminium has been cited as being a promising alternative for silicon as it inhibits cementite precipitation during bainite formation. The most important property is that aluminium does not exhibit the negative effects of silicon during galvanising process. As well, there are no adverse effects on the surface quality of the steel as there are with Si. However, aluminium has a smaller solid solution strengthening effect than silicon. Hence strength-ductility balance deteriorates when silicon is completely substituted by an equivalent amount of aluminium [Gir01, Jac01a]

Phosphorus: Like silicon, inhibits the formation of carbides. Low additions of mass contents less than 0.1 % proved to be sufficient to retard the precipitation of iron carbides and to provide a clear enhancement of strength. The beneficial effects of phosphorus on the formation and retention of retained austenite can only be accomplished together with silicon or aluminium [Ble02]. Although phosphorus causes cold work embrittlement in low and ultra-low carbon steels, this is not expected to be an issue in TRIP-type steels, as the carbon content is usually in excess of 0.1 wt% [Min01]. On the other hand, increasing the phosphorus increased the V_γ, especially in the presence of silicon (**Fig. 2.7**) [Che89].

Niobium: Current practice has placed much emphasis on the study and application of Nb addition to high strength low alloy (HSLA) steels, as it is deemed the most beneficial microalloying element, since it promotes austenite pancaking. It has also been classified as austenite stabiliser when added in amounts less than approximately 0.05 wt.% [Bau81]. Niobium is observed to increase the V_γ [Ohl02, Zar95]. The positive effect of niobium on V_γ is displayed in **Fig. 2.8**. The high austenite contents are a result of the combination of the different mechanisms including grain refinement, carbon enrichment, and martensite nucleation inhibition [Ohl02]. Niobium may also result in mechanical stabilisation of the small austenite particles [Zar95].

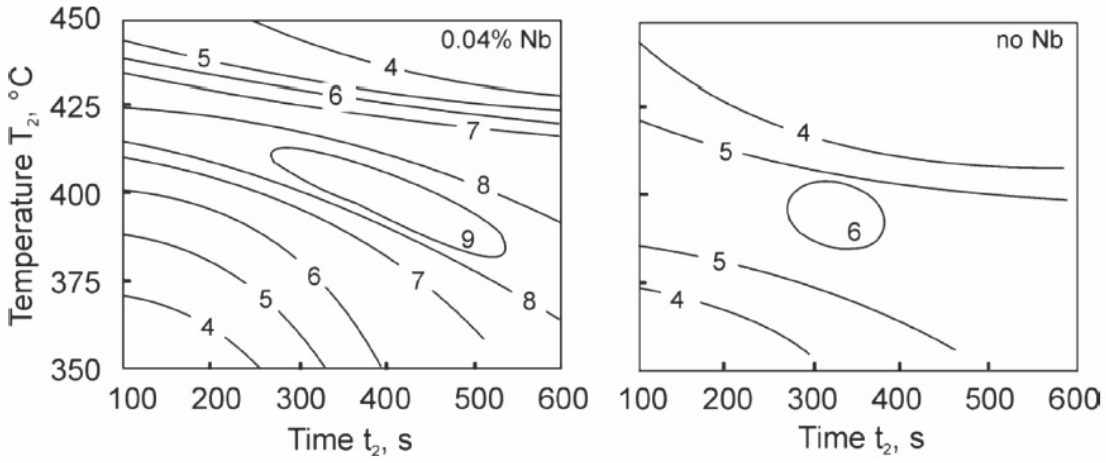

Fig. 2.8 Effect of niobium on the V_γ of TRIP steels for different process parameters during continuous annealing; composition in wt%: C: 0.17, Mn: 1.4, Si: 1.5 [Ohl02].

Molybdenum: Although molybdenum lowers the activity of carbon in austenite and promotes carbide formation from the thermodynamic point of view, Bleck

has reported that the contrary effect is observed in practice. Due to the strong solute drag effect, the carbide precipitation is even retarded in the presence of molybdenum. Moreover, molybdenum raises strength due to solid solution hardening [Ble02]

Furthermore, Mo has the retardation effect on the austenite transformation to both ferrite and pearlite rendering the process control more manageable. Capdevila el al. have observed that Mo has the strongest effect decreasing pearlite growth rate, when considering their studied alloying concentration values. A molybdenum concentration of 0.4 in weight pct. decreases in a hundred times the pearlite growth rate as compared with plain carbon steel for the same undercooling [Cap05].

The additions of molybdenum to niobium bearing steels are reported to bring about a further improvement of the combination of strength and ductility and to constitute another possibility of lowering the silicon level required [Ble02, Bou98].

Cobalt: Garcia-Mateo et al. have used cobalt to accelerate the bainite transformation in low temperature bainite steel because at the used temperature bainite transformation is very slow. This effect of cobalt is due to the fact that cobalt increases the free energy change for γ-α transformation [Gar03b].

2.5 Characterisation Methods for the Multi-phase Steel-Structure

2.5.1 Light Optical Metallography

The recent interest in the multiphase steels, characterised by complex microstructures, resulted in new developments in metallographic methods. So far, the limitation of using the classical etching techniques is not too detrimental, because most low-carbon steel grades possess a quite simple microstructure. Conventional etchants such as nital and picral used in the optical metallography cannot serve the purpose of phase identification well. Therefore, tint etching methods described below are developed for the sake of distinguishing different phases:

a. *Heat tinting:* Etching with 2% nital and then heating in air at about 260°C for 3-4 h without protective atmosphere before cooling to RT. With this technique the polygonal ferrite and bainitic-ferrite appear beige colour, retained austenite purple and martensite dark-blue. This method provides the opportunity to

observe the change in austenite/martensite volume fraction, distribution and size occurring during tensile testing [Tim02].

b. *LePera etchant:* This etchant is a mixture of two pristine solutions whose compositions are 1g $Na_2S_2O_5$ in 100 ml distilled water mixed with 4 g dry picric acid in 100 ml ethanol in a ratio of 1:1. The mixing process should be just before the etching process. LePera etchant tint the ferrite blue or brown the bainite dark-brown while both of the retained austenite and martensite are white [Lep80, Gir98].

c. *Klemm's I:* Pre-etching with nital then etching with 50 mL water saturated with $Na_2S_2O_5$ + 1g $K_2S_2O_5$. Klemm's I etchant stains ferrite light or dark blue, martensite brown or black and austenite white [Van84].

d. *10% $Na_2S_2O_5$:* Pre-etching with nital then etching with 10% $Na_2S_2O_5$ in aqua solution. This etchant reveals the martensite dark, ferrite off-white, austenite white and bainite brown [De03].

2.5.2 Scanning Electron Microscope (SEM)

Microstructural observation with SEM requires first the creation of a topographic contrast between the different phases by etching. Nital is generally well adapted, because it preferentially etches ferrite while leaving austenite and cementite intact. Ferrite-based phases such as bainitic-ferrite and pearlitic ferrite are dissolved and exhibit a typical morphology that generally allows their recognition (see **Fig. 2.9a**). The situation becomes more complex when a microstructure simultaneously presenting austenite and martensite as second phases is considered. By tempering samples at 200°C for 2 h, it becomes possible to differentiate the two phases by SEM [Gir98]. During this tempering regime, ε-carbides precipitate in martensite. Holding in this temperature range results in a dispersion of coarse particles within low-carbon martensite grains. Nital etching leads finally to the resolution of the martensite substructure, as shown in **Fig. 2.9b**.

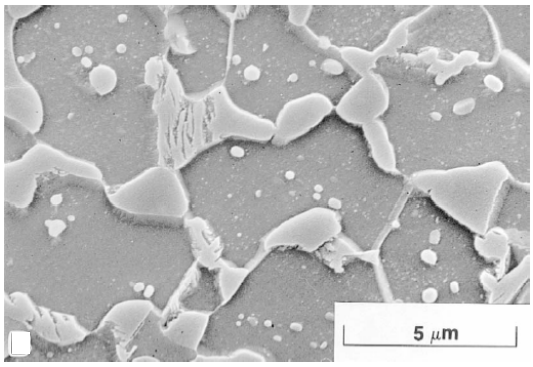

Fig. 2.9a SEM of nital-etched steel. Retained austenite and martensite exhibit both a smooth and a featureless aspect. [Gir98].

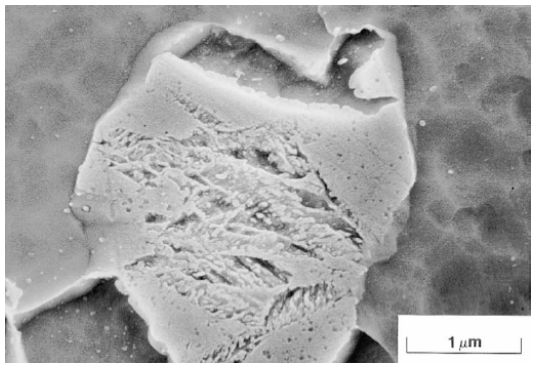

Fig. 2.9b Isolated martensite grain in tempered and nital-etched steel, featuring a typical, well-delineated substructure [Gir98].

2.5.3 Transmission Electron Microscope (TEM)

For the crystal structure and orientation determination TEM is most appropriate. It allows reaching a spatial resolution of about 10 nm [Zae04]. It provides the possibility of measuring the local carbon concentration which is an important measure for stabilisation of austenite [Zha98].

2.5.4 Magnetometry

Magnetic methods, such as polarisation measurements and thermo-magnetic analysis, are often used in metallurgical studies. The polarization measurements give a relation between measured polarisation (J) and applied magnetic field (H). From the polarization measurements, the saturation polarisation (J_s) can be obtained from the hysteresis curve.

Hysteresis is well known in ferromagnetic materials. When an external magnetic field is applied to a ferromagnet, the ferromagnet absorbs some of the external field. Even when the external field is removed, the magnet will retain some field: it has become magnetised.

The relation between the magnetic field (H) and the polarisation (J) is expressed in terms of the magnetic permeability:

$$J = \mu_0 (\mu_r - 1) H \qquad (2.1)$$

μ_0 is known as the magnetic constant or the permeability of vacuum with $\mu_0 = 4\pi \times 10^{-7}$ N·A^{-2}.

μ_r is the relative permeability of the material under study. μ_r of many materials is not constant, but depends on H. For example, in a ferromagnet the permeability is increasing with H, inverts at a certain point then decreases significantly. Further increase in H will not cause an increase in J as the permeability is too small. This is known as the saturation polarisation condition.

Several equations have been proposed to present the course of magnetisation curve at high field strengths in order to calculate saturation polarisation from hysteresis. At a field strength considerably higher than coercive force, saturation polarisation is sufficiently linear and can be calculated using a Taylor series of the dependency of saturation polarisation from magnetic field strength [Pol39, Pot90] under neglecting higher order powers.

$$J_s = J\left(1 - \frac{a}{H} - \frac{b}{H^2} - \cdots\right) \tag{2.2}$$

The saturation polarisation of a 100 % pure ferrite specimen is $J_s^{Fe} = 2.158T$ [Boz78]. If a specimen contains a fraction of austenite, x_A, with paramagnetic behaviour the saturation polarisation will be decreased by a factor (1- x_A):

$$J_A = (1 - x_A) \cdot J_s^{Fe} \tag{2.3}$$

Hence, x_A can be calculated by comparing the saturation polarisation of the specimen with retained austenite J_s^A with data from a 100% ferrite sample or a material with a known amount of ferrite, respectively:

$$x_A = \frac{J_s^{Fe} - J_s^A}{J_s^{Fe}} \tag{2.4}$$

However, the presence of alloying elements in the retained austenite steels reduces the saturation polarisation.

$$J_s^{alloy} = J_s^{Fe} - \sum_n x_n J_n^{element} \tag{2.5}$$

In eq. (2.5) x_n is the amount of alloying element and $J_n^{element}$ is the decrease of polarisation of 1% of a certain alloying element. Using eq. (2.4) and replacing the saturation polarisation of a pure ferrite by the saturation polarisation of an alloyed steel the amount of retained austenitic steel can be calculated with

$$x_A = \frac{\left(J_s^{Fe} - \sum_n (x_n J_n^{element})\right) - J_s^A}{J_s^{Fe} - \sum_n (x_n J_n^{element})} \quad (2.6)$$

2.5.5 X-Ray Diffraction Analysis (XRD)

X-ray diffraction is a common method for investigating the surface of crystalline materials. By determining the lattice spacings (d-spacing) in a sample; hence it is possible to extract crystallographic information. Qualitative and quantitative phase analysis, strain/stress analysis and quantification of preferred orientation (texture) can be performed. In short, a near monochromatic x-ray beam is illuminated on a sample. The x-rays are scattered in the sample and a detector is used to collect the scattered x-ray intensity. If the x-rays are in phase when they hit the detector they will constructively interfere (diffraction), while x-rays out of phase will destructively interfere. This is described by Bragg's law (**Fig. 2.10**) which states that if the wavelength of the incident x-rays is known and the angle were constructive interference appear is measured, the lattice spacing (d-spacing) can be determined [Sur98], The d-spacing is determined with Bragg's law:

$$n\lambda = 2d\sin\theta \quad (2.7)$$

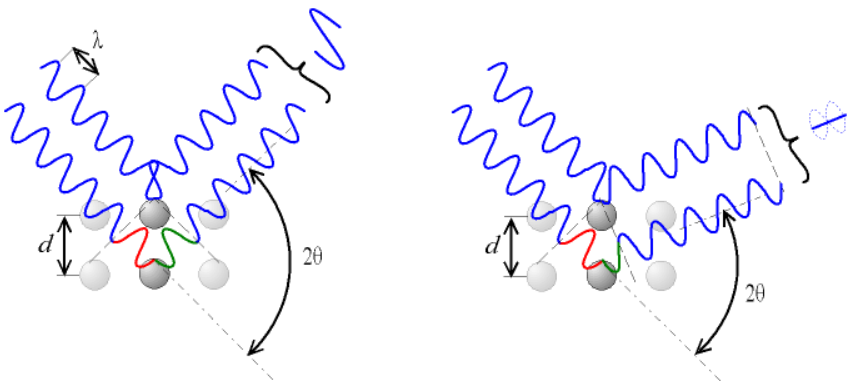

Fig. 2.10 Bragg's law: according to the 2θ deviation, the phase shift causes constructive (left picture) or destructive (right picture) interferences. The d-spacing is determined with Bragg's law: $n\lambda = 2d\sin\theta$

Precise measurement of lattice parameter: In a cubic system (e.g. bcc or fcc), the d spacing corresponding to each diffraction line can be related to the lattice parameter "a" by:

$$a^2 = d^2/(h^2 + k^2 + l^2) \quad (2.8)$$

where hkl are the Miller indices. Miller indices are a symbolic vector representation for the orientation of an atomic plane in a crystal lattice and are defined as the reciprocals of the fractional intercepts which the plane makes with the crystallographic axes. **Fig. 2.11** describes the series of steps that leads to the notation of an atomic plane using Miller indices. Recalling that there are three axes in crystallographic systems (except sometimes in the hexagonal system adopts a convention where there are four axes). Since the unit cell repeats itself in space, the notation actually represents a family of planes, all with the same orientation.

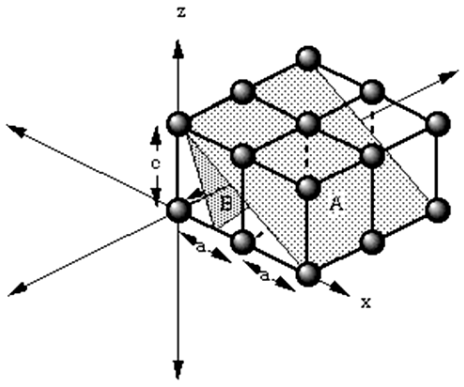

	plane A			plane B		
	a	b	c	a	b	c
intercept length	1	∞	$\frac{1}{2}$	$\frac{1}{2}$	∞	1
reciprocal	$\frac{1}{1}$	$\frac{1}{\infty}$	$\frac{1}{1/2}$	$\frac{1}{1/2}$	$\frac{1}{\infty}$	$\frac{1}{1}$
cleared fraction	1	0	2	2	0	1
Miller indice	(102)			(201)		

Fig. 2.11 The series of steps that leads to the notation of an atomic plane using Miller indices.

Measuring the Bragg angle θ for hkl and using the Braggs law to determine "d" allows the calculation of "a". But it is $\sin\theta$, not θ, which appears in the Braggs law. Precision in d, or a, therefore depends on the precision in $\sin\theta$. For this reason the key to precision in parameter measurements lies in the use of back reflected beam having 2θ values as near to 180° as possible. The true values of "a" should be found simply by plotting measured value against a certain function of θ, the extrapolating to θ = 90° results in a very accurate value of "a". The measured values of "a" are plotted against a function of θ, rather than θ, or 2θ directly, this function should account for the source of errors. Usually, the largest single source of error is the displacement of the sample from the diffractometer

axis. This error can be accounted for by extrapolation against $\cos^2\theta/\sin\theta$ [Cul01, Str95]. Extrapolation against "$\cos^2\theta/\sin\theta + \cos^2\theta/\theta$" is known as Nelson-Riley method and use to account for the vertical divergence of the incident beam [Cul01, Ang04].

Quantitative estimation of the retained austenite: The volume percentage of retained austenite (Vγ) could be estimated from measurements of the integrated intensities of ferrite and austenite phases assuming they are the only phases presented. Thus, if a relative volume percentage of ferrite to austenite, Vα /Vγ, is determined it can then be converted to absolute volume percentage with the identity:

$$V_\alpha + V_\gamma = 100 \tag{2.9}$$

Ratios of volume percentages V_α/V_γ are calculated from the integrated intensities I_α and I_γ, which can be determined from the x-ray diffraction pattern and constants R_α and R_γ:

$$\frac{V_\gamma}{V_\alpha} = \frac{I_\gamma}{R_\gamma} \times \frac{R_\alpha}{I_\alpha} \tag{2.10}$$

The R-values are constants determined by the particular phase, the particular Bragg reflection and the wavelength of the incident x-rays. The calculations of the R-values and the I-values at different peaks are most readily done on a computer using a spreadsheet program. This will be illustrated in section (3.5.1)

2.6 Interpreting the Dilatometric Data for Transformations in Steels

Dilatometry registers the length changes that occur during the heat treatment of a sample. The real-time monitoring of the sample dimensional changes allows the study of transformations processes. When a material undergoes a phase change, lattice structure changes and this is in principle accompanied by change in specific volume. In the case of a pure iron specimen, transformation from austenite, which has a fcc structure, into ferrite, which has a less closely packed bcc structure causes a volume expansion of about 1.6% [Gom03].

The $A_{e1}$and A_{e3} are easily detected by dilatometry during heating or cooling cycles, but some hysteresis is observed. Consequently, three values for each point can be obtained: A_c for heating, A_r for cooling, and A_e for equilibrium

conditions. It should be emphasised that the A_c- and the A_r-values are sensitive to the rates of heating and cooling, as well as to the presence of alloying elements [Gar02].

2.6.1 The Transformation Points

In order to locate the transformation points the linear part of the thermal contraction or expansion curve is extrapolated before and after transformation. The $\gamma \leftrightarrow \alpha$ phase transformation is defined as the temperature at which the thermal contraction/expansion during cooling/heating processes, respectively first deviates from linearity. However, the determination of transformation temperatures can be subject to errors, particularly since the thermal contraction before and after transformation is often not linear, and the dilatometer trace may exhibit some degree of curvature [Pri94].

In the heating dilatometric curve, normally there is no detectable differentiation between the pearlite dissolution process and $\alpha \rightarrow \gamma$ transformation. However, the experimental curve in **Fig. 2.12a** shows an unusual well-formed contraction associated with the pearlite dissolution [Gar02]. The possibility of discriminating the pearlite dissolution process and the ferrite-to-austenite transformation by means of high-resolution dilatometry permits the determination of the T_c temperature or starting temperature for ferrite-to-austenite transformation. An accurate dilatometric determination of transformation temperatures corresponding to the pearlite dissolution process in the steels could only be performed when fine-enough pearlite is obtained. The small contraction at temperature T_D (**Fig. 2.12a**), after the relative change in length reaches a minimum, corresponds to the formation of austenite from some grains of ferrite that remains untransformed in the microstructure. As Datta and Gokhale [Dat81] found under isothermal conditions, those residual ferrite grains transform almost instantaneously at the T_D temperature due to a change in ferrite-to-austenite transformation kinetics.

Fig. 2.12b shows the contraction that takes place during the ferrite-to-austenite transformation by continuous heating in martensitic stainless steel with an initial microstructure of ferrite plus globular carbides ($M_{23}C_6$). These dilatometric curves, apart from $\alpha \rightarrow \gamma$ transformation between A_{c1} and A_{c3} temperatures, reproduce a nonlinear length variation associated with the carbide dissolution

process. During heating at temperatures above A_{c3}, there is a continuous increase of slope in the curve $\Delta L/L_0 = f(T)$ that corresponds to the progressive dissolution of the carbides in austenite. The point of inflection of this section corresponds to the Ac_c temperature or temperature at which the carbide dissolution process ends.

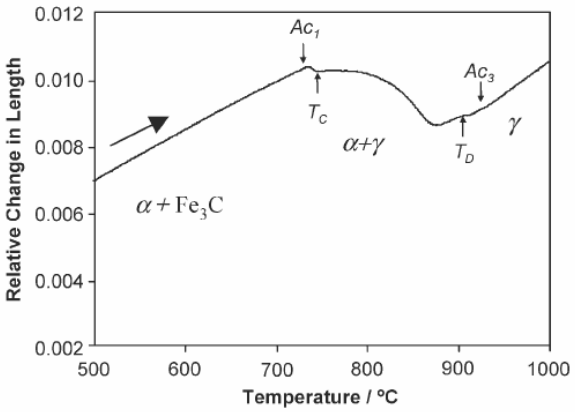

Fig. 2.12a Heating dilatation curve of a low carbon steel (Fe-0.11C-0.50Mn) obtained at a heating rate of 0.05K s^{-1} [Gar02].

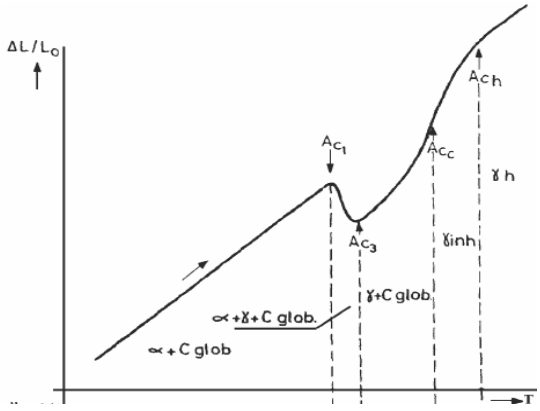

Fig. 2.12b Diagram of the heating dilatometric response of α-γ transformation and the carbide dissolution process of martensitic stainless steels [Gar02].

On the other hand, **Fig. 2.13** shows splitting phenomena detected in the martensitic transformation of X30–45Cr13 and X40–60CrMoV14 stainless steels by high-resolution dilatometric analysis [Gar02]. In these steels, the M_{sII} represents the temperature at which the splitting above M_{SI} commences. The weak intensity of this anomaly indicates that it is produced by the transformation of small amounts of austenite and does indeed correspond to the volume increase produced during the martensitic transformation of areas of austenite poor in carbon and carbide- forming elements.

This type of splitting is generally explained in terms of carbide precipitation during cooling. The M_{So} represents the temperature at which the splitting below M_{sI} commences. The small expansion anomaly identifying this stage (**Fig. 2.13**) indicates that it is also associated with a partial transformation, namely, the martensitic transformation of areas of austenite more concentrated than the massive austenite.

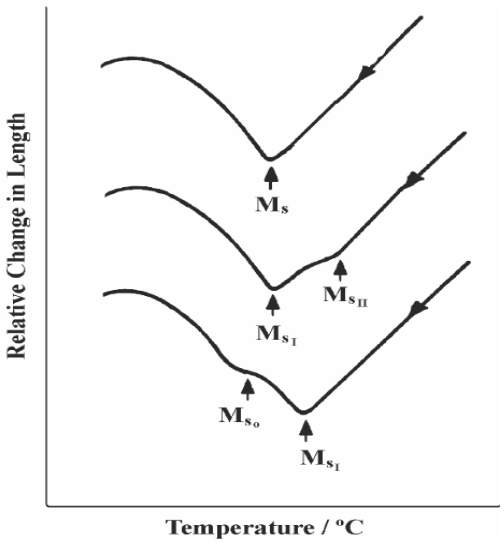

Fig. 2.13 Dilatometric representation of the splitting phenomena in the martensitic transformation [Gar02].

2.6.2 Quantitative Interpretations: Isothermal Bainite Transformation

A lot of attempts to provide methods for quantitatively relating length change to the extent of transformation have been proposed. For the transformation of austenite (γ) into a mixture of bainitic-ferrite and carbon-enriched austenite during isothermal holding, Takahashi and Bhadeshia [Tak89] have shown that the relative length change $\Delta L/L_0$, can be related to the volume fraction of bainitic-ferrite (V_b) by:

$$\frac{\Delta L}{L_0} = \frac{2V_b a_\alpha^3 + (1-V_b)a_\gamma^3 - a_{\gamma 0}^3}{3a_{\gamma 0}^3}, \qquad (2.11)$$

where a_α is the lattice parameter of ferrite at the reaction temperature, a_γ is the lattice parameter of austenite at the reaction temperature at any stage of the reaction and $a_{\gamma 0}$ is the lattice parameter of austenite at the reaction temperature before the reaction.

$$a_\alpha = a_{\alpha r}[1+I_\alpha(T-25)]$$

$$a_{\gamma 0} = a_{\gamma r}(\bar{x})[1+I_\gamma(T-25)]$$

$$a_\gamma = a_{\gamma r}(x)[1+I_\gamma(T-25)]$$

where T is the reaction temperature (°C), I_α and I_α are the linear thermal expansion coefficients of ferrite and austenite, respectively (K^{-1}), $a_{\alpha r}$ is the lattice

parameter of ferrite at the ambient temperature, $a_{\gamma r}(\bar{x})$ is the austenite lattice parameter at the ambient temperature as a function of the average carbon content of the steel. $a_{\gamma r}(x)$ is the austenite lattice parameter at the ambient temperature as a function of the carbon content of residual austenite at any stage of the reaction. $a_{\gamma r}(\bar{x})$ and $a_{\gamma r}(x)$ can be calculated using ref. [Pea67]. x which is the carbon content of residual austenite at any stage of the reaction can be calculated from the equation:

$$x = \frac{\bar{x} - V_b s}{1 - V_b}, \tag{2.12}$$

where s is the total carbon of the ferrite. **Fig. 2.14** represents the relationships among volume fractions transformed and corresponding relative length changes during isothermal transformation at 420°C to ferrite with 0.03wt % carbon, to super-saturated ferrite with 0.2 wt% carbon and also during isothermal transformation at 370°C to ferrite with 0.03wt % carbon for steel Fe-0.3 wt%C-4.08 wt% Cr.

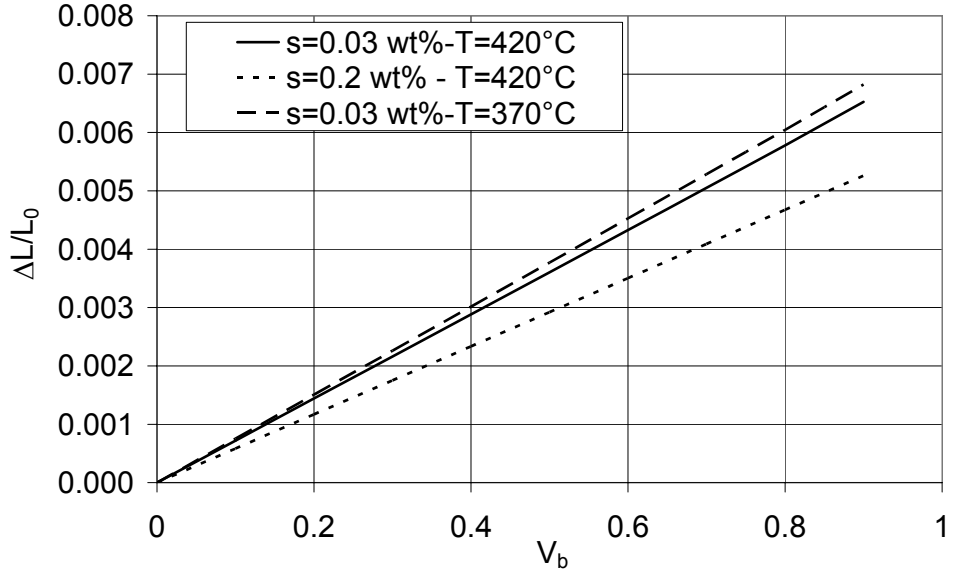

Fig. 2.14 Length change as a function of volume fraction of ferrite, during isothermal transformation of austenite at the prescribed temperature T assuming the ferrite carbon content “s” - for steel Fe-0.3 wt%C-4.08 wt% Cr [Tak89].

2.6.3 Quantitative Interpretations: Non-Isothermal Kinetics

For the non-isothermal transformation kinetics, a common method to determine the remaining austenite-fraction as a function of temperature is to extrapolate

the linear expansion behaviour from the temperature regions where no transformations occur, and to subsequently assume a proportionality between the fractions decomposed austenite and the observed length change. This method is referred to as the lever-rule method. The lever rule is applied as a quick method for estimating the transformed phase amount during cooling and heating [Pan95, Mah02b, Pal07]. However, in the case of carbon steel the lever rule does not give an accurate transformed phase amount because it does not take into account that the carbon redistribution between the forming ferrite and the remaining austenite, increases the specific volume of austenite and also that the formation of pearlite has a distinctly different volume effect to the formation of ferrite [Gom03]. Furthermore, for a multi-step phase transformation, Zhao et al. [Zah01a] reported that the lever rule is not applicable to the interpretation of the dilatation curve due to the large resulted committed-error. Many researches have been done using several calculation methods in order to avoid the errors that arise if the aforementioned aspects are not taken into account [Zha01a, Zha02b, Kop01, Gar98]. **Fig. 2.15** represents an example comparing the fraction curves obtained from the lever rule and two suggested methods.

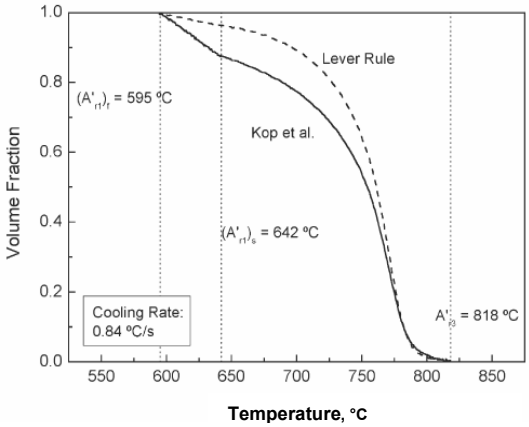

Fig. 2.15a Fraction curves obtained from lever-rule and Kop et al. method at given cooling rate [Gom03].

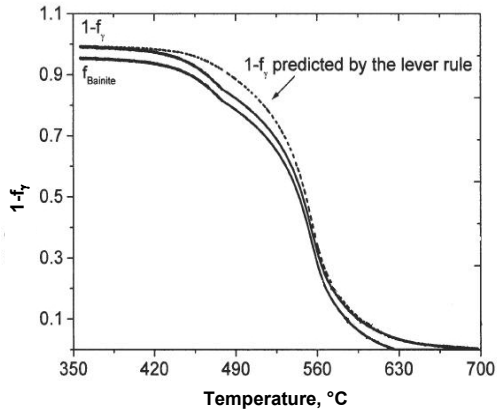

Fig. 2.15b Fraction curves obtained from lever-rule and Zhao et al. method at given cooling rate [Zha01a].

In general, the lever rule always gives a higher ferrite percentage than that which is really obtained, irrespective of the steel's carbon content, since it cannot distinguish between the dilatation experienced by the specimen due to the formation of ferrite and the dilatation experienced by the austenite due to progressive carbon enrichment.

Chapter 3
Experimental Methods and Details

3.1 Production of the Materials

All alloys were melted in a high frequency furnace in the laboratory. The chemical analysis of the investigated alloys is given in **Tab. 3.1**. The selection of the compositions was based upon current researches and understanding in the field as will be described in the next chapters.

Tab. 3.1 Chemical composition of the steel used (wt%)

Steel	C	Si	Mn	Al	Mo	Co	Cr	Nb	P	S	N
A1	0.278	0.852	1.48	0.228	0.401	-	-	0.041	0.037	0.020	0.006
A2	0.254	0.869	1.37	0.643	0.383	-	-	0.040	0.030	0.021	0.008
B1	0.420	1.50	2.37	0.820	0.250	1.40	1.41	-	0.044	0.013	0.005
B2	0.565	1.52	2.02	0.654	0.239	1.59	1.21	-	0.042	0.014	0.007

3.2 Heat Treatment

The heat treatment cycles were conducted primarily in two salt baths, one for the annealing followed by one for austempering. The heat treatment parameters have been selected according to the thermodynamic calculations and dilatometric measurements as will be described later. The annealing is performed in Durferrit GS 540/R2® and austempering in Durferrit AS 140® salt baths. The inertor R2 had been added to prevent any oxidation or decarburisation during the austenitisation process.

3.3 Dilatometry

Dilatometric experiments were conducted on a Baehr dilatometer “DIL 805A”, which has a resolution of 0.05□m/0.05K. The dilatometer uses the induction heating principle and can work under vacuum, air and inert gas. The test specimens had been degreased using an acetone solvent. Sheathed type S “Pt/Pt-10% Rh” thermocouple wires with a nominal diameter of 0.1 mm had been individually spot welded to the specimen’s surface in central position using a welding jig. Each specimen was held between two quartz rods, with one of the rods fixed, and the other connected to a linear variable differential transducer (LVDT) as shown in Fig. 3.1. A reference rod is also connected to the LVDT. The dimension variations of the specimens during the thermal cycle are

transmitted via the moving quartz pushrod to the LVDT sensor. After placing the sample between the pushrods, the insulating sheaths on the thermocouple wires had been moved along the thermocouple wires until they contacted the specimens's surface. This step is essential to prevent undesirable heat loss and to avoid contact between the two thermocouple wires [Ast04]. The thermal cycles had been performed under vacuum of 5×10^{-5} mbar. Helium gas was used for cooling. The dilatometric curves had been recorded along the thermal cycle with the help of a computer-data acquisition system.

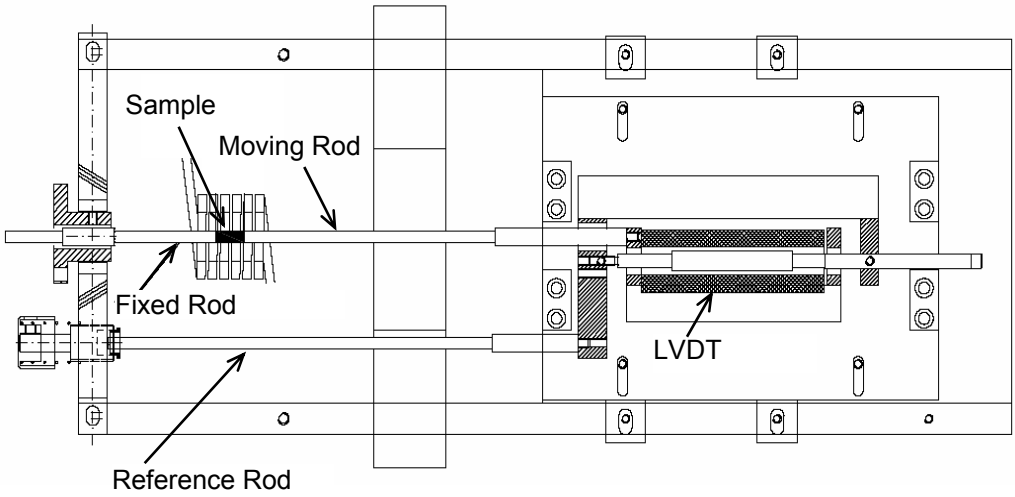

Fig. 3.1 Schematic view of the measurement system in "DIL805A" dilatometer.

Although the induction heating has not direct effect on heating the push rods, their temperature do not remain constant during the measurement due to thermal conductivity effects from the sample. Due to the small expansion coefficient of quartz, $0.5\times10^{-6}K^{-1}$ (the expansion coefficient of steel is approximately $14\times10^{-6}K^{-1}$), the contribution of the push rods to the measured length is negligible.

3.3.1 Independent Check of the Temperature Measurements

The Curie temperature (T_{CU}) can be measured during heating by monitoring of the HF-power. This provides a means to have an independent absolute temperature reference, since a ferromagnetic material with $T < T_{CU}$ is more easily heated by induction than a paramagnetic material. Therefore, a distinct increase in the power required to keep the sample at the scheduled temperature appears when the sample transforms from the ferromagnetic to the

paramagnetic state. The Curie temperature of steel is known to be almost independent of the carbon concentration, but it depends strongly on the manganese concentration. This dependence can be expressed by the relation

$$T_{CU} = [769°C - x_{Mn} \times 1500]°C, \quad (3.1)$$

where x_{Mn} is the manganese weight fraction [Kop01]. **Fig. 3.2** gives three examples of such internal temperature checks. The steel A2 contains 1.37 wt% Mn (**Tab. 3.1**), which implies that C_T = 748.5°C. Steel B1 and B2 with more manganese contents of 2.37 and 2.02 wt.%, have lower Curie temperature, namely 733.5°C and 739°C, respectively. The temperatures at which the heating power jumps during the measurements indicate that the dilatometer temperature measurement system yields correct absolute temperature values.

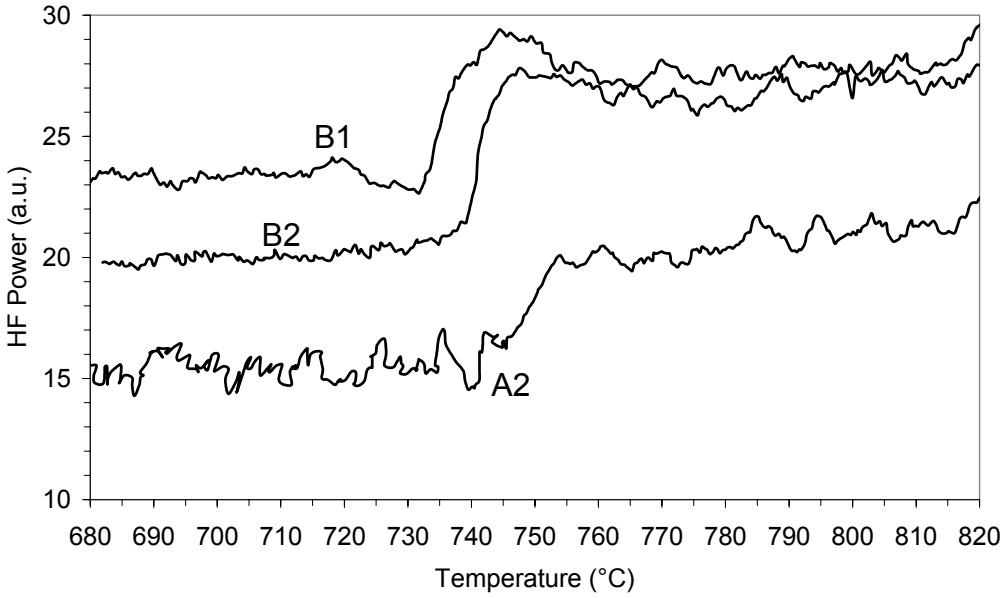

Fig. 3.2 The change in the required high frequency (HF) power required to follow the temperature for the samples A2, B1 and B2.

3.4 Metallographic Investigations

The Micrographs were taken perpendicular to the transverse-deformation direction. The specimens were prepared by mechanical grinding followed by polishing up to a 0.25 μm-grade alumina solution. In order to reveal phases and grain boundaries, two etchant methods were used, namely, 2% nital and LePera's etchant. The LePera's etchant composed of two parts:

1- 1 grams of sodium metabisulfite + 100 mL distilled water.

2- 4 grams of picric acid + 100 mL ethyl alcohol.

The two components are kept separate until use when they were mixed together in equal parts by volume [Lep80, Gir998]. Etching time was between 20 and 30s. After etching, the samples were rinsed with ethyl alcohol and dried under a warm air drier. LePera's etchant stains ferrite brown and/or blue, bainite dark-brown to grey, while martensite and austenite remains white. Quantitative analysis of the photomicrographs was performed using image analysis software "Analysis Five"®.

SEM investigations of selected specimens were also conducted on a CamScan Series 4 device. For these investigations the samples were mechanically prepared as described above before being deep etched in nital.

3.5 XRD Investigations

The x-ray diffraction (XRD) was used to measure the volume percentage of retained austenite, V_γ, and its carbon content, C_γ. Prior to x-ray examination the samples had been mechanically ground, polished and then lightly etched with nital to remove the distorted thin layer resulting from the metallographic preparation procedure. Siemens D5000 Diffractometer, which has goniometric diameter of 600 mm, was used for the investigations. Data collection is performed under computer control using the Diffrac Plus software application.

The experiments were conducted using Fe-filtered Co-Kα radiation at 40 kV and 40 mA. The peak intensities of the whole patterns were collected by the step scanning technique utilising small step size of $\Delta 2\theta$ = 0.025° and a period of 3s at each fixed value of 2θ in the range between 48°-130°.

3.5.1 Austenite Volume Fraction

The V_γ was measured using the integrated intensity from (111), (200), (220) and (311) austenite diffraction peaks and from (110), (200), (211) and (220) ferrite diffraction peaks. Eq. 2.10 was used to determine the ratio V_γ/V_α. For four reflections per phase, the I_α/R_α and the I_γ/R_γ were determined from equations:

$$\frac{I_\gamma}{R_\gamma} = \frac{1}{4}\sum_{i=1}^{4}\frac{I_i^\gamma}{R_i^\gamma} \tag{3.2a}$$

$$\frac{I_\alpha}{R_\alpha} = \frac{1}{4}\sum_{i=1}^{4}\frac{I_i^\alpha}{R_i^\alpha} \tag{3.2b}$$

Once the ratio "V_γ / V_α" is found, the value of V_γ can be obtained from eq. (2.9).

The sequences required to calculate the positions, 2θ, and relative intensities, R_α and R_γ, values are illustrated in **Tab. 3.2**, with:

Column 1: Miller indices of the diffraction planes in the fcc and bcc phases (c.f. **2.11**).

Column 2: Needed for further calculations.

Column 3: Values of $\sin^2\theta$ are given by the equation:

$$\sin^2\theta = \frac{\lambda^2}{4a^2}(h^2+k^2+l^2) \qquad (3.3)$$

which is actually a substitution of eq. (2.8) in eq. (2.7). For the current study, the used CoKα radiation has a wave length λ = 0.17890 nm. The austenite lattice parameter is a_γ = 0.35730 nm and the ferrite lattice parameter a_α = 0.28665 nm.

Column 4: Expected positions of the peaks in the diffraction pattern.

Column 5: Needed for further calculations.

Column 6: The Lorentz-polarisation factor $L_p = \frac{1+\cos^2 2\theta}{\sin^2\theta\cos\theta}$

Column 7: The atomic scattering factor of iron, f_{fe}, is obtained from appendix 10 of Ref. [Cul01] using the input value of $\frac{\sin\theta}{\lambda}$.

Column 8: According to Ref. [Cul01] p. 139, the structure factor, F, can be obtained as follows:

For the fcc, γ phase, as at all reflection planes all the three sums (h+k), (h+l) and (k+l) are even integers, then $F = 4f_{fe}$.

For the bcc, α phase, and as all the (h+k+l) are even integers then $F = 2f_{fe}$.

Column 9: The multiplicity factor, ρ, obtained for the cubic system from appendix 11 of Ref. [Cul01].

Column 10: The temperature factor of iron at 20°C is obtained from the **Fig. 3.3** using $\frac{\sin\theta}{\lambda}$ input value [Cul01].

Column 11: The R is obtained from the eq. [Cul01-p. 352]:

$$R = (\frac{1}{v^2})\left[F^2 \rho L_p\right](e^{-2M}) \qquad (3.4)$$

i.e. the yield of multiplying columns 6, 8,9 and 10 divided by the squared volume of the unit cell, v^2.

Tab. 3.2 Calculation of the positions, 2θ, and relative intensities, R, of the fcc and bcc phases in steel using CoKα. radiation.

1	2	3	4	5	6	7	8	9	10	11
hkl	$h^2+k^2+l^2$	$\sin^2\theta$	$2\theta°$	$(\sin\theta)/\lambda$ (nm^{-1})	L_p	f_{fe}	F^2	ρ	e^{-2M}	$R\times10^7$
111γ	3	0.1880	51.421	2.4221	8.2000	17.463	4879.3	8	0.96	14.768
200γ	4	0.2507	60.093	2.7968	5.7536	16.278	4239.4	6	0.95	6.6822
220γ	8	0.5014	90.160	3.9553	2.8245	13.299	2829.6	12	0.89	4.1025
311γ	11	0.6894	112.263	4.638	2.9763	12.051	2323.7	24	0.87	6.9406
110α	2	0.1948	52.402	2.4651	7.8546	17.315	1199.3	12	0.96	19.357
200α	4	0.3895	77.233	3.4861	3.4463	14.358	824.66	6	0.93	2.8586
211α	6	0.5843	99.702	4.2696	2.7299	12.686	643.73	24	0.88	6.6900
220α	8	0.7790	123.920	4.9301	3.5810	11.601	538.3	12	0.85	3.5025

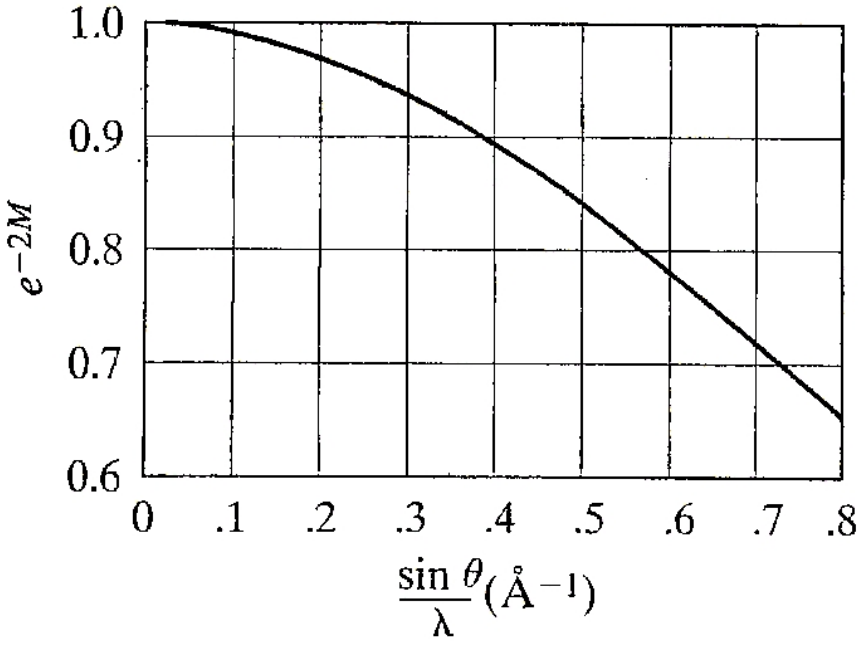

Fig. 3.3 Temperature factor e^{-2M} of iron at 20°C as a function of $(\sin\theta)/\lambda$ [Cul01-p.155] .

3.5.2 Austenite Carbon Content

The retained austenite carbon content, C_γ, was calculated via lattice parameter measurements and eq. [Str05, Cul01]:

$$C_\gamma=(a_\gamma-0.3555)/0.0044 \quad (3.5)$$

Where a_γ is given in nm and C_γ in mass%.

The observed 2θ values of the austenite peaks were used to calculate the d spacing using eq. (2.7) (Bragg's law) and then the a_γ using eq. (2.8). The values were plotted against $\cos^2\theta/\sin\theta$. The precise lattice parameter, a_γ, is determined by extrapolation to $\cos^2\theta/\sin\theta = 1$ [Str05, Cul01].

3.6 Magnetic Measurement

During the present study magnetometry was the preferred method for obtaining the retained austenite volume fractions. The advantages of this technique are that the measurement is performed on the whole volume, the specimens do not need a special preparation and the measurements are fast, reliable and more sensitive to the retained austenite than the x-ray diffraction method [Wir02, Zha01b]. However, in some cases due to the limits imposed by the small size of

the samples (e.g. dilatometric samples), it was not possible to use this technique for measuring the amount of retained austenite. Still the XRD technique is utilisable.

Fig. 3.4 shows a schematic view of the magnetic measurement system. A detailed description of the hysteresis recorder is described elsewhere [Pot90, Ram01]. A specimen is exposed to an alternating magnetic field of magnetising frequency f_{mag}=1 Hz which is generated by a GPIB controlled wave form generator (Philips PM 5191), amplified by a power amplifier (DCP 260/60-C, Servowatt Renz Elektronik, Gerlingen, Germany) and fed to the field coils. The generated magnetic flux density $B=\mu_0\mu_r \cdot H$ (μ_0: permeability of vacuum; μ_r: permeability of test specimen; H: magnetic field) includes not only magnetic properties of the sample but also magnetic properties of vacuum respective air. To eliminate this part of the induction an identical coil system is connected in series (compensation coils). The induction coils are connected anti-parallel to get a resulting signal which only delivers the change of the magnetisation in the sample and therefore, directly the polarisation J of sample is measured. The signal at the field coils and the induced signal of the induction coils are tapped and stored by a two channel analogue digital converter sampler (ADC, Dirkes GmbH, Telgte, Germany). The measured and time fitted signals are sent via RS232 to a computer and evaluated. A maximum magnetic field of approximately H_{max} = *45 kA/m* was applied to the sample, the saturation polarisation, J_S, was determined using eq. (2.2).

The amount of retained austenite can be calculated by comparing the saturation polarisation of the specimen with retained austenite (J_s^A) with that of an austenite-free specimen containing the same amount of alloying elements (J_s^{alloy}), using eq. (2.6).

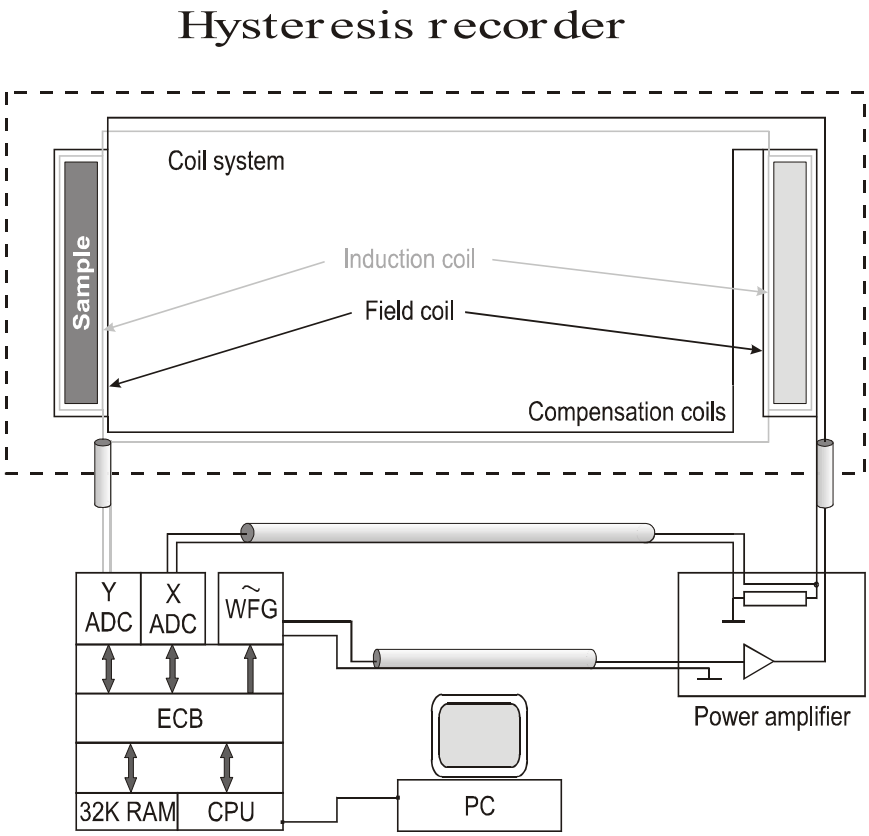

Fig. 3.4 Schematic view of the hysteresis recorder.

The austenite-free specimens of the alloys A1 and A2 have been prepared by heating the specimens to a temperature of 950°C holding there for 20 min and then very slow cooling, by switching off the furnace, to RT. The cooling rate did not exceed 1.5 K/min. The measured J_s^{alloy} for alloy A1 and A2 were 1.973 T and 1.948 T, respectively. On the other hand, the J_s^{alloy} values can be theoretically calculated using a linear function of the weight percent alloying additions, rather than measuring saturation on a reference sample (see eq. (2.5)). For that, the $J_n^{element}$ are described elsewhere [Tra02, Boz78]. The measured and calculated values for alloys A1 and A2 are listed in **Tab. 3.3**. **Fig. 3.5** shows a representative example comparing the hysteresis curve of austenite free sample with the one having 18.4% retained austenite.

Tab. 3.3 Measured and calculated J_s^{alloy} (T)

	J_s^{alloy} (measured)	J_s^{alloy} (theoretical) [Tra02]	J_s^{alloy} (theoretical) [Boz78]
A1	1.973	1.997	1.895
A2	1.948	1.984	1.881

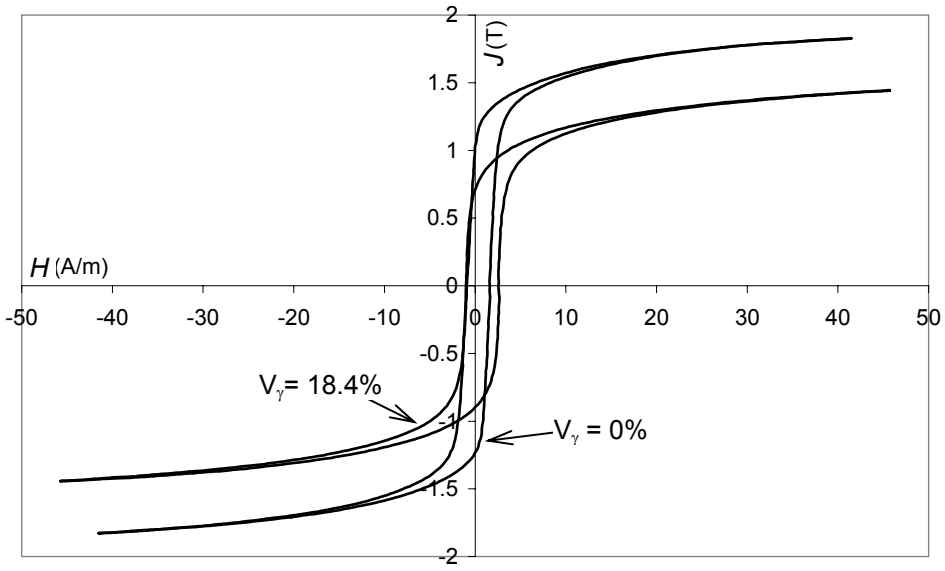

Fig. 3.5 The change in the hysteresis curve obtained due to the variation of the austenite content from 0% to 18.4% of alloy A1.

3.7 Mechanical Testing

The materials were machined to the required specimen size and geometry prior to heat treatment. This was done to avoid transformation of retained austenite to martensite due to machining forces. Standard tensile specimens according to ASTM, subsize E8-03, with a width of 6.35 mm and a gauge length of 25.4 mm were machined in transverse to the rolling direction from the cold rolled bands.

For the compression samples the same dimensions of the dilatometric sample were used (D5×10mm).

The tensile and compression tests were conducted in a computerised universal testing machine (UTS) with a cross head speed of 5 mm/min during tension and 1 mm/min during compression.

3.8 Thermodynamic Calculations

All the thermodynamic calculations were performed using the program Thermo-Calc using the database TCFE3 and considering the phases ferrite, austenite and cementite.

Chapter 4
Cold Rolled TRIP-steel: Results and Discussion

4.1 Introduction

The remarkable strength-ductility balance in TRIP steel results from the occurrence of the transformation induced plasticity (TRIP) phenomenon during deformation [Zac67]. The co-existence of austenite with a certain stability in the microstructure is of vital importance for the occurrence of this phenomenon and hence for the achievement of the desired properties. Retention of austenite is usually obtained by the combined effect of chemical composition and typical heat treatment. In this respect, adding large amount of silicon to TRIP steel ensure that cementite precipitation is not likely to occur in the microstructure during the formation of bainite [Mat87]. The absence of cementite ensures that the carbon will enrich the austenite rather than forming cementite plates. Therefore, after the course of bainite transformation, by further cooling the austenite is stabilised to RT. Jeong et al. concluded that austenite retention in these low-alloyed steels is almost impossible with silicon concentrations much below 1 wt% [Jeo92].

However, the high Si levels that are needed do not fit the industrial practice of flat products that is because:

1- Steel with more than 1% Si has the drawback of poor Zn coating quality after continuous galvanising due to the presence of Si-Mn oxides on the strip surface [Mak03].

2- The high Si-content of steel results in the formation of red scales in form of bands. After pickling the oxides are completely removed but the band remains visible on the surface of the pickled steel [Mar01].

As a consequence, studies have been performed on other elements that can play the role of silicon. Presently, aluminium seems to be the most promising candidate for substitution of silicon. However, together with the fact that high aluminium content in steel causes serious casting problems, a full substitution of silicon by equivalent amount of aluminium leads to a marked deterioration of the strength-ductility balance [Gir01, Jac01a]. De Cooman [Dec99] proposed that silicon can best be partially replaced by aluminium with increase in the carbon content. Bleck also suggested that the combination of silicon, aluminium

and phosphorus can be considered as a reasonable compromise and could be the most important alloying concepts for low alloyed TRIP steels [Ble04].
However, hardly any source can be found in literature about the effect of the aluminium-content, as a unique varying element, on the phase transformation and mechanical properties of the TRIP-aided steels. De-Meyer et al. [Mey99] and E. Emadoddin et al. [Ema06] presented some results about Si-Al alloyed TRIP steels. However, their comparison of the amount of phases and the mechanical properties is misleading since the carbon content was different in their alloys. Carbon is the main alloying element by which all transformations are noticeably affected and by which the final microstructure and the mechanical properties are controlled [Ble02]. On the other hand, without changing the alloys' carbon-content, Jacques et al. [Jac01a] studied the effect of partial substitution of Si by Al. However, in the latter source the Si content was variant.

4.1.1 Aim of the Study

This study is to enlighten the influence of varying the Al-content together with the prior hot-rolling conditions and heat treatment parameters on the microstructure and mechanical properties of the cold-rolled Mn-Si-Al TRIP-aided steel alloyed with Mo-Nb.

4.2 Investigated Materials

The Si-Al-Mo-Nb steel studied in this work was laboratory produced. The two alloys studied here, A1 and A2, differ by their Al content. The chemical composition is given in Tab. 3.1. The alloys contain Mo and are microalloyed with Nb. Nb in solid solution has been found to improve the TRIP properties; Mo retards the precipitation of Nb(C, N), thus potentially improving the effectiveness of Nb as a TRIP enhancer [Bou98, Jia02]. Furthermore, Mo has the retardation effect on the austenite transformation to both ferrite and pearlite rendering the process control more manageable [Cap05].

4.3 Hot Rolling Conditions

4.3.1 Estimation of T_{nRX}

When dynamic recrystallisation (DRX) takes place during deforming a material, e.g. rolling process, grain size is determined by the steady state flow stress.

Whenever the critical strain ε_c for the onset of DRX is reached and exceeded during hot deformation, a metadynamic recrystallisation (MDRX) takes place after interruption of straining, consequently coarsening the austenite grains. If deformation is interrupted before reaching the strain ε_c and if temperature is high enough, then static recrystallization (SRX) takes place. By deforming the material in the recrystallization region the austenite grains are being refined. This is important because the grain size of the austenite strongly affects both, the kinetic of subsequent $\gamma \rightarrow \alpha$ transformation and the ferrite grain size, namely smaller austenite grains consequently lead to the refinement of ferrite grains. When deformations are applied at temperatures below the temperature of non-recrystallization T_{nRX} the austenite grains become elongated and deformation bands are introduced within the grains. The process is called pancaking. As the amount of deformation in this region increases, the number of nucleation sites at the austenite grain boundaries and within austenite grains increase. Because of that, $\gamma \rightarrow \alpha$ transformation from deformed austenite yields in much finer ferrite grains than that from recrystallized, strain-free austenite. Therefore T_{nRX} is a very important parameter and its determination represents a crucial step in designing rolling schedules. Accordingly, the present hot rolling schedules have been selected according to this temperature.

T_{nRX} can be determined by the method proposed by Jonas and co-workers [Kar95, Bai93] which is based on multi-stage torsion test. In the present work we used this method, but the deformation was conducted by means of multistage compression test. Since the maximal strain of Bähr 805D deformation dilatometer is 1.2, six strain steps were selected each one of them $\varphi = 0.2$ with a strain rate $\dot{\varphi} = 6\ s^{-1}$. The stress-strain curves obtained are shown in **Fig. 4.1** and indicate that the level of stress depends on deformation temperature. Stress increases as temperature decreases, but this increment is higher at the last two deformation steps. On the other hand, there is higher work hardening rate observed on these two curves.

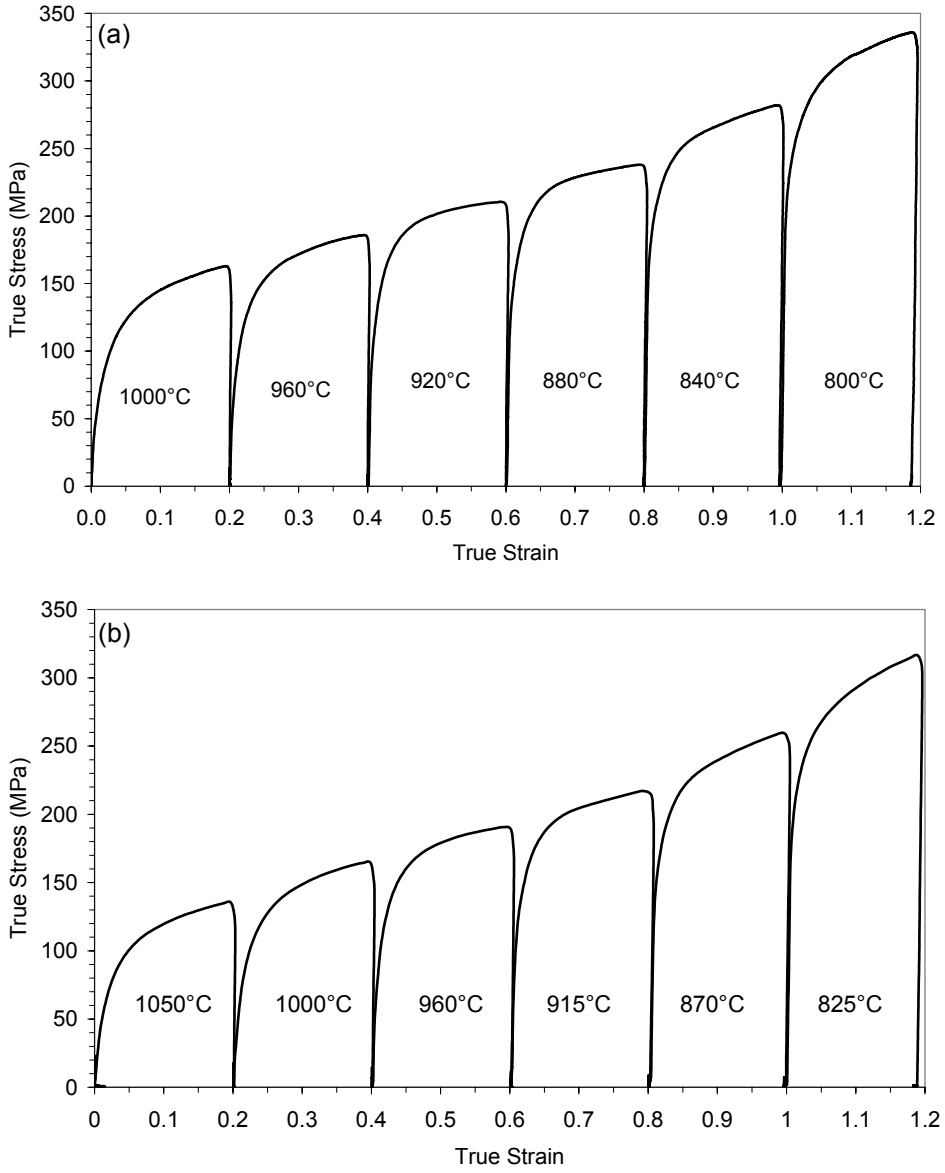

Fig 4.1 The true strain-true stress curves obtained in six-stage compression test for determination of the T_{nRX} temperature at a strain rate of 6 s^{-1} and temperature sequence denoted on the figure (a) alloy A1 (b) alloy A2.

The procedure of determination of T_{nRX} consists of calculating of mean flow stress, MFS, that corresponds to each deformation step. MFS is the area under the given stress-strain curve for selected interval divided by pass strain. The mean flow stresses for all the deformation steps have been calculated by numerical integration and the results are plotted as a function of inverse absolute temperature on **Fig. 4.2**.

From this graph the value of T_{nRX} can be determined by finding the intersection between the regression lines of the points that corresponds to each part of the

curve with two different slopes (cf. **Fig. 4.2**). The estimated values of T_{nRX} from **Fig. 4.2** are 864.7°C and 885.7°C for alloys A1 and A2, respectively.

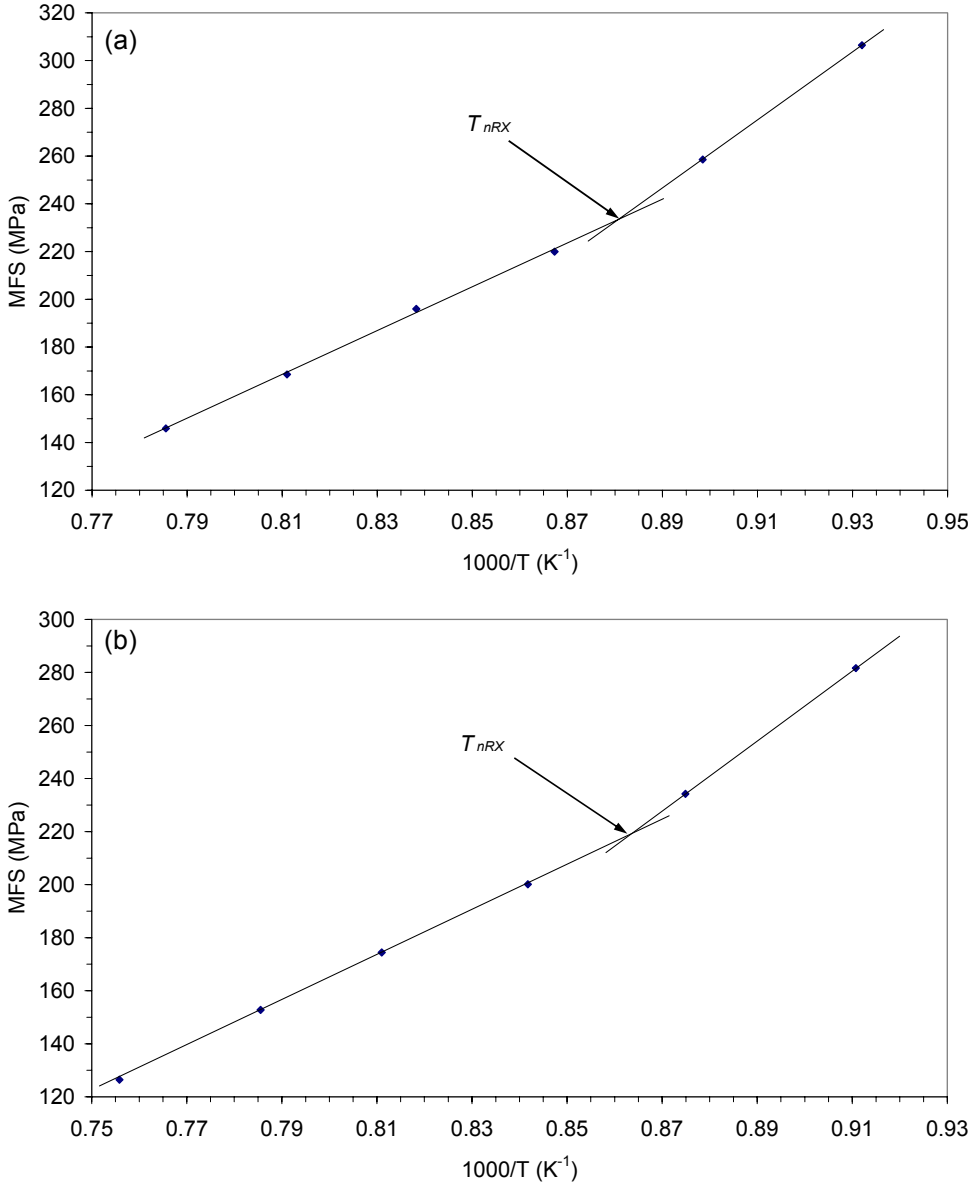

Fig 4.2 Dependence of the MFS on the inverse absolute temperature for alloys (a) A1 and (b) A2.

4.3.2 Hot Rolling Schedules

With these estimated temperatures, the deformation part for the schedules was determined in such a way that all the three possibilities were covered, namely all deformations conducted above the T_{nRX}, deformations below T_{nRX} and and deformations mixtures of below and above T_{nRX}. A schematic representation of the employed schedules is given in **Fig 4.3**. The schedule resulted in

microstructure formed from the recrystallized-austenite is denoted by “R”, whereas that resulted in microstructure formed from pancaked-austenite is denoted by “P”. The “RP” schedule is for the microstructure resulting from the recrystallized- and then pancaked-austenite.

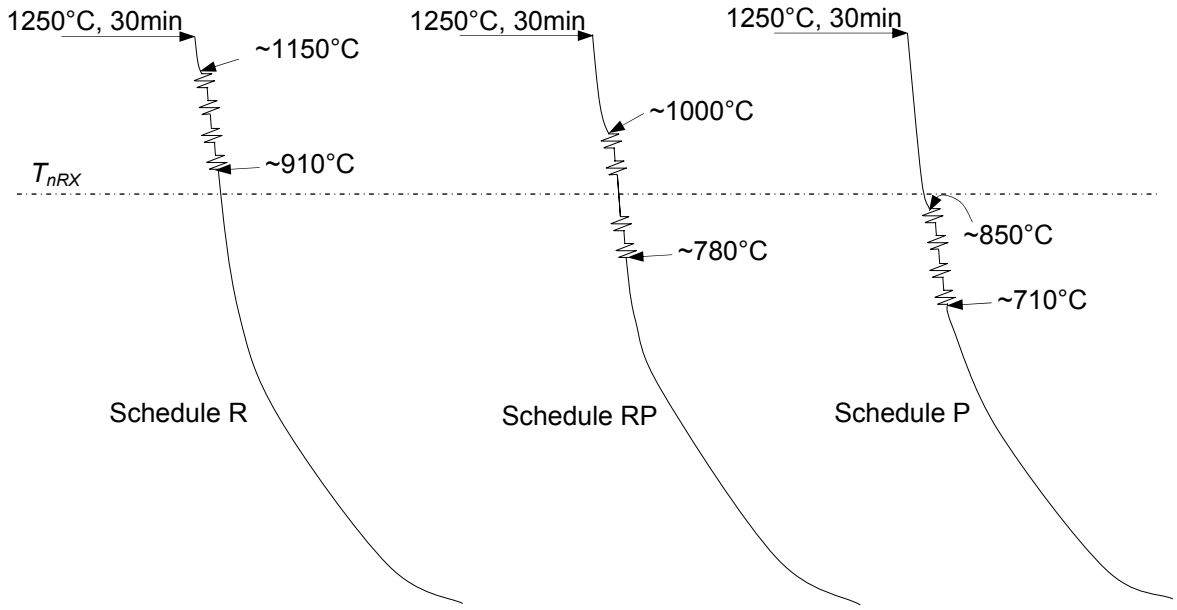

Fig. 4.3 Schematic representation of the employed hot rolling schedules.

A reheating temperature of 1250°C was selected to dissolve the Nb in solution. This temperature is sufficient to dissolve the *entire* Nb in solution as it is clear from the relevant solubility versus temperature curve, which was calculated using Thermo-Calc (cf. **Fig. 4.4**). The hot rolling took place in four passes from a thickness of 19 mm to 4 mm and with a true strain value φ = 0.38 at each pass. During the final cooling of the hot rolled strips in air, the temperature was continually monitored using a pyrometer. It took between 20 to 31 min to cool the strips from the finish rolling temperature to 400°C. The scales then were removed from the slabs using shot-blasting before being cold rolled to a thickness of 2.5 mm.

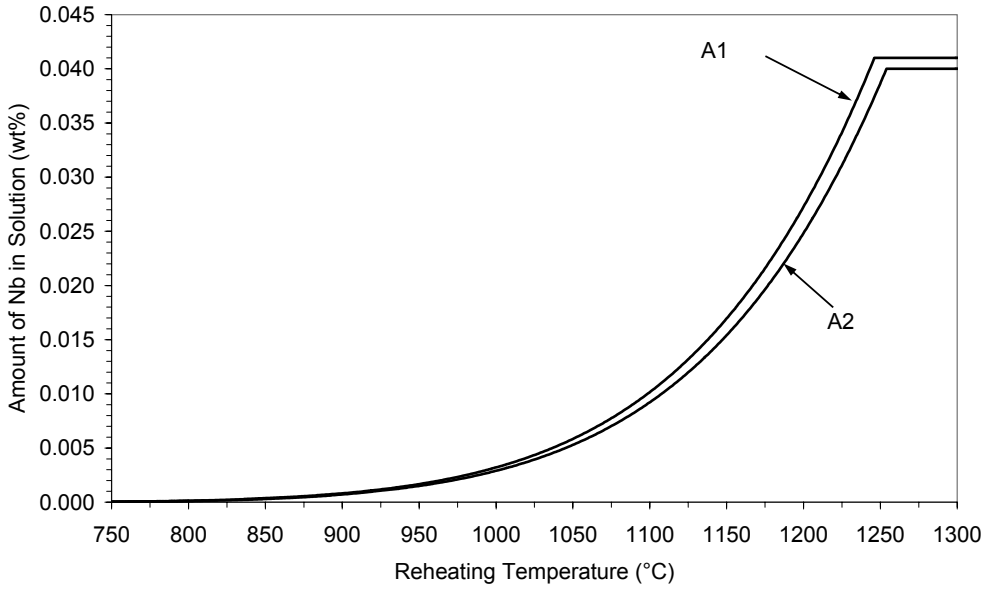

Fig. 4.4 Dependence of the amount of Nb that goes under equilibrium into solution on the reheating temperature.

Fig. 4.5 and **Fig. 4.6** show the microstructure obtained after the different hot-rolling schedules. As can be seen, acicular ferrite is dominant with polygonal ferrite. The acicular ferrite matrix is characterised by its non-equiaxed ferrite grains. A remarkable characteristic of this type of microstructure is that it possesses a unique and irregular configuration, which has various size grains distributed in a chaotic manner with random orientations. The polygonal ferrite grains are equiaxed with different average sizes dependant on the applied rolling schedule.

Tab. 4.1 compares the ferrite contents (Fer. %) and their grain sizes (d_f) being observed due to the different hot-rolling schedules for both alloys. The higher ferrite content of steel A2 can be explained by its lower hardenability. That is because the increase in the Al-content results in shifting the ferrite-nose of the CCT diagram towards lower time (cf. **Fig. 2.6**). It is also observed that the hardenability is sensitive to deformation temperature. Decreasing the deformation temperature decreases the steel hardenability and hence the ferrite-content increases by moving the deformation schedule towards lower temperature.

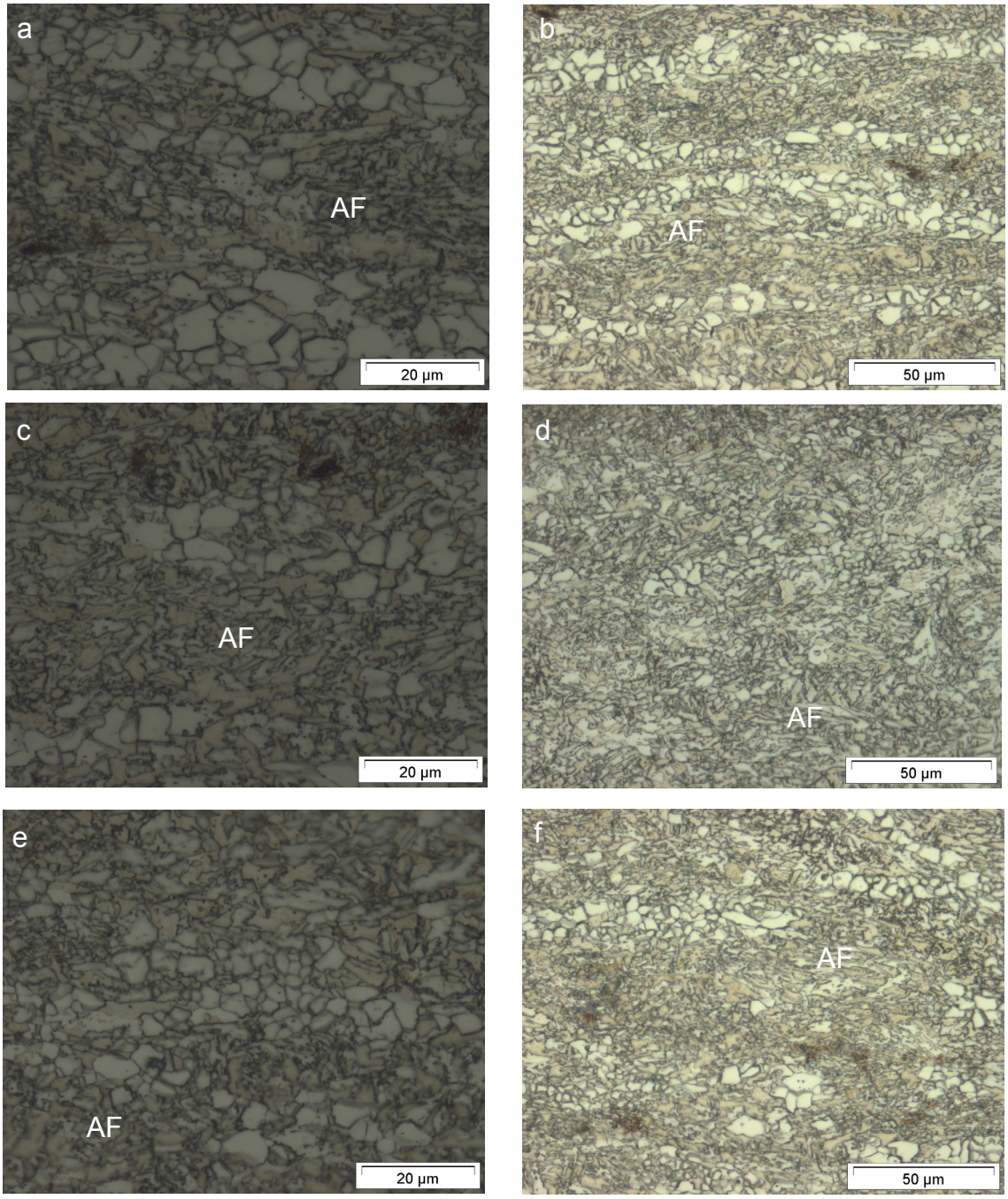

Fig. 4.5 Structure refinement as a result of applying different rolling schedules on alloy A1- microstructures (“a” and “b”), (“c” and “d”) and (“e” and “f”) resulted from applying schedules R, RP and P, respectively (etchant: nital). Micrographs taken at the middle section of the hot-rolled material (AF: acicular ferrite).

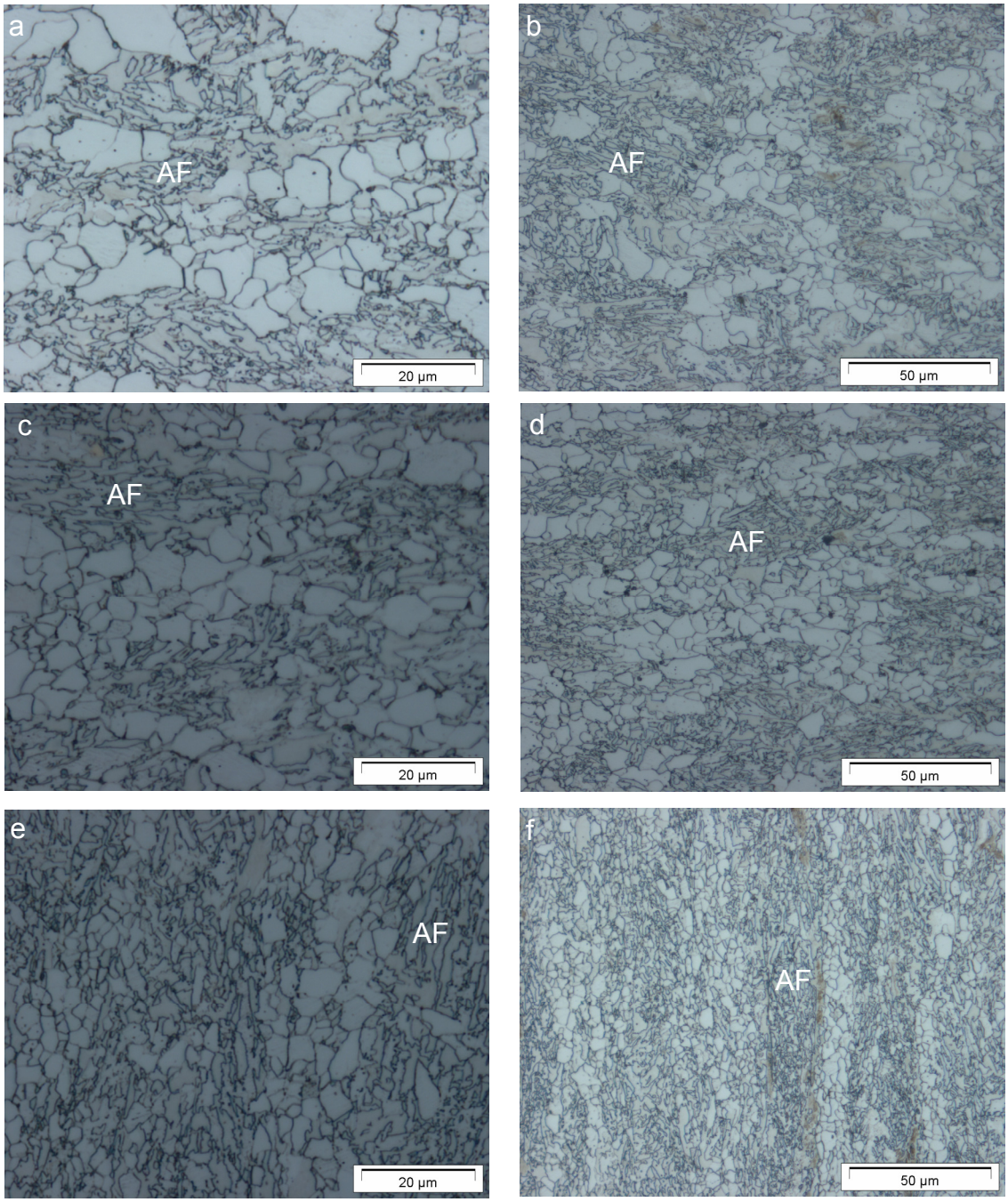

Fig. 4.6 Structure refinement as a result of applying different rolling schedules on alloy A2- microstructures (“a” and “b”), (“c” and “d”) and (“e” and “f”) resulted from applying schedules R, RP and P, respectively (etchant: nital). Micrographs taken at the middle section of the hot-rolled material. (AF: acicular ferrite).

Tab. 4.1 Effect of hot-rolling schedule on the ferrite percentage (Fer. %) and ferrite grain size (d_f) μm for alloys A1 and A2.

Sched. / Alloy	R		RP		P	
	Fer. %	d_f	Fer. %	d_f	Fer. %	d_f
A1	40.8	8.1	52.3	6.8	61.2	4.5
A2	52.1	8.9	65.3	7.0	78.2	4.4

On the other hand, the variation in the ferrite grain size with varying the hot-rolling schedule is due to the difference in the morphology of the austenite grains from which the ferrite is formed. For the P-schedule the grains are produced from work hardened (pancaked) austenite through austenite to ferrite transformation. The sizes of these ferrite grains are smaller than those produced from the recovered and recrystallized austenite grains of the R-schedule. It is well known that ferrite tends to nucleate at the austenite grain boundaries [Bra77, Bel04]. Thus, the ferrite grain size developed after the transformation strongly depends upon the austenite grain structure that appears just before the start of transformation. During straining austenite in non-recrystallization region, deformation bands, and twinning boundaries form and the dislocation density inside austenite grains is greatly increased which provided favourable nucleation sites and enhanced nucleation rate. The grain refinement effect of deformation in the non-recrystallisation region is greater than that in the recrystallisation region [Qu02, Egh06]. The higher austenite decomposition kinetics causes the faster nucleation rate of ferrite. Non-recrystallized austenite transforms to ferrite at a faster rate than recovered or recrystallized austenite owing to two effects [Egh06]:

(1) the higher internal energy of the deformed and thus less stable austenite

(2) the larger number of nucleation sites provided by defects.

4.4 The Intercritical Annealing Conditions

During the current investigation the transformation kinetics had been studied using the dilatometer. All the dilatometric measurements were performed using 2.5×5×10 mm samples. Unless mentioned, the dilatometric tests were performed on samples from cold-rolled strips of the RP-materials.

4.4.1 Continuous Heating Transformation (CHT)

In order to define the intercritical region, dilatometric measurements were applied by heating specimens up to 1100°C. Increasing the heating rate resulted in increasing the Ac1 as well as Ac3 as shown in **Fig. 4.7**.

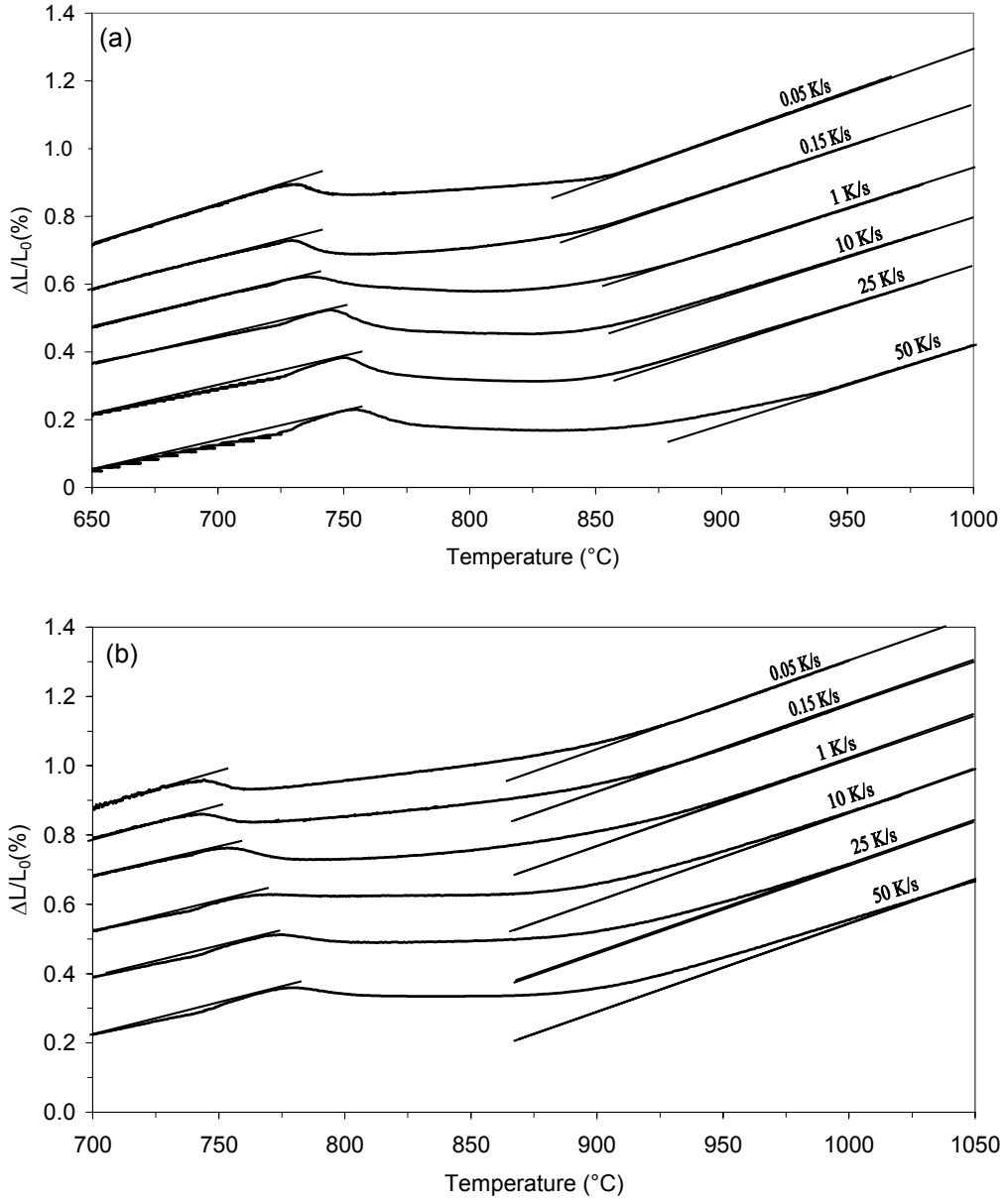

Fig. 4.7 Dilatation versus temperature curves observed during continuous heating for alloys (a) A1 (b) A2.

The Ac1 and Ac3 temperatures are plotted in the continuous heating transformation (CHT) diagram in **Fig. 4.8**. These data indicate that the heating rate exerts a stronger influence on the finish temperature, when all the ferritic phase is exhausted, than on the start temperature at the beginning of carbide dissolution. On the other hand, the dependence of transformation temperature on the heating rate is decreasing as the heating rate decreases. For the very slow heating rate the Ac1 and Ac3 are independent on the heating rate. This feature is associated with the transformation temperatures under equilibrium Ae1 and Ae3 which depend only on the chemical composition, i.e. independent on the heating or cooling rates [Gar02]. An inference is that at the heating rate where the transformation temperatures start to be independent on the heating rate, the Ac1 and Ac3 are closed to the Ae1 and Ae3. In this context fine grain size resulted from the hot- and cold-rolling processes favour the transformation process in such a way that very slow heating rate, slower than 0.05 K/s, is not required to trace the equilibrium points. This is because the greater density of nucleation sites, resulted from the fine grained structure, enhances the transformation kinetics.

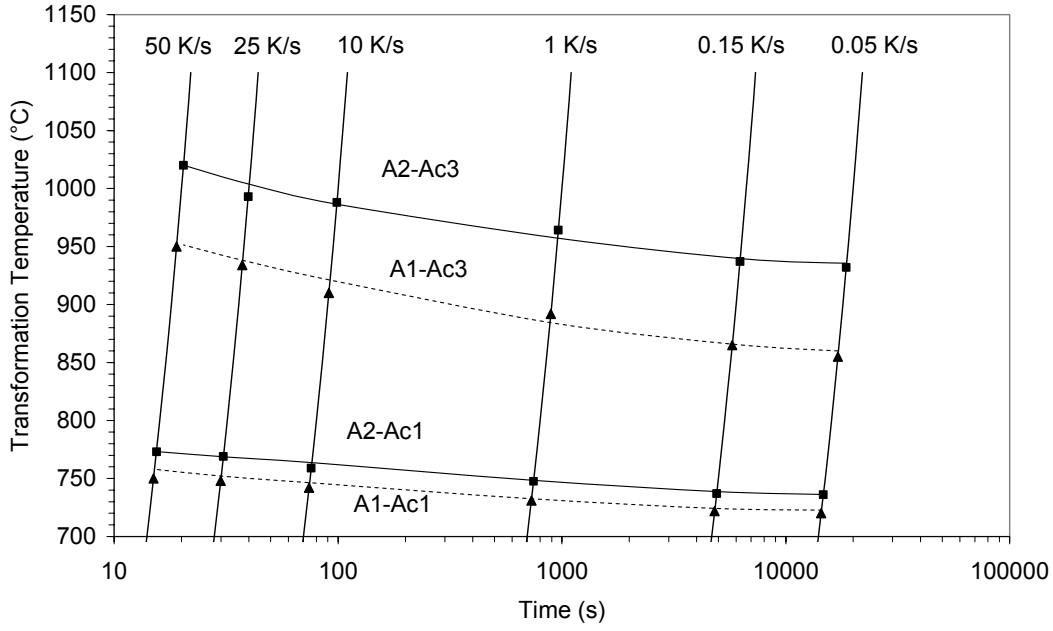

Fig. 4.8 The CHT diagram of alloy A1 and A2.

4.4.2 Phases in Equilibrium

From the variation of the relative change in length as a function of temperature the formed austenite fraction (f_γ) were calculated employing the lever rule. The results for both steels are shown in **Fig. 4.9**. Depending on the previous discussion, for better tracing of the equilibrium points, the dilatation curve of the 0.05 K/s was used for these calculations.

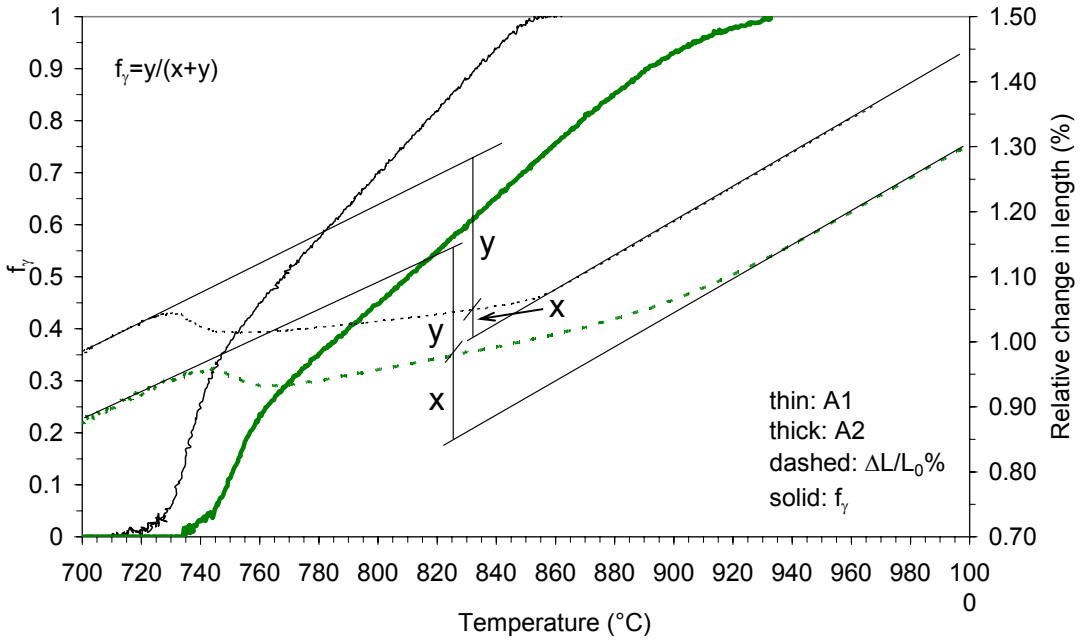

Fig. 4.9 Dilatation versus temperature curves observed during continuous heating together with the calculated formed austenite fraction (f_γ).

Fig. 4.10 compares the measured formed austenite fraction with that one predicted using the Thermo-Calc TCW3 software. The predicted dependence of the ferrite and cementite on the temperature is also shown in this figure. During the continuous heating of steels, it is reported that the transformation takes place starting by growth of austenite into the carbide rich areas and then subsequently by growth of austenite into ferrite and redistribution of carbon between the former and the latter [Jeo85, Dem02]. For both of the predicated and measured transformation kinetics, a clear demarcation of the two steps can be seen in **Fig. 4.10**. The change in slope of the line representing the dependence of f_γ on the annealing temperature corresponds to the change in the mechanisms of austenite formation.

On the other hand, at the beginning of transformation (near to Ae1), the measured kinetics is slower than the predicted one, for both alloys. However,

this difference decreases gradually with increasing the transformation temperature. The predicted and the measured transformation kinetics are almost identical at the end of transformation near to Ae3. The reason for this difference could be the sluggish kinetics of austenite formation at low temperature near to Ae1 [Dem02].

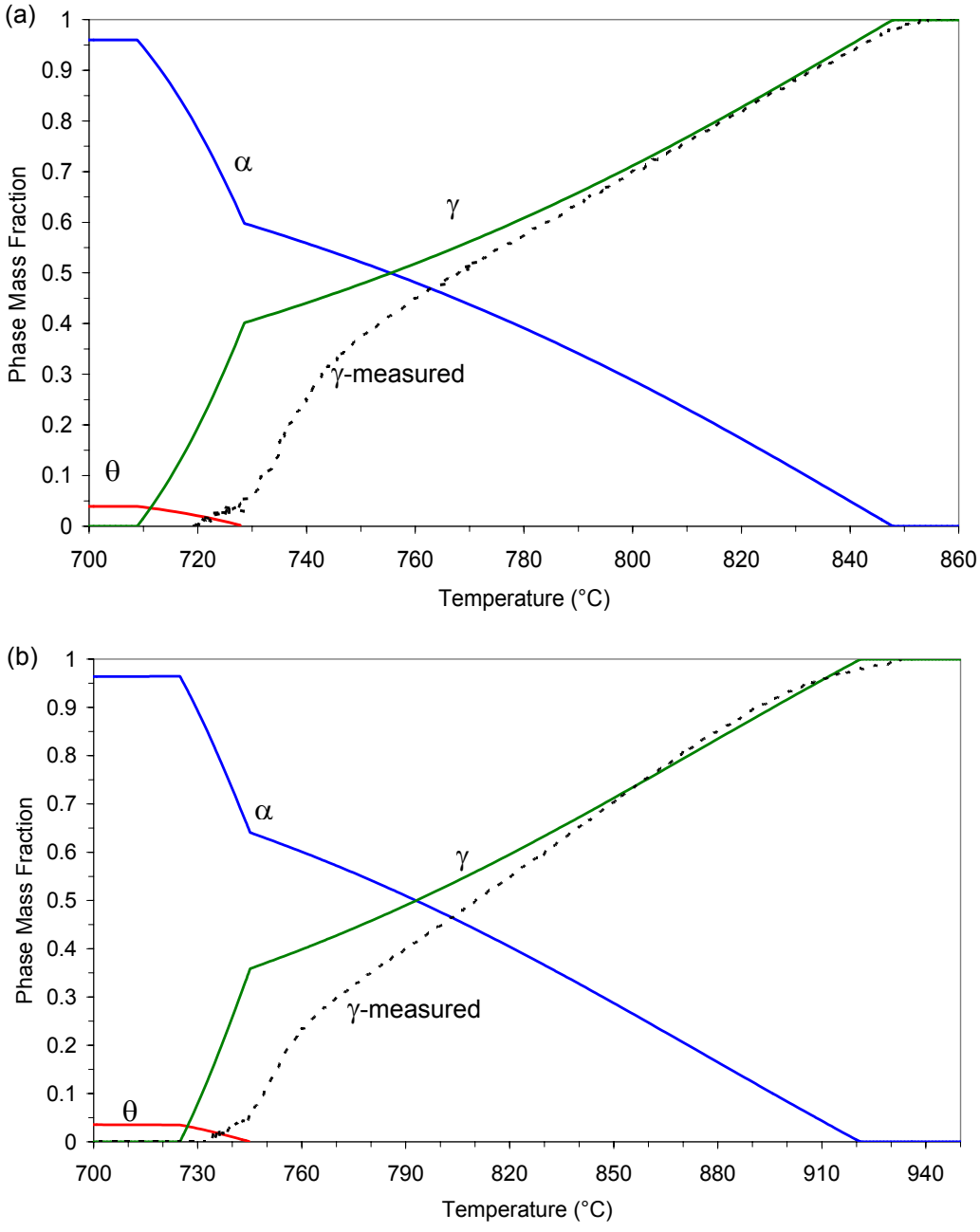

Fig. 4.10 The solid lines represent the predicted dependence of the phases in equilibrium on the annealing temperature (calculated using Thermo-Calc). The dashed line represents the measured one for the γ-phase. (a) alloy A1 (b) alloy A2.

4.5 Heat Treatment and Microstructure Formation

The intercritical annealing temperature was chosen on the basis of the dilatometric measurement shown in **Fig. 4.10**. A phase content of 70%, 50 % and 30% polygonal ferrite (PF) was required at the end of intercritical annealing. In equilibrium conditions this phase distribution is obtained in the intercritical annealing temperatures (T_A) shown in **Tab. 4.2**. For the heat-treatment processes the salt baths mentioned in section 3.2 were used. The intercritical annealing temperatures listed in **Tab. 4.2** were implemented in combination with austempering temperatures, T_B, of 365°C, 400°C and 435°C. After austempering the samples were quenched into water.

Tab. 4.2 Intercritical annealing temperatures (T_A) for alloys A1 and A2 (°C)

	70% PF	50% PF	30% PF
A1	742	768	800
A2	770	810	849

4.5.1 Microstructure Evolution

Microstructural evolution of both alloys intercritically annealed for 8 min at the temperature corresponding to PF content of 30% (**Tab. 4.2**) was studied along isothermal holding at 400°C. Depending on the bainitic holding time, various mixtures of bainite, martensite and retained austenite can be found in the microstructure after quenching. **Figs. 4.11** and **4.12** illustrate the different microstructures with micrographs corresponding to bainite holdings of 60, 120, 300 and 480s. The LePera etchant revealed the ferrite blue or light brown bainite brown while the martensite and the retained austenite (A/M) remained white. During the bainite holding the intercritical austenite progressively transforms to bainite, bringing about a larger stabilization of austenite. According to the stability of the austenite, a certain part retains at RT, whereas the remaining part transforms to martensite. For both retained austenite and martensite appeared in white colour, the white areas of **Figs. 4.11** and **4.12** represent the non-transformed austenite during the bainite holding stage. Accordingly, the gradual decrease in the white area of the figures corresponds to the progress of the bainite-reaction.

In addition to the metallographic investigations, the retained austenite volume percentage (V_γ) was measured using the magnetic method for the different intercritical annealing conditions along the isothermal holding at 400°C. **Fig. 4.13** shows the V_γ as a function of the austempering time for the two steels. This figure shows that the V_γ decreases by increasing the austempering-time. It is also noted that for the steels intercritically annealed to 30% and 50% PF-contents, the dependence of the V_γ on the austempering-time decreases by increasing the transformation-time.

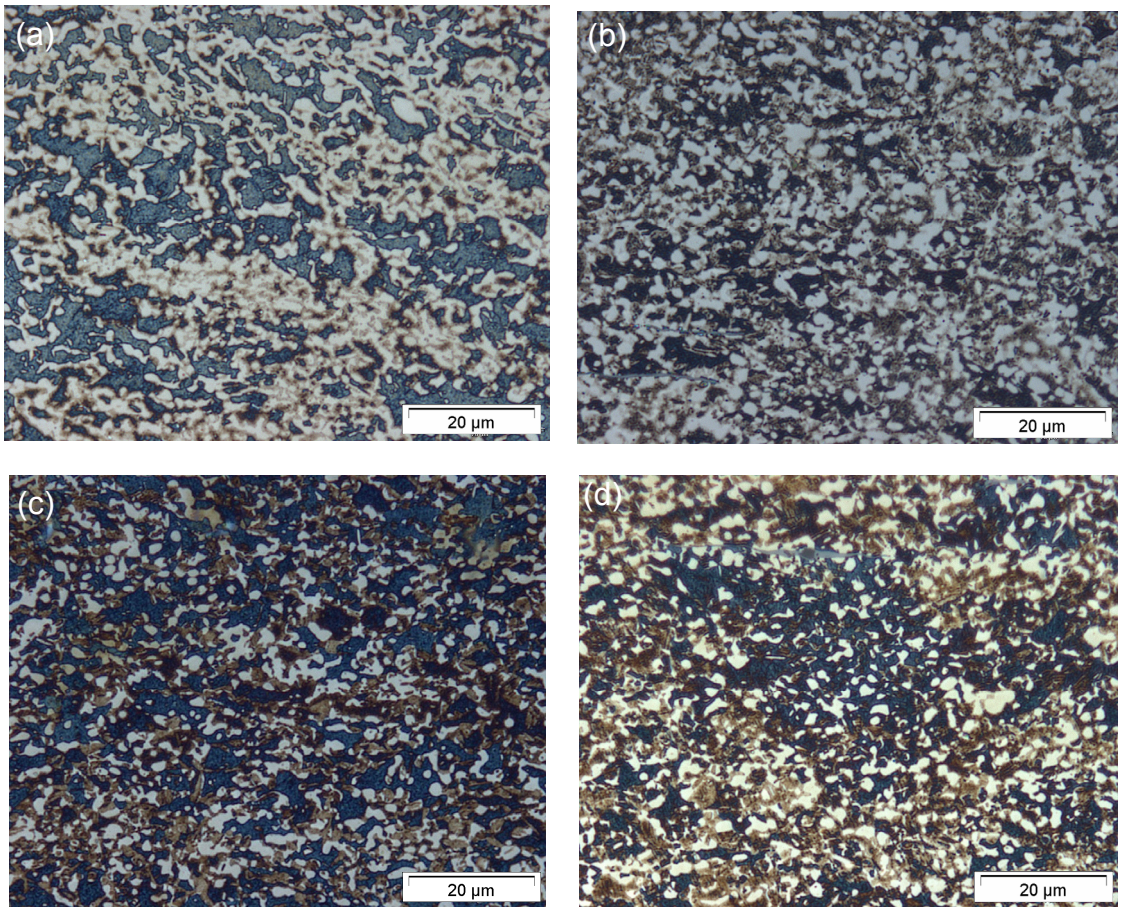

Fig. 4.11 Microstructure of alloy A1 observed after annealing at 800°C for 8 min and isothermal transformation at 400°C for (a) 60 s, (b) 120s, (c) 300s and (d) 480s.

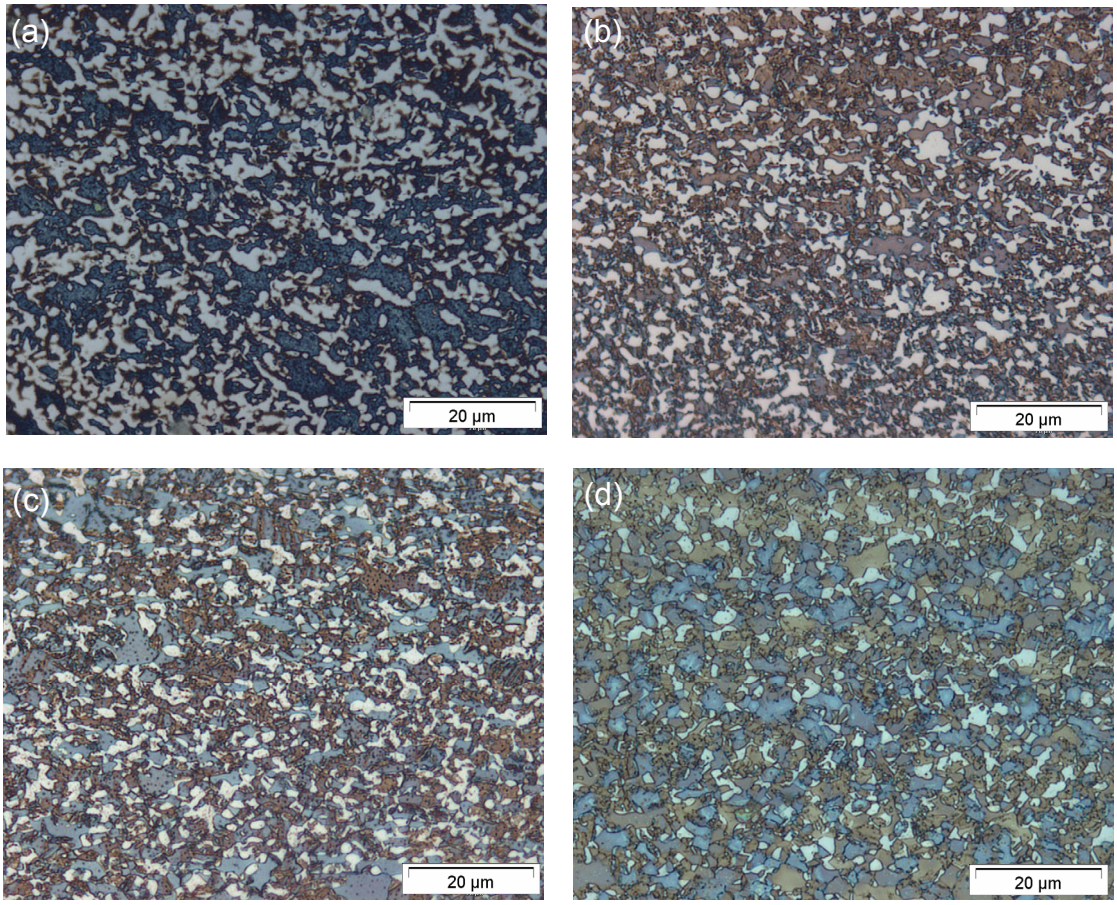

Fig. 4.12 Microstructure of alloy A2 observed after annealing at 849°C for 8 min and isothermal transformation at 400°C for (a) 60 s, (b) 120s, (c) 300s and (d) 480s

Referring to **Figs. 4.10** to **4.13**, the difference between the A/M% in the photomicrographs and the V_γ represents the martensite phase. Because the austenite is less stabilized at the beginning of the bainite-reaction more martensite phase is expected which increases the difference between the white areas in the figures and the V_γ. However, proceeding in the bainite-reaction is accompanied by carbon enrichment of the austenite. The latter is gradually stabilised and simultaneously decreases in quantity during the course of bainite-reaction. The former effect results in decreasing the martensite phase and hence decreasing the difference between the A/M% and the V_γ.

Moreover, the dilatometric measurements were used to compare the bainite transformation kinetics of the two steels. During the dilatometric tests, a cooling rate of 50K/s was used to quench the samples from T_A (**Tab. 4.2**) temperature to 400°C.

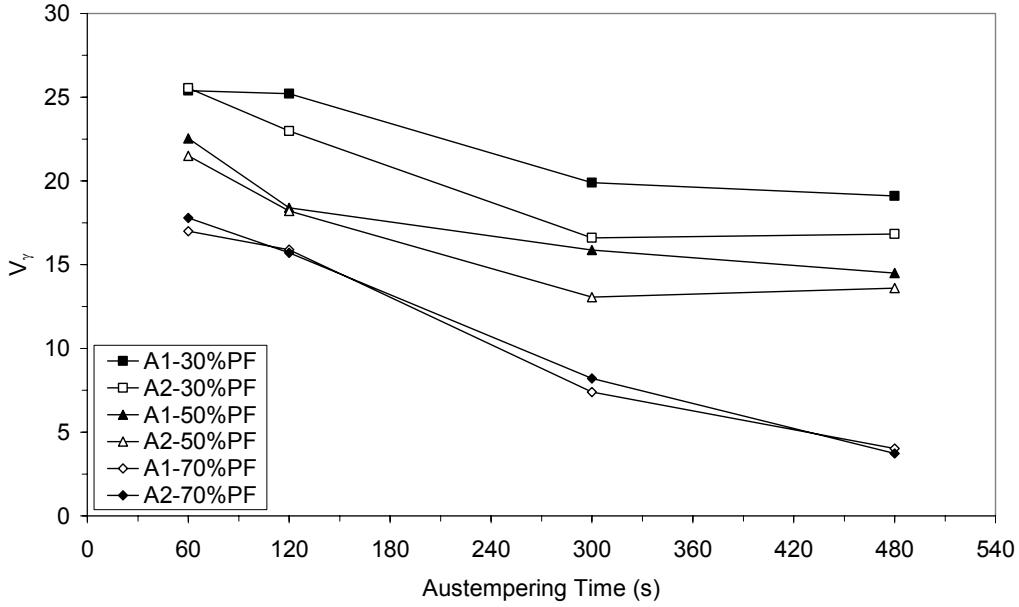

Fig. 4.13 V_γ as a function of the austempering time at 400°C – the material is intercritically annealed to different PF-contents.

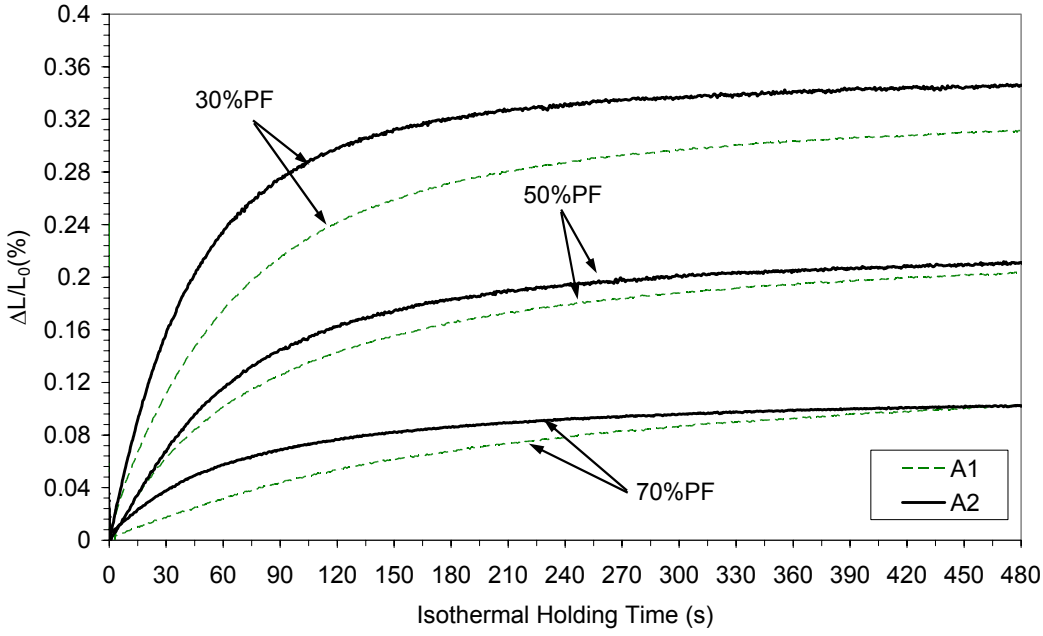

Fig. 4.14 Dilatation curves of alloys A1 and A2 bainitically transformed at 400°C.

Fig. 4.14 compares the dilatation curves of alloys A1 and A2 bainitically transformed at 400°C. The bainite-reaction proceeds to a higher final amount of bainite for the higher Al-content alloy. **Fig. 4.14** demonstrates also that the bainite formation is accelerated by increasing the aluminium content (considering the same PF-content). Thermo-Calc calculations of the driving

force for the transformation of austenite into ferrite ($\Delta G^{\gamma\alpha}$) for alloys A1 and A2 (cf. **Fig. 4.15**) confirm the thermal dilatometric results. Thus, the microstructure evolution throughout the isothermal bainite transformation demonstrated that both, bainite formation rate and its total amount, increase as a result of increasing the aluminium content.

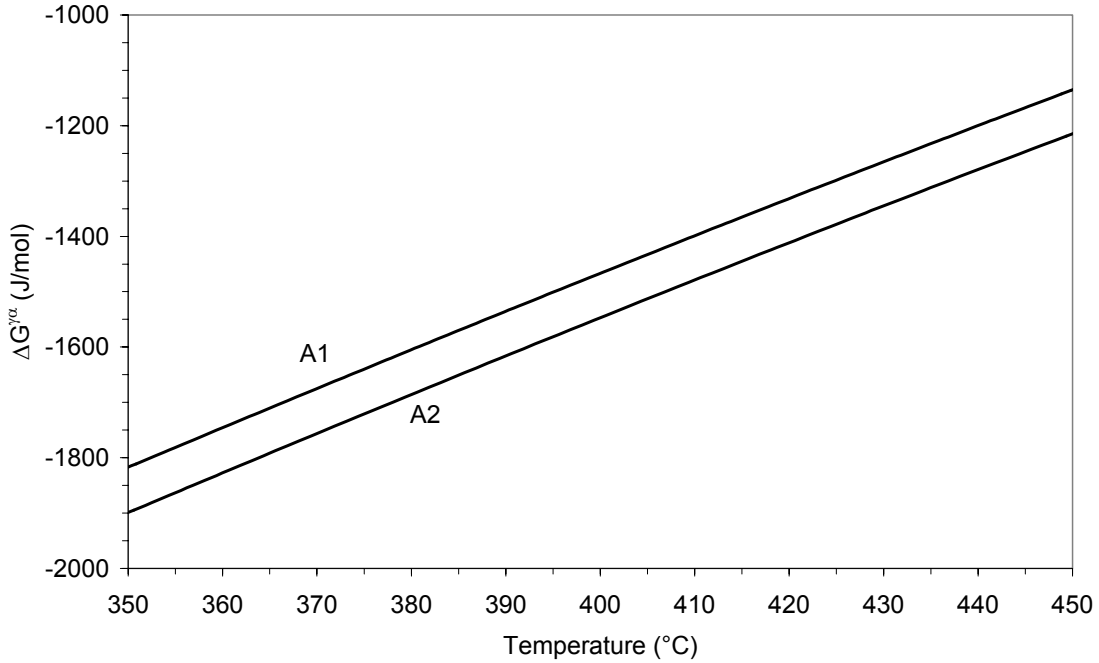

Fig. 4.15 Calculated driving force of transformation from austenite into ferrite ($\Delta G^{\gamma\alpha}$) for alloys A1 and A2.

On the other hand, the dilatometric experiments have shown that a cooling rate of 50 K/s is sufficient to avoid the formation of the allotriomorphic ferrite during cooling to the T_B. This has been detected from the linearity of the temperature-dilatation curve observed during cooling.

4.5.2 Effect of Heat-treatment Conditions

The T_A listed in **Tab. 4.2** was used in combination with austempering temperatures T_B of 365°C, 400°C and 435°C. The isothermal holding time for both of the two steps were 8 min. Representative microstructure results using the same magnification are shown in **Fig. 4.16**. In all specimens the minor microstructure is the austenite/martensit (A/M) structure.

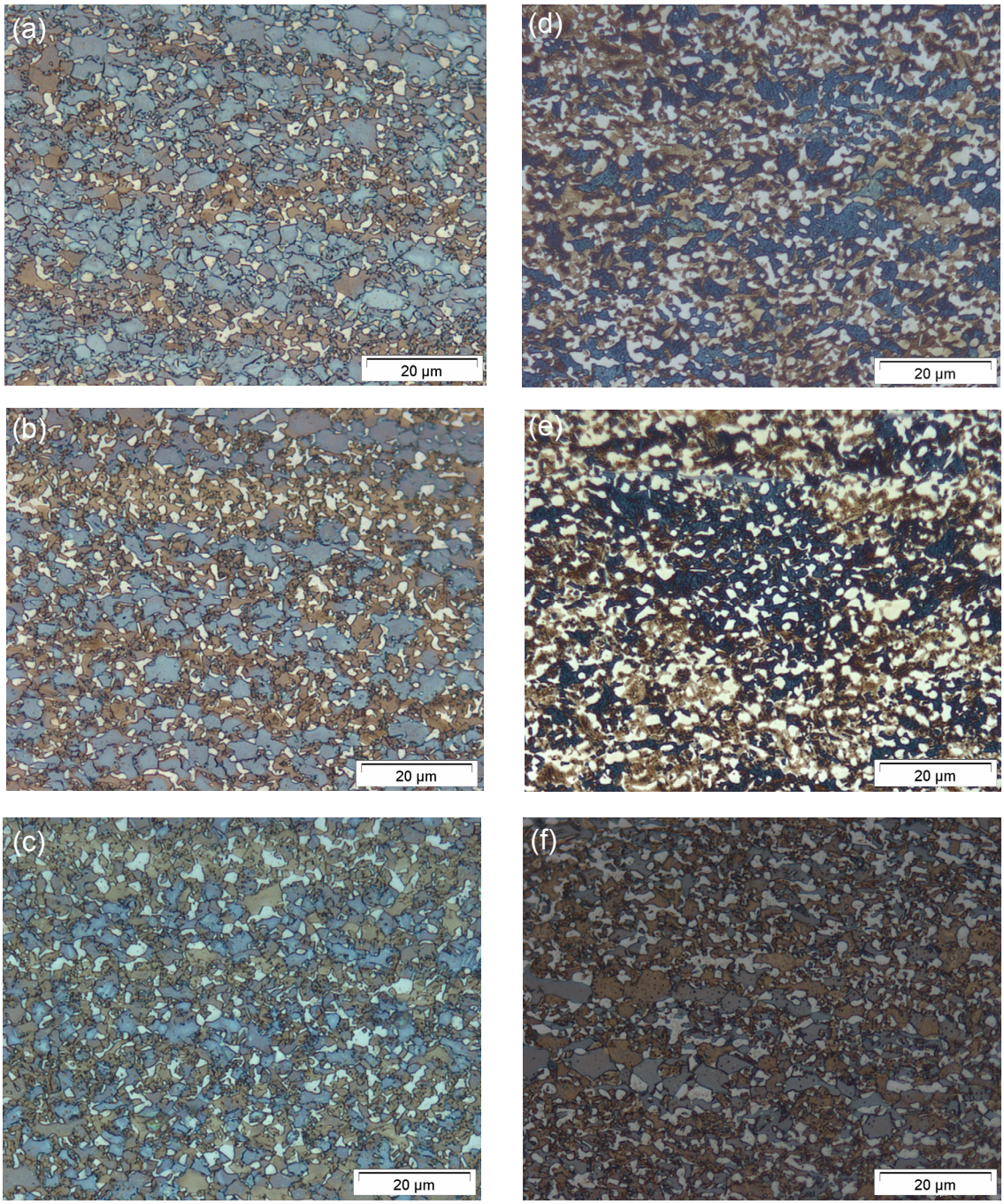

Fig. 4.16 (a) to (c) Alloy A2; austempering temperature 400°C – intercritically annealed at (a) 770°C, (b) 810°C and (c) 849°C – **Fig. 4.16** (d) to (f) of alloy A1; intercritically annealed at 800°C and austempered at (d) 365°C (e) 400°C and (f) 435°C.

Figs. 4.16 a to **c** show the influence of the intercritical annealing temperature on the microstructure of alloy A2 for specimens austempered at 400°C. Increasing the intercritical annealing temperature resulted in decreasing the PF amount to reach approximately the foreseen amount (70%, 50% and 30%). A concurrent increase in the amount of the A/M phase (white areas) is observed.

On the other hand, the intercritical annealing temperature has no significant effect on the grain size of ferrite and retained austenite. Similar observation has been reported by Shi et al. [Shi06]. The grain sizes of ferrite and retained austenite varied between 3-7 μm and 0.7-3 μm, respectively. On the other hand, a significant influence of the chemical composition and austempering temperature on the location and morphology of the retained austenite could not be detected.

Also **Fig. 4.16** shows that the structure is fully recrystallized. In consistence with that, for their studied cold rolled TRIP-aided steels, Petrov et al. has not observed any interaction between recrystallization and transformation phenomena as the static recrystallization was already completely finished before the start of the $\alpha \rightarrow \gamma$ phase transformation [Pet01].

Fig. 4.17 shows that decreasing the PF amount (increasing the intercritical annealing temperature) has led to a higher amount of V_γ in the final microstructure for the two alloys. This could be attributed to the higher intercritical austenite content.

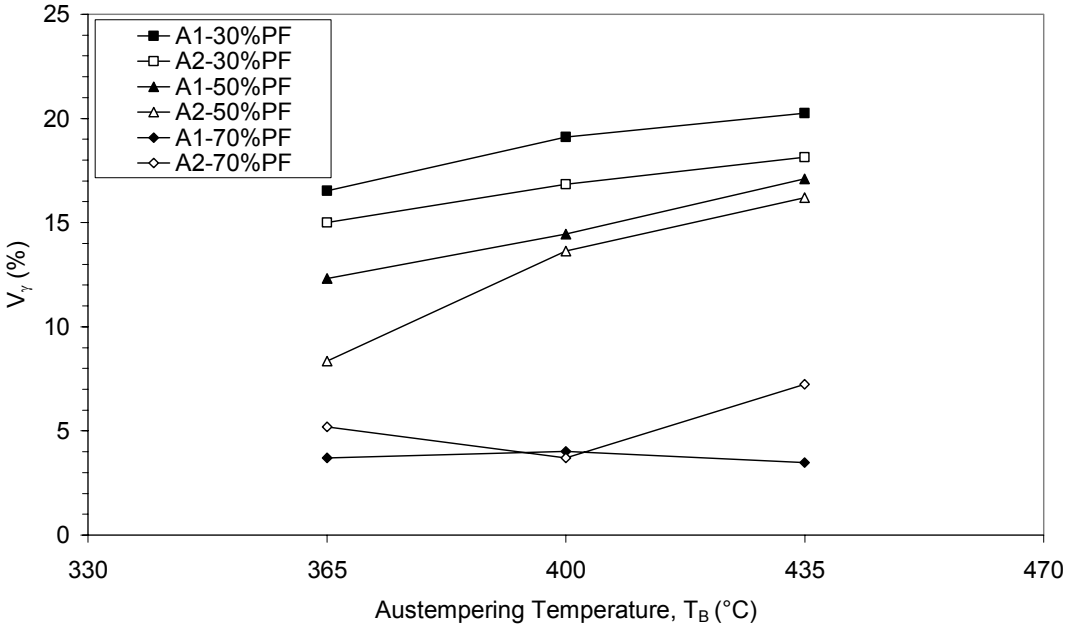

Fig. 4.17 Effect of annealing conditions on the retained austenite percentage.

On the other hand, for the alloys annealed to a foreseen PF% of 50% and 70%, increasing the T_B temperature from 365°C to 435°C resulted in increasing V_γ.

For these intercritical annealing conditions, it is also noted that the alloy of higher aluminium content (A2) has lower V_γ compared with that of lower aluminium content.

These two observations were not recorded for the materials intercritically annealed for a foreseen PF% content of 70%. Such results for V_γ can be justified by following up the austenite and its composition throughout the heat-treatment process. This is described as follows: During the intercritical annealing stage, the austenite is firstly enriched with carbon due to the partitioning of the latter between the ferrite grains and the intercritical austenite (γ_i) during the formation of γ_i. The dependence of the elements concentrations in the intercritical austenite on the PF-content (i.e. T_A) is given in **Fig. 4.18** (using Thermo-Calc). During the course of the second isothermal holding (austempering) the austenite is further enriched with the carbon rejected from the bainitic-ferrite. This reaction can take place until reaching a point in which the free energy of ferrite is equal to the free energy of austenite ($G_\alpha = G_\gamma$) and thus at this point no further transformation of austenite to ferrite can take place. This residual austenite, because of its high carbon content, has a martensite start temperature (M_S) below RT and thus a certain amount of austenite from this process can be retained at RT. The amount of carbon that can enrich the austenite during this process has been found to be dependant on the isothermal austempering temperature according to the T_0 concept [Bha01]. **Fig. 4.19** shows the T_0 curve drawn for both, A1 and A2 alloys using Thermo-Calc software (TCCQ). However, the amount of carbon that enriched the V_γ is not necessarily matching that one expected by the T_0 curve. If the holding time for example is not sufficient to reach the T_0 curve, especially for the low austempering temperatures which require long holding time, the expected carbon concentration value can not be reached. On the other hand, for a high holding temperature the carbides can form easily and the carbon in austenite decreases [Has04]. It has been reported that carbide starts to precipitate between 450°C and 475°C and this temperature range is hardly affected by the chemical composition [Tra02b].

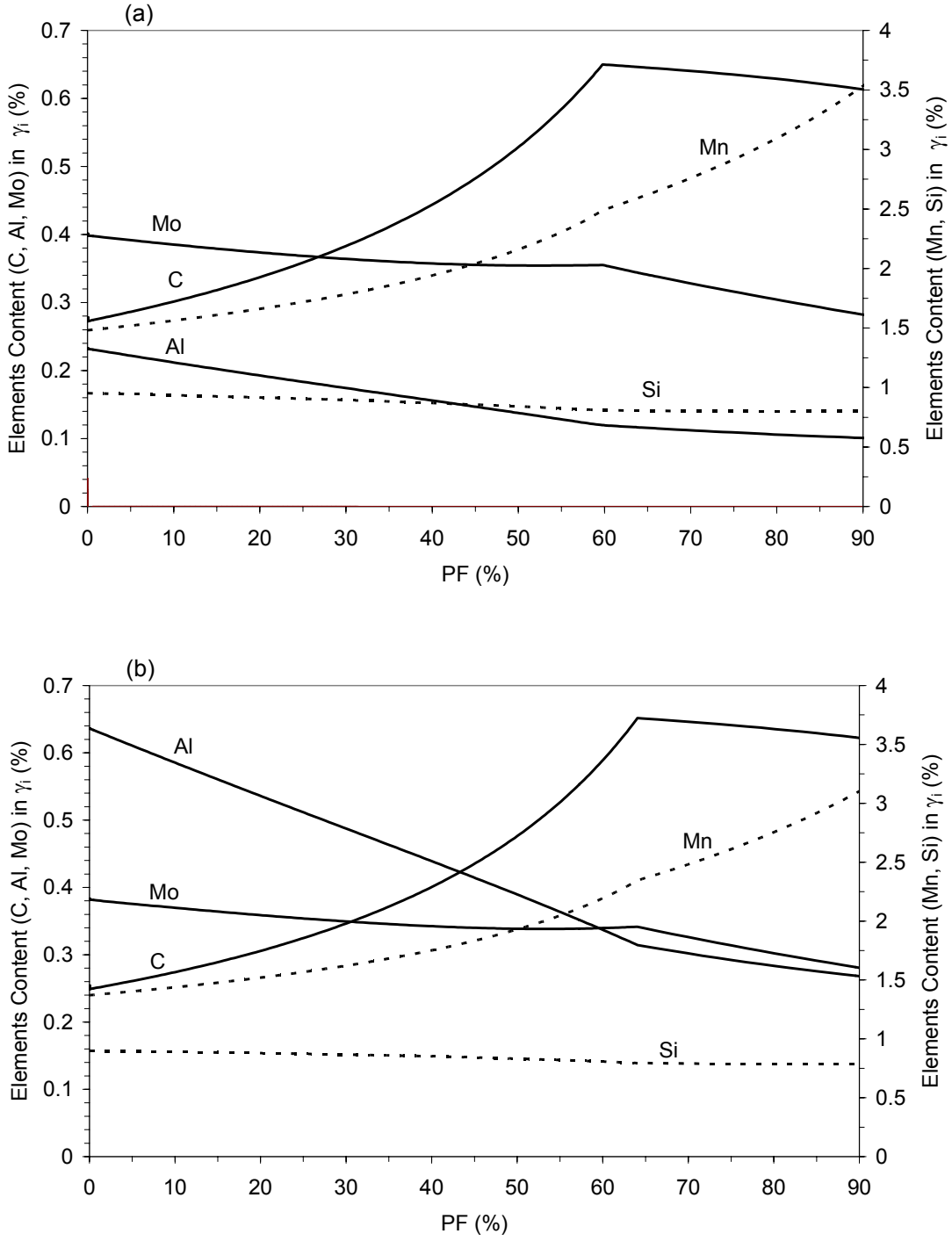

Fig. 4.18 Predicted dependence of the alloying elements in γ_i on the PF content in the intercritical region for alloys (a) A1 and (b) A2.

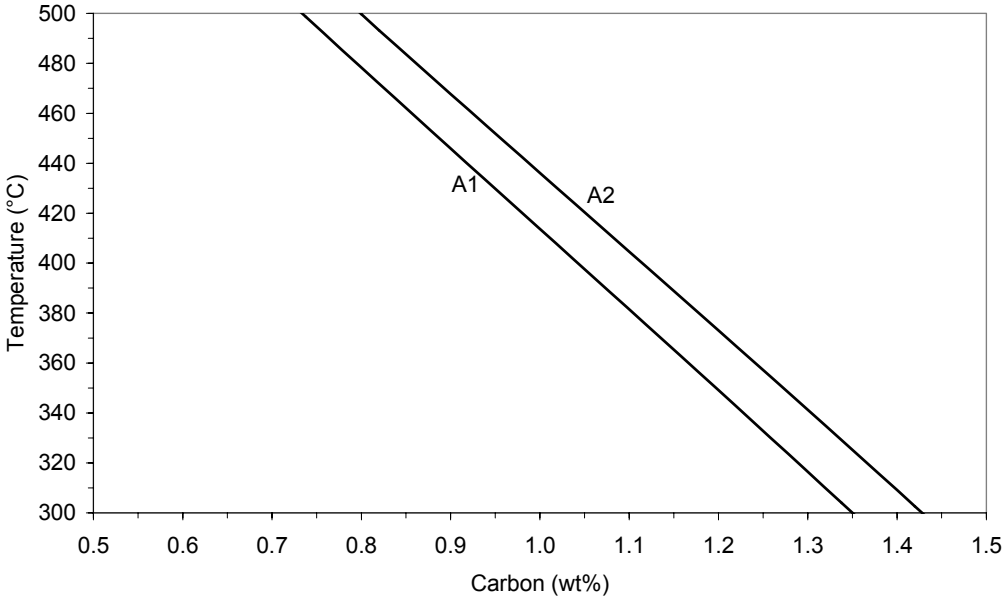

Fig. 4.19 The T_0 curves of alloys A1 and A2.

For the current case, considering the same amount of γ_i at the beginning of the bainitic transformation, the bainitic reaction will last to a lower concentration of carbon at higher temperature. Thus the final austenite will have a lower carbon concentration (**Fig. 4.19**) but higher amount (**Fig. 4.17**). The used relatively narrow austempering temperature range around 400°C is the reason why the results could be justified in the light of T_0 curve. It is reported by Hashimoto that at this temperature (400°C) the best combination of bainite transformation rate and carbon-content at T_0 curve occurs [Has04]. However, the trend is possibly not to continue for lower or higher austempering temperatures, where the carbon in the retained austenite may not fit with the T_0 curve due to the insufficient holding time or the carbide precipitation, respectively, as explained in the previous paragraph.

The V_γ of the 70% PF material does not follow the trend expected from the T_0 curve. In this case the γ_i is enriched with the carbide former elements (C and Mn), whereas the carbide suppression element (Al) is at lower level (cf. **Fig. 4.18**). This can motivate the carbide formation in bainite. Carbide formation taking place in austenite withdraws carbon from the austenite so its stability drops noticeably. This may proceed to an extent that some of the austenite formed during the isothermal holding can not be stabilized down to RT and thus transforms to martensite. Furthermore, Kim et al. have reported that the improvement of the austenite hardenability because of the high Mn content

(2.52wt% in their case) results in martensite transformation during cooling after the isothermal bainite holding [Kim01]. For the material annealed to 70% PF, similar excessive Mn-content is predicted in γ_i (cf. **Fig. 4.18**).

SEM was used in order to confirm the occurrence of the martensite phase in the 70% PF material. The samples for SEM were prepared following the procedure proposed by Girault et al., therewith distinguishing martensite from retained austenite in the SEM micrograph is possible [Gir98]. Representative SEM micrographs are shown in **Fig. 4.20**.

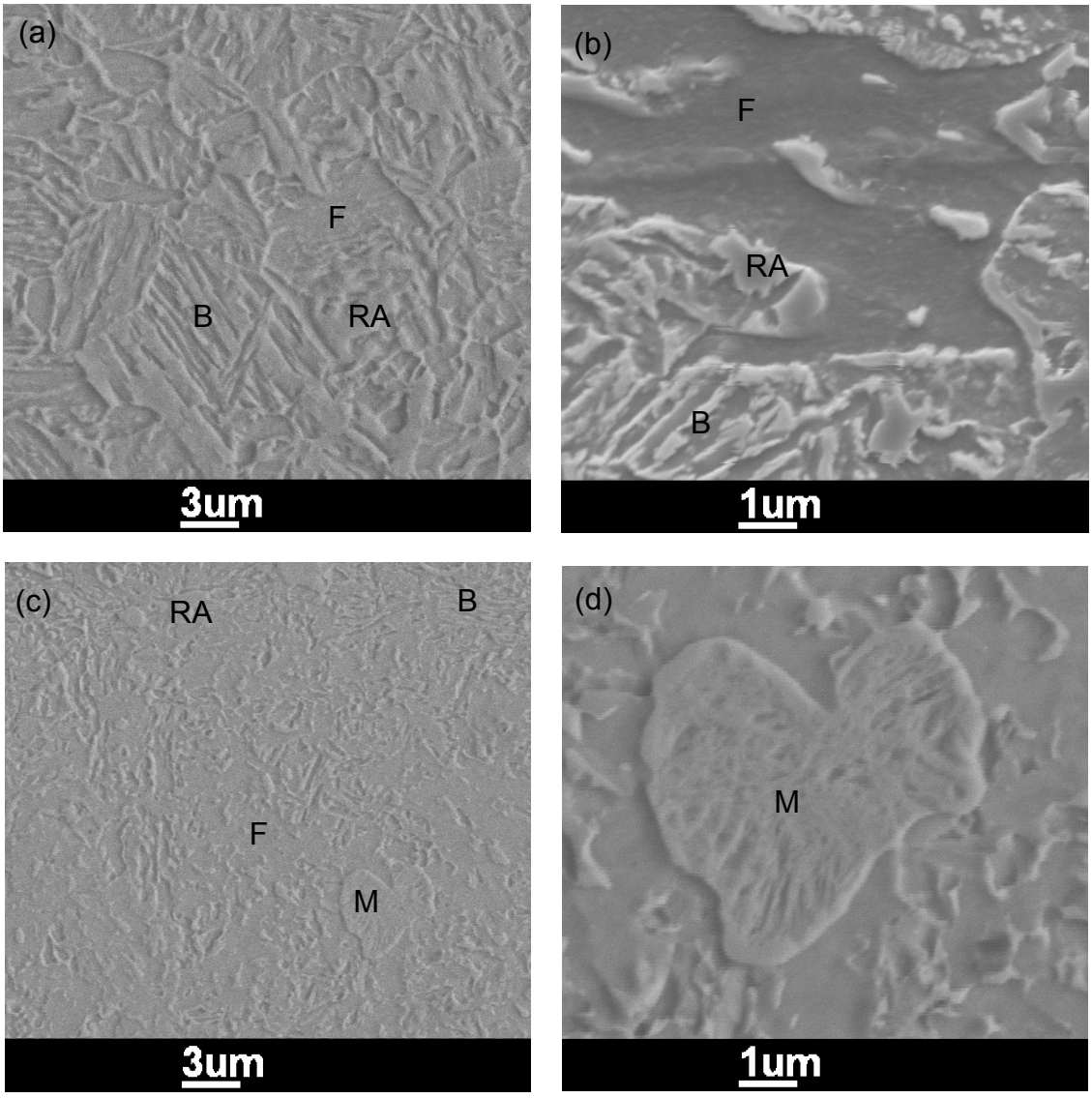

Fig. 4.20 SEM micrograph of steel A1 intercritically annealed at (a) 800, (b) 768°C and (c) and (d) 742°C. F: ferrite, B: bainite, RA: retained austenite and M: martensite.

For the material annealed to 70% PF, martensite phase was observed as can be seen in **Fig. 4.20** (c) and (d). The martensite grain is characterised by its well delineated substructure while the retained austenite looks rather smooth.

On the other hand, increasing the aluminium content leads to lower V_γ (**Fig. 4.17**). The ability of alloy A2 to proceed to higher carbon enrichment of austenite during bainitic holding (**Fig. 4.19**) results consequently in lowering the V_γ as has been discussed above. Hence, increasing the aluminium content not only reduces the cementite stability but also motivates the enrichment of austenite with carbon and leads to a lower retained austenite volume fraction but with higher carbon content and higher stability.

Additionally, dilatometric experiments were performed in order to compare the transformation behaviour at different isothermal holding temperatures. Before that comparison, the observed dilatation should be first normalised. That is because the dilatation measured, as a result of austenite transformation, during the isothermal holding depends on the isothermal holding temperature (cf. **Fig. 2.14**). The measured dilatation is related to the bainitic temperature by applying the following procedure: After complete austenitisation of the material, the ΔL-T curves of the austenite and ferrite were fitted and extended to lower and higher temperatures, respectively. The distance between these two lines ($\Delta_{\gamma\alpha}$) was then determined for each bainitic temperature investigated. The measured dilatation during isothermal holding was normalised by dividing its value to the corresponding $\Delta_{\gamma\alpha}$ (norm. $\Delta L = \Delta L/\Delta_{\gamma\alpha}$) [Tra02a, Ohl03].

The dependence of the “norm. ΔL” on the isothermal transformation time for alloys A1 intercritically annealed at 768°C and A2 intercritically annealed at 810°C is shown in **Fig. 4.21**. Considering the same amount of PF, decreasing the over-aging temperature has led to an increase in the total amount of formed bainite. This result confirms the (V_γ) results that is, if the amount of PF is constant, any increase in the total amount of bainite will be on the expense of the retained austenite amount. On the other hand, decreasing the transformation temperature decreases the transformation rate. This feature is associated with performing the isothermally bainite transformation below the nose of the TTT diagram. This is because at lower temperature the diffusion of atoms becomes more difficult [Bha01].

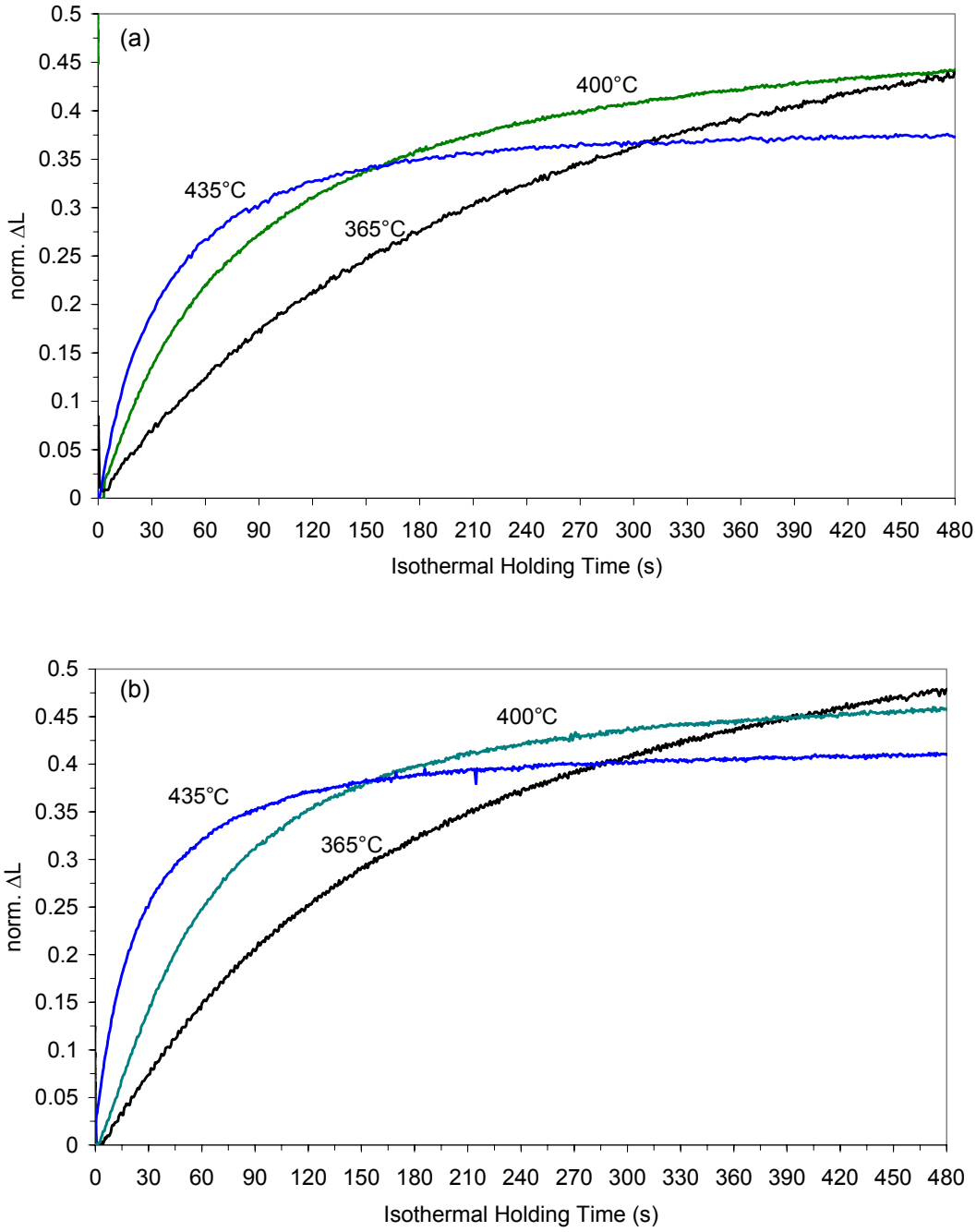

Fig. 4.21 Influence of the isothermal holding temperature on the bainitic-transformation behaviour of alloys A1 and A2 intercritically annealed at 768°C and 810°C, respectively.

4.5.3 Effect of Hot-rolling Conditions

As explained in section 4.3.2, the different hot-rolling schedules (**Fig. 4.3)** resulted in pronounced differences in the hot-rolled structure-size (**Fig. 4.5** and **Fig. 4.6**). Due to the latter variation different final TRIP-aided steel structure size is observed (cf. **Fig. 4.22**). **Tab. 4.3** gives a comparison among the final structure grain sizes of ferrite and retained austenite. Making use of the

beneficial effect of the hot rolling below T_{nRX}, a pronounced finer cold-rolled TRIP-aided steel structure was produced. Recalling the current result (as well as pervious report [Shi06]) that the employed heat-treatment parameters have no significant effect on ferrite and retained austenite grain size (cf. **Fig. 4.16**). An inference is that, in the current study, the structure fineness is dependant only on the hot-rolling conditions.

On the other hand, the observed effect of the prior hot-rolling schedule on the V_γ was very limited.

Tab. 4.3 Effect of the hot-rolling schedule on the final grain sizes of the ferrite and retained austenite phase (μm).

Phase \ Schedule	R	RP	P
Ferrite	5.0	3.5	2.3
Retained austenite	1.6	0.9	0.84

Additionally, dilatometric investigations showed that the difference in the hot rolling-schedules influences the bainite transformation kinetics in a pronounced way. **Fig. 4.23** presents the evolution of $\Delta L/L_0$ as a function of the transformation time for the different hot-rolling schedules applied on alloy A2. In **Fig 4.23** it can be seen that for smaller grains the transformation starts faster but proceeds at a slower rate. Indeed, the reduction of the grain size brings about an increase of the grain boundary area at which the first bainitic ferrite sub-units nucleate. Thus, the transformation starts faster due to an enhanced nucleation rate. The transformation then proceeds by nucleation and grow of new sub-units from the tip of the previous ones towards the interior of the austenite grain, thus when the austenite grain size is reduced the transformation proceeds in slower rate [Mat04, Jac04]. The influence of austenite grain size on the transformation rate was already shown and modelled by Rees and Bhadeshia [Ree92].

An inference is that beside the effect of chemical compositions on the bainite transformation kinetics (cf. **Fig. 4.14**); another feature highlights the transformation occurring in the cold rolled TRIP-aided steels: the prior hot-rolling schedule.

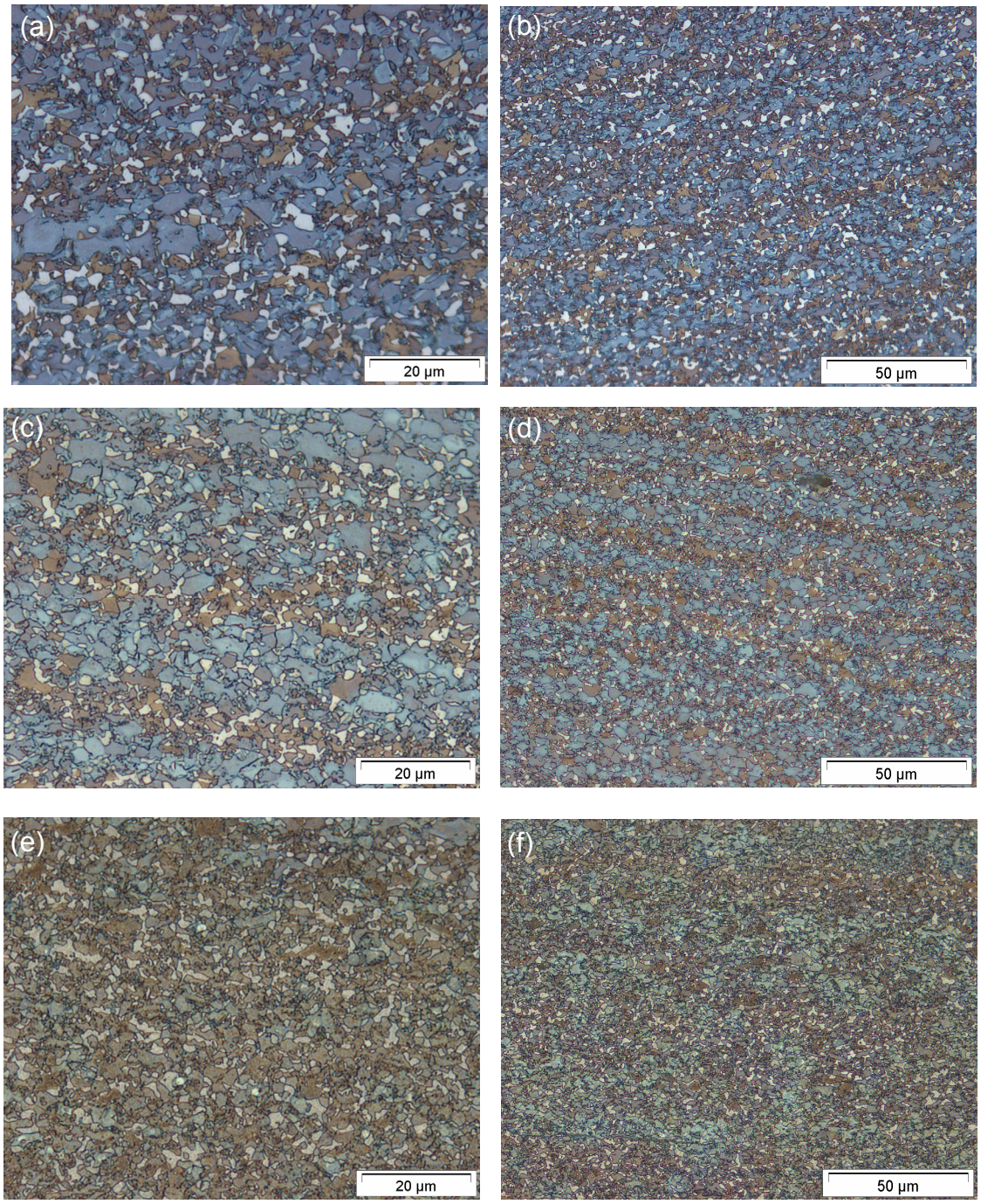

Fig. 4.22 Different TRIP steel microstructures obtained as a result of using different hot rolling schedules (a) and (b) schedule R - (c) and (d) schedule RP - (e) and (f) schedule P. Microstructures are for steel A2 intercritically annealed for 70%PF.

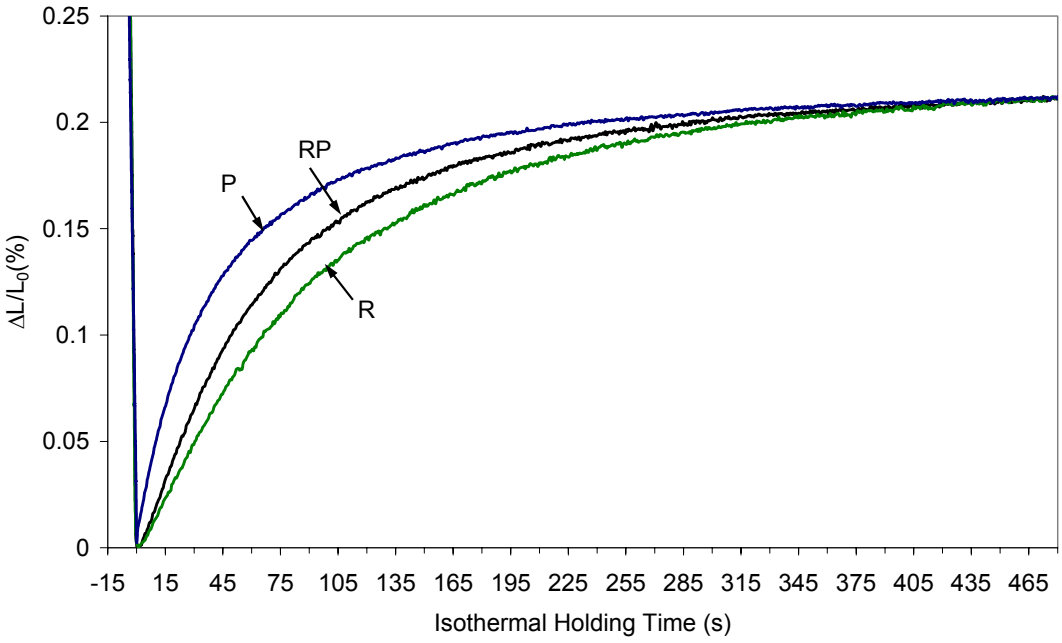

Fig. 4.23 Dilatation curves of alloy A2 intercritically annealed at 810°C and bainitic transformation at 400°C.

On the other hand, instead of the difference in the transformation rates, the bainite-reaction proceeds to the same final amount of bainite (cf. **Fig 4.23**). Accordingly, by mass-balance relationship among the material phases, V_γ in the final microstructure should be unaffected by the prior structure-fineness. This dilatometric-observation is in consistence with that the measured-V_γ is insignificantly affected by the hot-rolling schedule.

4.6 Mechanical Properties

The tensile properties of steels A1 and A2 were investigated using standard tensile specimens according to ASTM, subsize E8-03, with width and gauge length of 6.4 and 25.4 mm, respectively. The samples were machined with their tensile axis oriented perpendicular to the rolling direction. The samples were subjected to the heat-treatment described in section 4.5.

Figs. 4.24 and **4.25** show the effect of the processing route on the ultimate tensile strength (R_m), yield strength (R_e) and the total elongation % (TEl%) for steels A1 and A2, respectively. The R_e-values plotted in the histograms are the lower yield strengths or the $R_{p0.2}$-values, in case of the absence of a yield point (continuous yielding behaviour). Representative tensile stress–strain curves showing the continuous and discontinuous yielding behaviour is shown in **Fig.**

4.26. In **Fig. 4.27** the TEl% values are plotted *vs* the R_m values for all combinations of the rolling conditions and heat-treatment parameters.

It can be concluded from **Fig. 4.24, Fig. 4.25 and Fig. 4.27** that PF% (intercritical annealing condition) has the most pronounced effect on the mechanical properties for both steels. The R_m values increase with decreasing the PF content. This can be explained by the higher austenite content formed during the intercritical annealing. A higher amount of γ_i results in a higher amount of high strength bainite after the isothermal bainitic transformation step.

On the other hand, increasing the PF% from 30% to 50% results in increasing the TEl% values. In addition to the effect of increasing the soft PF-content on the TEl%, the expected higher amount of retained austenite surrounded by the bainite phase in the 30%PF microstructure can also contribute to the observed lower TEl%. That is because the film shape retained austenite grains located at the bainite are not transformed to martensite even when considerable amount of deformation is applied, thus not contributing to the ductility improvement [Kim01].

Further increase in the PF% to 70% has no further enhancement effect on the TEl%. This observation can be justified by the retained austenite characteristics associated with the 70%PF material. Principally, the total elongation of TRIP-aided steel is controlled by the volume fraction and stability of the retained austenite and the difference in strength between matrix and second phase [Sug06]. In the 70% PF material the V_γ is obviously lower than that of the 50% PF material (cf. **Fig. 4.17**) and with lower stability as discussed before.

Furthermore, Timokhina et al. have reported that the polygonal ferrite in the C-Mn-Si-Nb-steel showed a lower ferrite deformation than in the non-Nb steels and did not flow around the bainitic region during straining. This has been justified by the fact that the Nb addition has the effect of promoting precipitation hardening of the ferrite and/or through grain refinement, which leads to the strengthening of ferrite [Tim04].

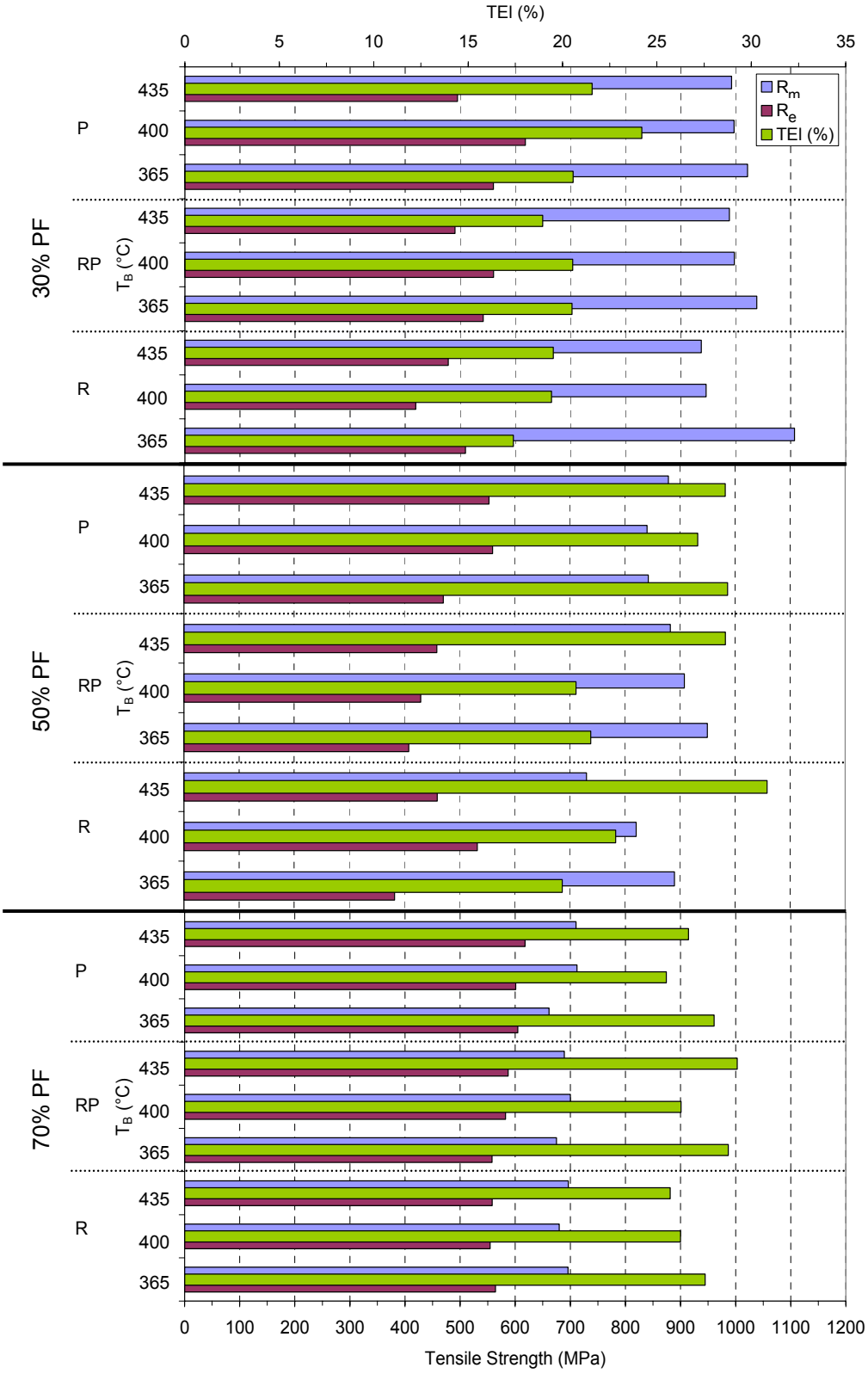

Fig. 4.24 Tensile strength (R_m), yield strength (R_e) and total elongation % (TEI (%)) dependence on the hot-rolling and annealing conditions for alloy A1.

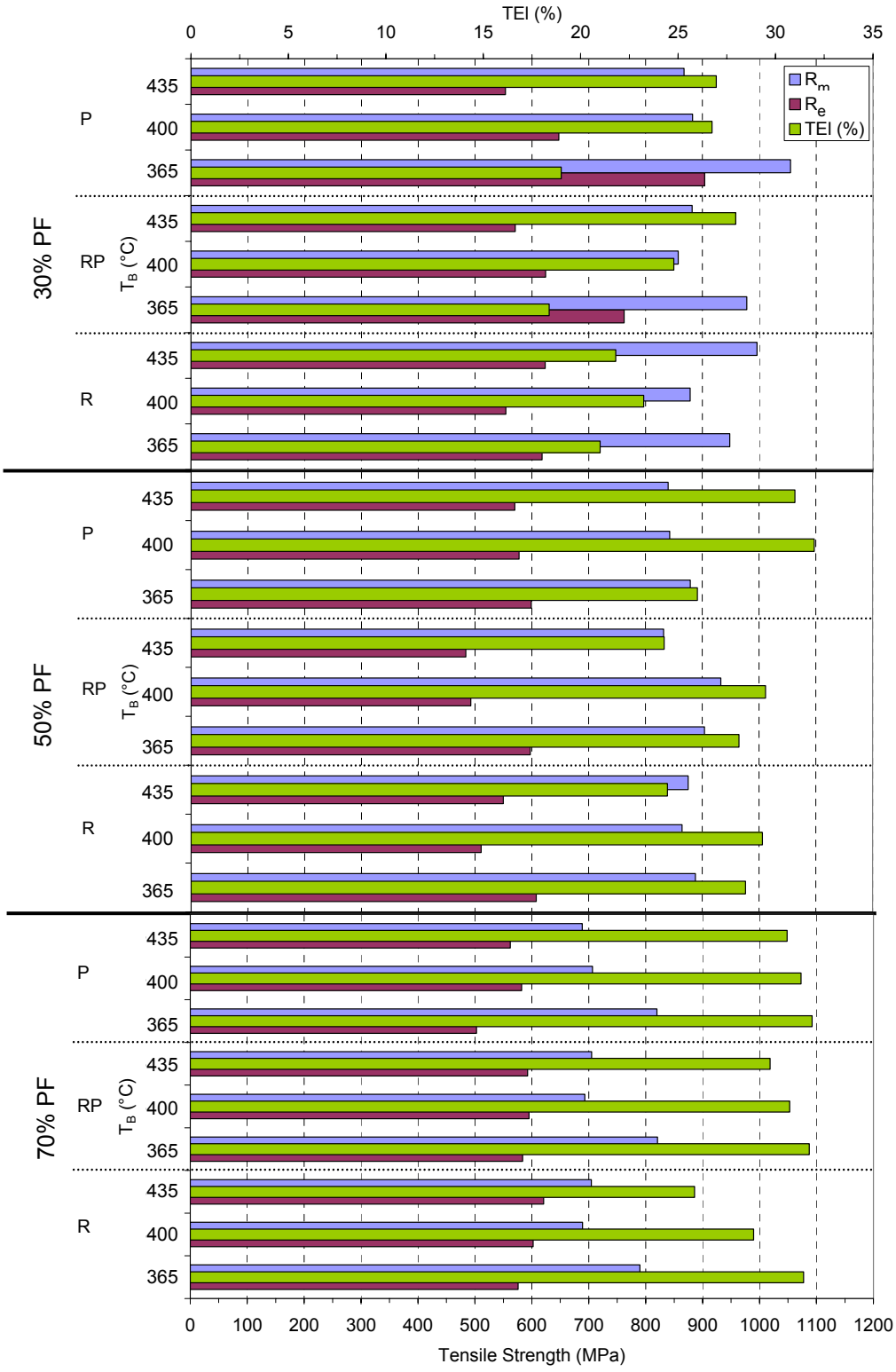

Fig. 4.25 Tensile strength (Rm), yield strength (Re) and total elongation % (TEl (%)) dependence on the hot-rolling and annealing conditions for alloy A2.

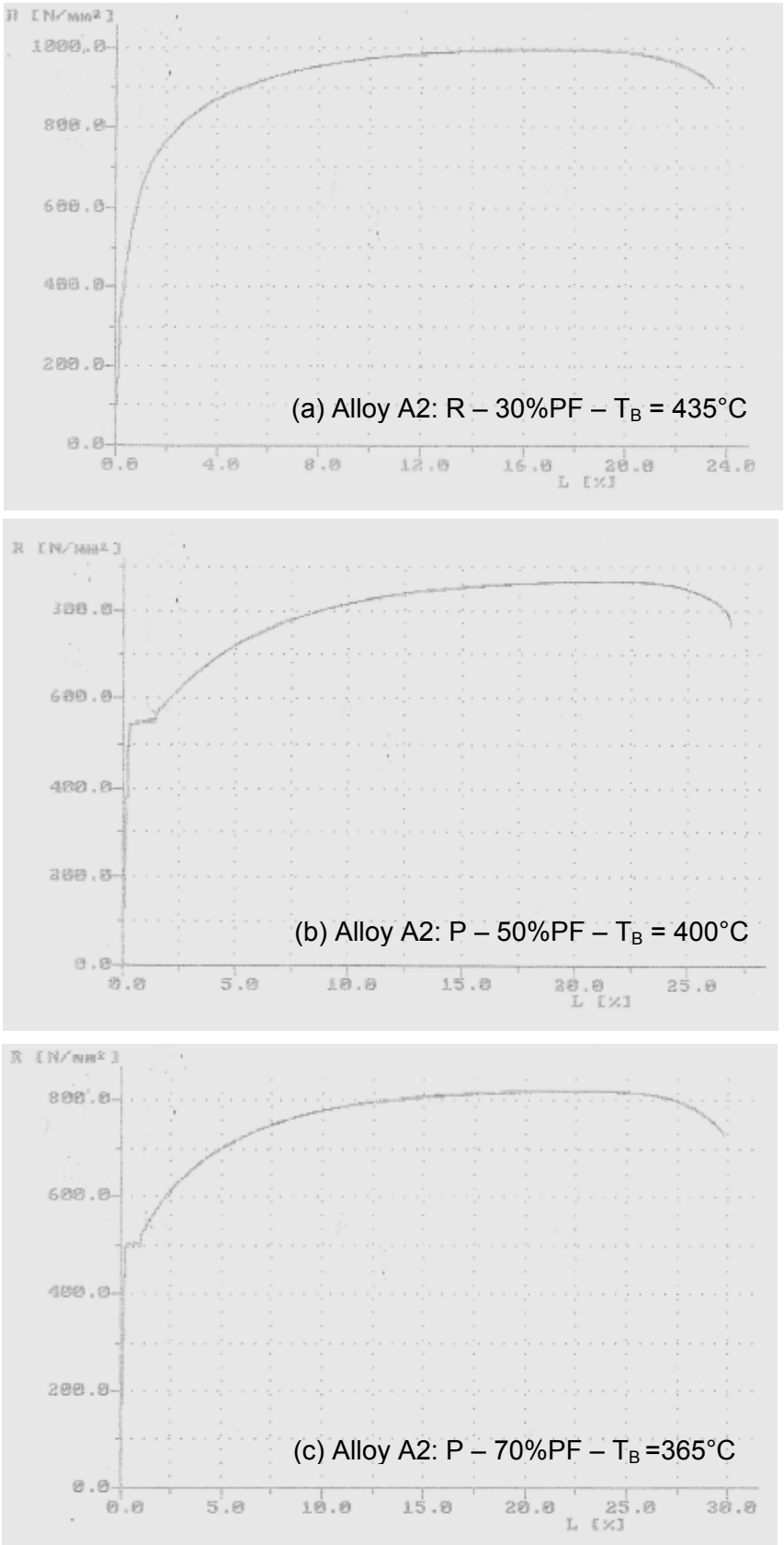

Fig. 4.26 Representative tensile stress–strain curves showing (a) continuous yielding and “(b) and (c)” discontinuous yielding behaviours.

On the other hand, the materials annealed to 70% PF have recorded high R_e values compared with their R_m values. For this case, the retained austenite stability is very low, as explained before. Consequently, transformation in such low austenite stability would take place even in the elastic region [Ohl02]. Thus, the TRIP effect is most likely to take place in the elastic region and would eventually increase the R_e values, but subsequent transformation in the plastic region would be limited. Consequently the contribution of the TRIP effect in enhancing the R_m and the TEl% is also limited.

Referring to **Figs. 4.24** and **4.25** the mechanical properties do not vary similarly with respect to the isothermal bainitic holding temperature, T_B. The complex nature of the microstructures and the interaction among their phases result in an unpredictable effect of the T_B especially in the investigated relatively narrow range (365°C-435°C).

Since TRIP-aided steels combine high strength and high ductility, their mechanical properties are often characterized by the product of the tensile strength and the total elongation ($R_m \times$ TEl (%)) which is known as the formability index [Bar02].

At each combination of PF-content and hot-rolling condition the average formability index has been calculated from the values recorded at the three corresponding T_B temperatures. A comparison among these averages is shown in the histogram of **Fig. 4.28**. It is clear form this figure that the highest formability index is recorded for the steels annealed to 50% PF this result is in association with the strength-ductility balance recorded at this PF content (**Fig. 4.27**).

On the other hand, it can be concluded from **Fig. 4.28** that the hot-rolling schedule has a pronounced effect on the formability index for both steels. Interestingly, the hot rolling schedule has a very limited effect on the V_γ values. Thus, the improvement in properties seems entirely to be due to microstructural refinement (**Fig. 4.22**). In addition to the well known effect of grain refinement on the improvement of the mechanical properties, the higher stability of the smaller retained austenite grains has a further improving effect. Brandt et al. [Bra93] have pointed out that smaller retained austenite particles contain less potential nucleation sites for the transformation to martensite and consequently require a larger total driving force for nucleation of martensite. Thus, by controlling the

deformation temperature and the degree of deformation below T_{nRX} during the hot-rolling process, it was possible to improve the strength-ductility balance of the cooled-rolled TRIP-aided steel. The deformation below the T_{nRX} results in distinct refinement of the final TRIP-aided steel microstructure.

A poorer formability index for the lower Al-content alloy (A1) in spite of its higher austenite-content is related to lower carbon enrichment during isothermal bainite transformation (cf. **Fig. 4.19**). This results in a lower stability of the austenite, which is then transformed to martensite in an earlier stage of plastic deformation. In some cases, where the austenite stability is very low, the transformation takes place even in the elastic region so that the dual phase behaviour can be observed. Nevertheless, a minimum amount of retained austenite should be present in order to guarantee TRIP behaviour and enhanced strength and formability [Ble04].

For further analysis, the average mechanical properties of A1 and A2 alloys had been calculated from all the values recorded under the different employed processing routes. The calculated values are listed in **Tab. 4.4**. The values are highly reliable because they were obtained from many samples processed under different conditions, but these conditions are quite similar for the two alloys. It can be concluded that increasing the aluminium content has improved the formability of the steel A2 through improving its ductility.

Tab. 4.4 The average mechanical properties of A1 and A2 alloys calculated from all the values recorded under the different employed processing routes.

Alloy	R_m (MPa)	R_e (MPa)	TEl(%)	F.I. (MPa%)
A1	851	524	24	20280
A2	845	595	27	22758

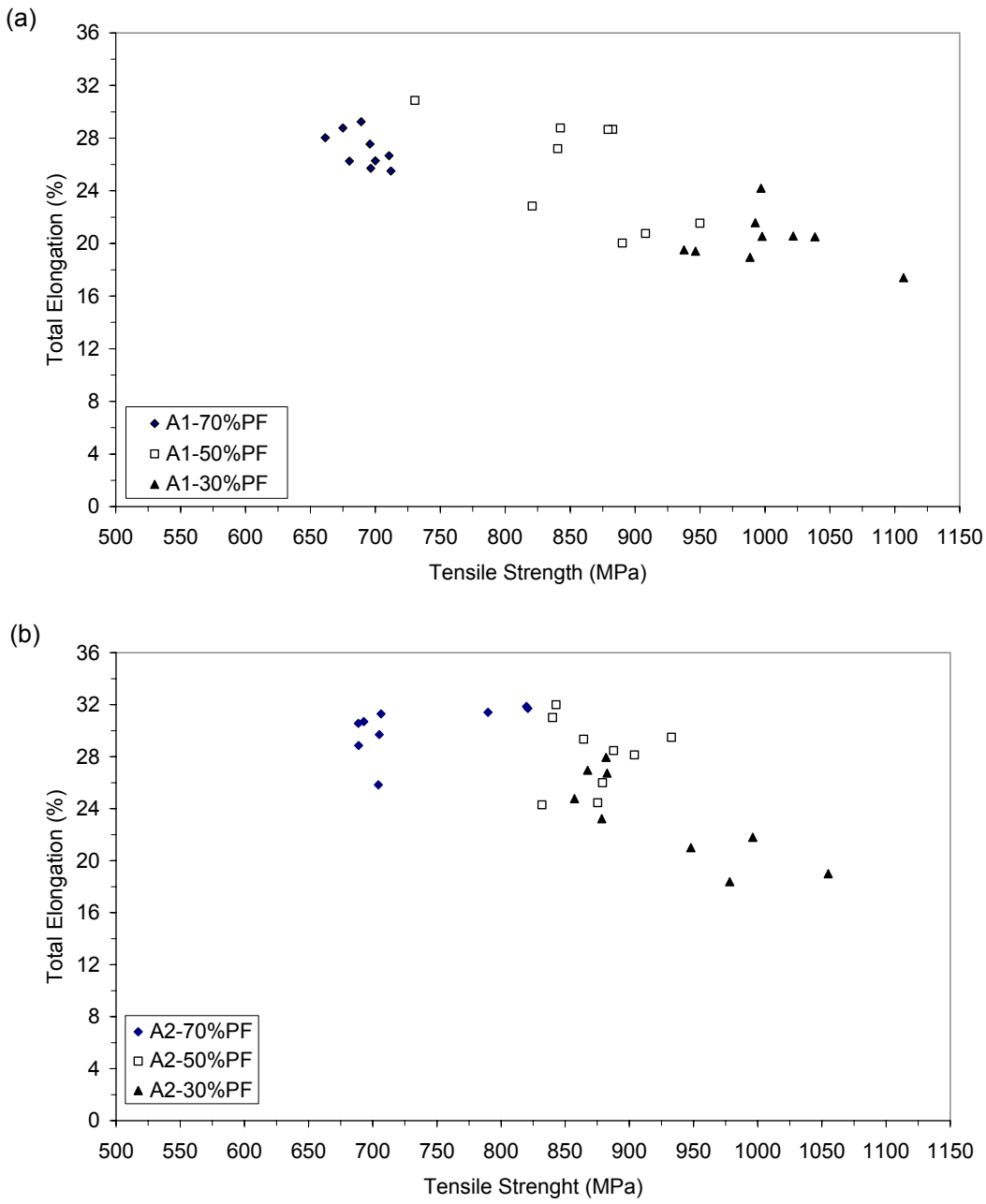

Fig. 4.27 Map of the tensile strength *vs*. total elongation (%) for all combinations of the investigated processing routes for (a) alloy A1 and (b) alloy A2.

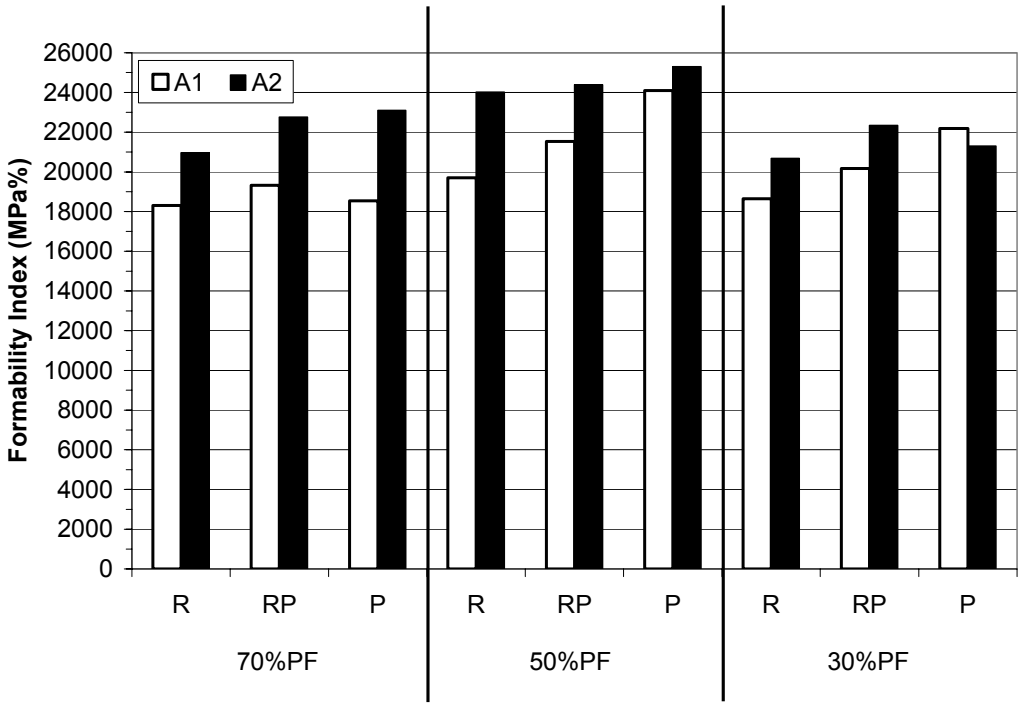

Fig. 4.28 The average formability index at each combination of PF-content and hot-rolling condition; calculated from the values recorded at the three corresponding T_B temperatures.

4.7 Conclusions

This chapter provided an investigation of the microstructure formation and mechanical properties obtained after different hot-rolling and two-step annealing treatment conditions of two Mn-Si-Al cold-rolled TRIP-aided steels alloyed with Mo-Nb. From the present investigation the following conclusions can be drawn:

1- By making use of the beneficial effect of the hot-rolling below T_{nRX}, a pronounced finer cold-rolled TRIP-aided steel structure had been produced. This resulted in improving the strength-ductility balance of the steel.

2- Comparison between the transformation kinetics using the thermodynamic calculations and the dilatometric method is only relevant when using a heating rate where the transformation temperatures are independent of the heating rate. Using higher heating rate is then misleading.

3- The intercritical annealing temperature has no significant effect on the grain size of ferrite and retained austenite.

4- As long as the bainite transformation in TRIP steel can comply with the T_0 curve, the retained austenite content would increase with increasing the bainite transformation temperature.

5- It is the composition of the intercritical austenite which controls its behaviour during the transformation-process and not the bulk composition of the alloy. During the current study, it is proposed that the martensite formation was observed due to the partitioning of elements during the intercritical annealing in such a way that at low intercritical temperature the γ_i is enriched with the carbide former elements (C, Mn) whereas the carbide suppression element (Al) is at lower level.

6-Increasing the aluminium content not only reduces the cementite stability but also:

(a) Motivates the formation of bainitic-ferrite and leads to a higher fraction of bainite.

(b) Lowers the fraction of retained austenite.

(c) Increases the carbon content in retained austenite and improves its stability.

(d) The latter effect would enhance the formability though increasing the ductility.

7-For the given alloying elements, the most promising microstructures with respect to the strength-ductility balance are those containing 50% PF.

Chapter 5
Ultra-fine Bainite: Results and Discussion

5.1 Introduction

In silicon-alloyed steels the martensite start temperature "M_S" of carbon-enriched austenite may, after a certain transformation time, decrease to the level where the martensite formation during cooling from the transformation temperature is avoided [Del65]. Using this feature in combination with high carbon content and low bainitic transformation temperature ultra-high strength bainitic steels had been developed [Cab02, Gar03a, Gar03b, Cab04, Gar05].

The high strength of these steels is due to their very fine structure. The observed refinement is a consequence mainly of the ability of high carbon content and low transformation temperature to enhance the strength of the austenite. It is expected that the bainite-plates would become thinner as the yield strength of the austenite, from which they are formed, increases [Bah01, Sin98]. Thus, the high carbon directly refines the structure by strengthening the austenite and indirectly by lowering the M_S temperature and thus allowing performing the bainitic transformation process at lower temperature.

However, the high carbon content results in the existence of large regions of untransformed austenite in the microstructure, which is known to be detrimental to the mechanical properties. The incomplete transformation phenomenon, which limits the amount of bainite that can be formed at any temperature, is the reason for the existence of these large regions of untransformed austenite [Bha01, Aar06].

5.1.1 Aim of the Study

This chapter is concerned with a further development of the ultra-fine bainitic steel by decreasing its carbon content aiming at both, lowering the retained austenite and accelerating the bainite transformation reaction. The consequence of lowering the carbon content below the eutectoid composition provides the possibility of intercritical annealing of the alloy which results in a wider window for designing mechanical properties.

A systematic method consisting of three steps was developed. In the first step the appropriate heat-treatment parameters using the dilatometric measurements

were employed. In the second step the obtained parameters were reapplied using salt-bath treatment and in the third one the final structure was characterised. Throughout the present work, the reliability of different thermodynamic and kinetic models-based on phase transformation-had been reviewed.

5.2 Investigated Material

Two steel alloys with different carbon contents had been produced by induction melting in vacuum. A water-cooled suction-mould had been used for the production of cylindrical samples with the dimension of ϕ33 mm $\times$ 140 mm from the melt. The samples were cooled down to the ambient temperature and then hot pressed to a thickness of 12 mm. The material was homogenised in a protection atmosphere for 48 h at 1200°C, then slowly cooled down to RT inside the furnace simply by switching off the power. It took about 12 h to cool down the samples to 300°C. The chemical compositions of the materials (alloys B1 and B2) are shown in **Tab. 3.1**. Manganese and chromium had been added for hardenability, molybdenum to prevent temper embrittlement due to phosphorus and silicon to prevent the precipitation of cementite during bainite formation. Aluminium and cobalt had been added to accelerate the bainite transformation process.

5.3 Dilatometry and Heat-Treatment

Dilatometric investigations were conducted using samples with 5 mm diameter and 10 mm length prepared from the homogenised material. The dilatometric results had been used for the selection of the appropriate heat-treatment parameters of the two alloys as will be described later. Using salt baths mentioned in section 3.2, the designed heat-treatment had been repeated on further mechanical testing samples and on samples for micro-constituents investigations.

5.3.1 Defining the Intercritical Region

In order to define the intercritical region, dilatometric measurements had been applied by heating specimens up to 1100°C. For better tracing the equilibrium points, a heating rate of 0.05K/s had been used. The variation of the relative

change in length as a function of temperature had been measured from which the transformed austenite fractions was calculated employing the lever rule. The results for both steels are shown in **Fig. 5.1a**. **Fig. 5.1b** compares the measured transformed-fraction and the predicted one obtained using the Thermo-Calc TCW3 software employing the TCFE3 database.

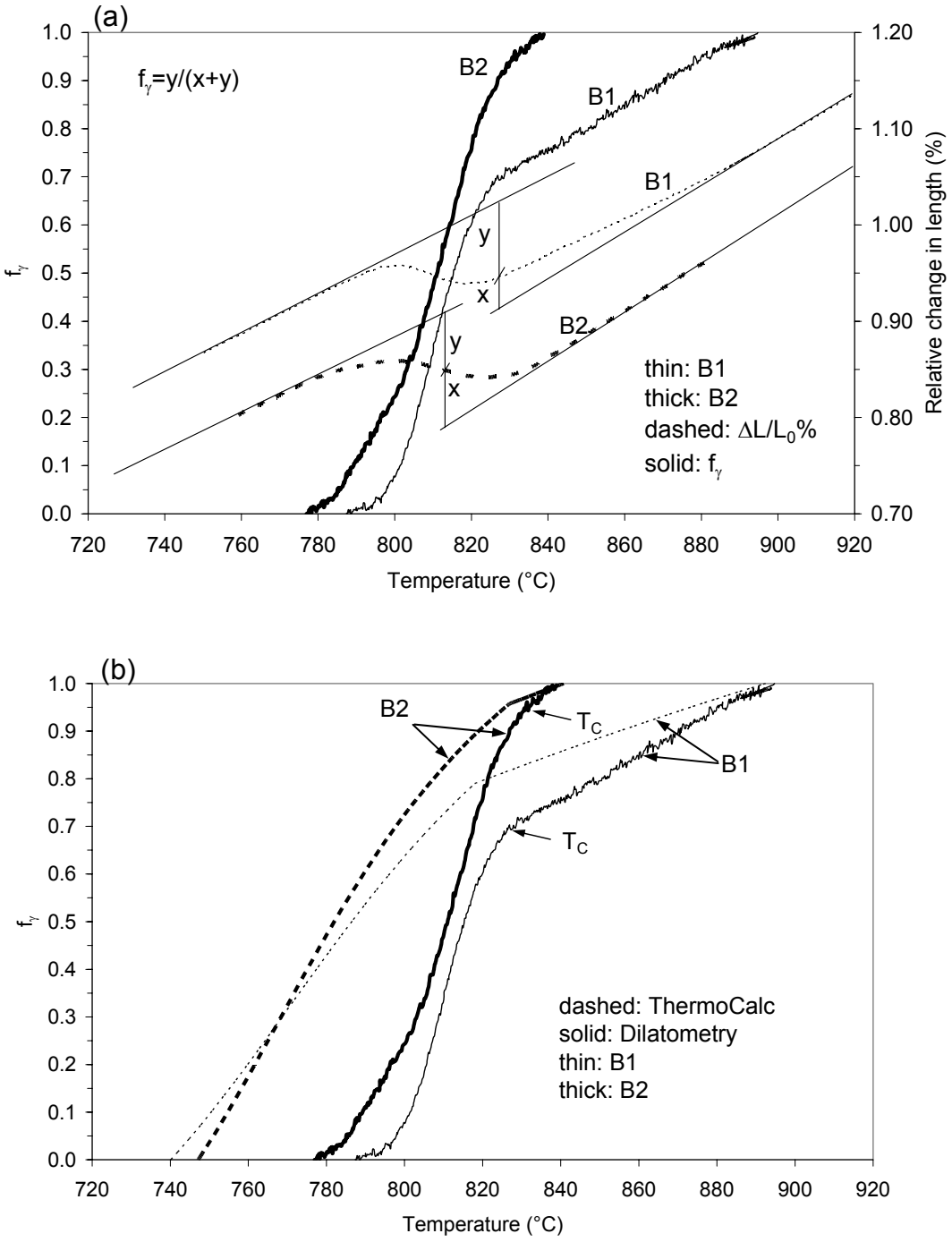

Fig. 5.1 (a) Dilatation versus temperature curves observed during continuous heating together with the calculated formed austenite fraction (f_γ) and (b) Comparison of the calculated (f_γ) and the predicted one using Thermo-Calc.

As mentioned in chapter 4, the austenite starts to form in the carbides rich areas. Once the carbides regions disappeared (corresponding to the point T_C in **Fig. 5.1b**), the austenite formation continues at much slower rate.

Tab. 5.1 compares the measured and the predicted critical temperatures. The reason for the significantly higher measured A_{e1} temperature in comparison with the calculated one is the sluggish kinetics of austenite formation close to A_{e1}. Similar results had been reported in ref. [Dem02], too.

Tab. 5.1 Predicted versus measured critical temperatures.

Alloy		A_{e1} (°C)	T_C (°C)	A_{e3} (°C)
B1	Predicted	740.1	818.0	892.5
	Measured	787.4	826.9	894.7
B2	Predicted	747.2	829.9	840.8
	Measured	777.3	831.4	838.9

In order to confirm the dilatometric results, a microstructure study had been performed on steel B1. The microstructures obtained for samples quenched from 870, 850, 830 and 815°C down to RT are shown in **Figs. 5.2a-d**. For better distinguishing of the pearlite phase in the martensite matrix, LePera etchant had been used. **Tab. 5.2** compares the different non-transformed-phase constituents, i.e. ferrite or ferrite+pearlite obtained by microstructural investigations, Thermo-Calc and dilatometry. The present results are in consistence with previous reports showing that the lever rule gives a higher ferrite amount than that one obtained by the more reliable microstructure examinations especially for lower temperatures. This difference is correlated with the fact that the lever rule does not take into account the redistribution of carbon between ferrite and austenite and that the formation of pearlite has a distinctly different volume effect on the formation of ferrite [Gom03, Kop01].

Tab. 5.2 Percentage of ferrite-ferrite+pearlite obtained using different methods.

Temp. (°C) / Method	870	850	830	815
Microstructure	8.1	17.2	23.4	30.1
Thermo-Calc	5.82	11.4	17.2	23.2
Dilatometric	10.5	20.4	28.2	50.4

Referring to **Fig. 5.2**, the only microstructure with pearlite structure (dark-brown stained) is that one obtained by quenching from 815°C, whereas for those quenched from higher temperatures the pearlite structure is absent. These results are consistent with the assumption that the change in the slope of the transformation-temperature diagram corresponds to the T_C temperature (see **Tab. 5.2**).

Locating the T_C temperature is of particular importance for the design of the heat treatment process, namely, the intercritical annealing stage. Determination of the temperature range of pearlite dissolution process allows the selection of the most suitable intercritical temperature for obtaining microstructures which gives optimum combination of mechanical properties. During the current investigation it was important to show that the annealing temperature used in the experiments is higher than the austenite+ferrite-pearlite temperature range.

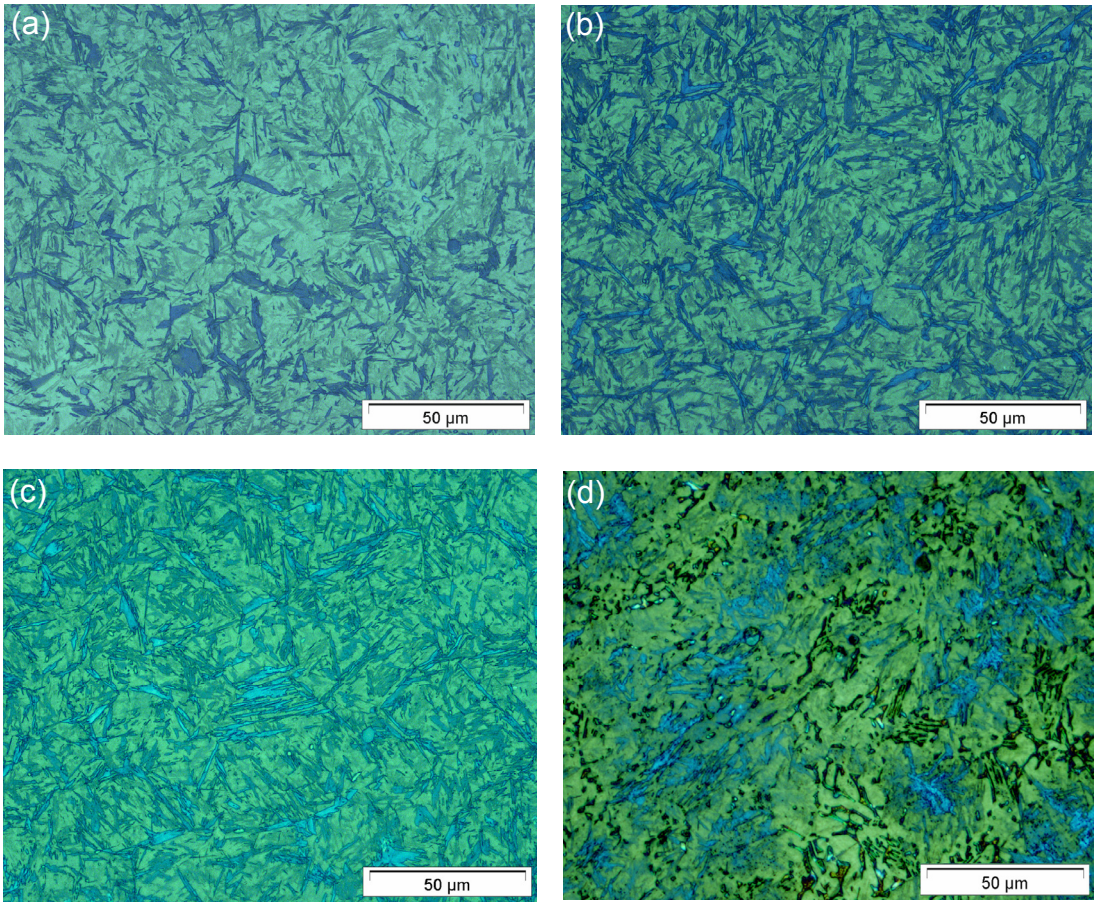

Fig. 5.2 Microstructure observed after quenching from (a) 870°C, (b) 850°C, (c) 830°C and (d) 815°C. ferrite: blue, pearlite: dark-brown in the martensite matrix

5.3.2 The Martensite Start Temperature

In order to locate the martensite start temperatures, the dilatometer was used to quench both alloys B1 and B2 from different temperatures with a cooling rate of 10K/s. The dilatation curves during quenching are shown in **Fig. 5.3**, where the decrease of the M_S temperature with decreasing intercritical annealing temperature is observed and can be explained by the austenite enrichment with carbon during the intercritical annealing together with the refinement of their particles.

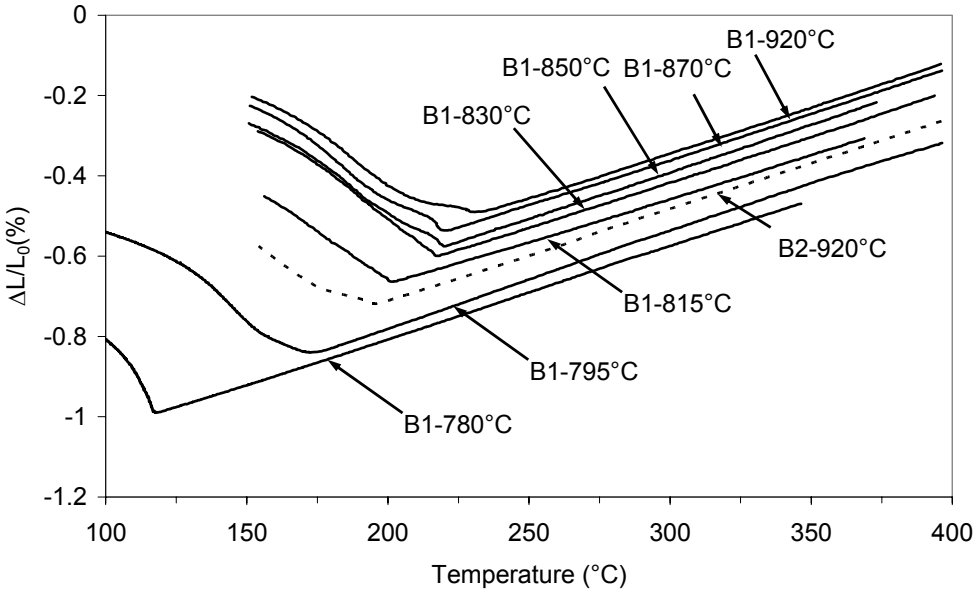

Fig. 5.3 Dilatation versus temperature curves observed during continuous cooling from the annealing temperatures for alloys B1 and B2.

In **Fig. 5.4** the M_S temperatures are plotted against the annealing temperature. The change in the slop of the line fitting the date-points is due to the change in the mechanism of austenite formation. As described by De Meyer et al., the austenite first nucleates and grows at the pearlite colonies. The second austenite formation mechanism starts to take place once the cementite rich regions disappeared (T_C temperature). This takes place by growing of austenite into ferrite and redistribution of carbon between the former and the latter, simultaneously [Dem02].

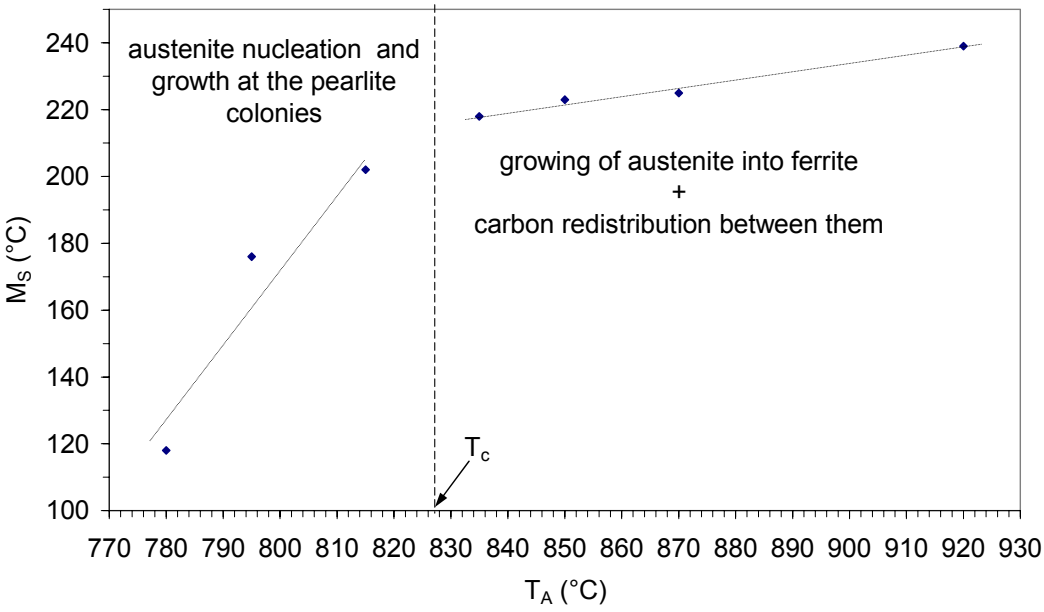

Fig. 5.4 Dependence of the martensite-start temperature on the annealing temperature for alloy B1.

5.3.3 Selection of the Heat-treatment Parameters

According to the investigations of the intercritical transformation and the M_S temperatures of the two alloys, the heat treatment temperatures have been selected as shown in **Tab. 5.3**. Not to be mentioned that the selected bainite transformation temperature (T_B) should be above M_S temperature and that of the autenitisation temperature (T_A) should be above T_C temperature.

Tab. 5.3 Used heat-treatment parameters (annealing temperature "T_A" and austempering temperature "T_B") together with the martensite start for each T_A.

Alloy	B1				B2
T_A (°C)	920	870	850	830	920
M_S (°C)	239	225	223	218	197
T_B (°C)	290, 250	290, 250, 230	290, 250, 230	290, 250, 230	290, 250, 230, 210

5.3.4 Bainite Transformation

The dilatometer was also used to perform the heat treatments at different T_A and T_B temperatures. The samples were heated at a rate of 10K/s up to the prescribed austenitising temperature, held there for 15 min and then cooled

down to the austempering temperature with a cooling rate of 10K/s. This cooling rate was sufficient to avoid any allotriomorphic ferrite and pearlite formation during cooling to the prescribed bainitic holding temperature. This could be detected from the linearity of the temperature-relative change in length curve, being recorded during cooling. After Similar linearity had been obtained during cooling to room temperature after the austempering process at the prescribed bainitic holding temperature. The latter linearity indicates that the autenitisation process has stabilised the retained austenite and moved the M_S temperature well below RT. So the final microstructure is free of martensite. Accordingly, the final structure consists of the prescribed ferrite amount, bainitic ferrite (α_b) and retained austenite. The later micro-constituent was quantified using x-ray diffraction method as will be described in section 5.4.3, whereas the former was quantified using LOM (**Tab 5.2**). Therefore, by mass-balance relationship among the phases, the final α_b volume fraction (V_b) can be calculated.

Representative results from the real-time monitoring of the extent of the bainite reaction are shown in **Figs. 5.5 a-c**. In these figures, the calculated V_b is settled at the end of the bainite transformation; whereas the progressive increase in α_b with transformation time is calculated assuming the linearity between $\Delta L/L_0$ and V_b (cf. **Fig. 2.14**). In these curves, it is assumed that the point where dimensions cease to change represents 100% of transformation. In all cases the samples had been quenched after reaching this point. Horizontal lines have been drawn nearby these points to aid in estimating them.

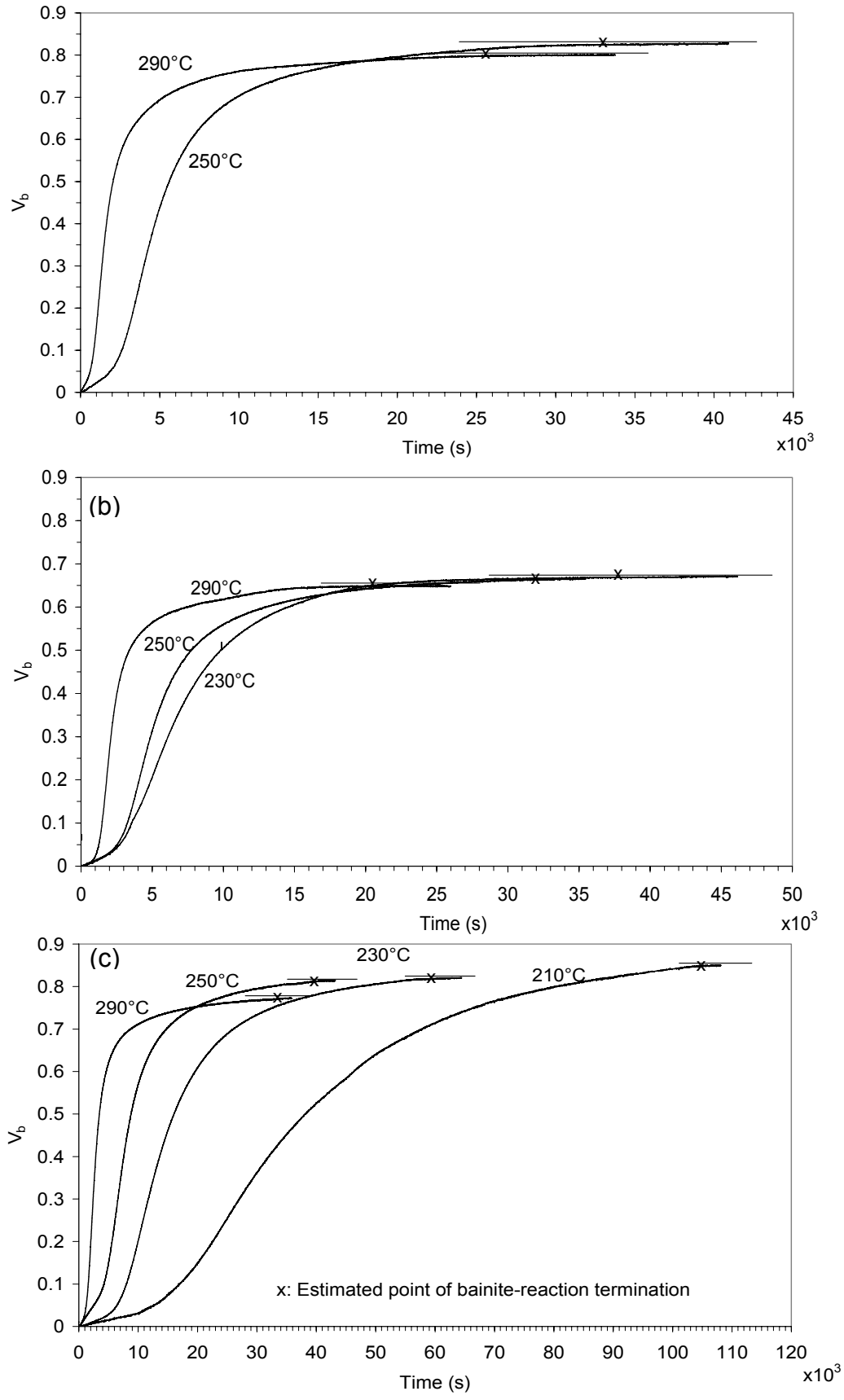

Fig 5.5 V_b versus time curves observed during isothermal holding of (a) alloy B1 quenched from 920°C (b) alloy B1 quenched from 850°C and (c) Alloy B2 quenched from 920°C.

The reason for this termination of the reaction, which limits the amount of bainite that can be obtained at any temperature, is explained by the incomplete-reaction phenomenon. The reaction is said to be incomplete since transformation stops before the phases achieve their equilibrium compositions [Bha01, Aar06]. It is clear from **Fig. 5.5** that for the transformation performed at higher temperature the bainite reaction proceeds to lower amounts of α_b in shorter time frames compared with that performed at lower temperature.

Furthermore, in **Fig. 5.6** the dependence of transformation kinetics on the annealing temperature and alloy composition is shown.

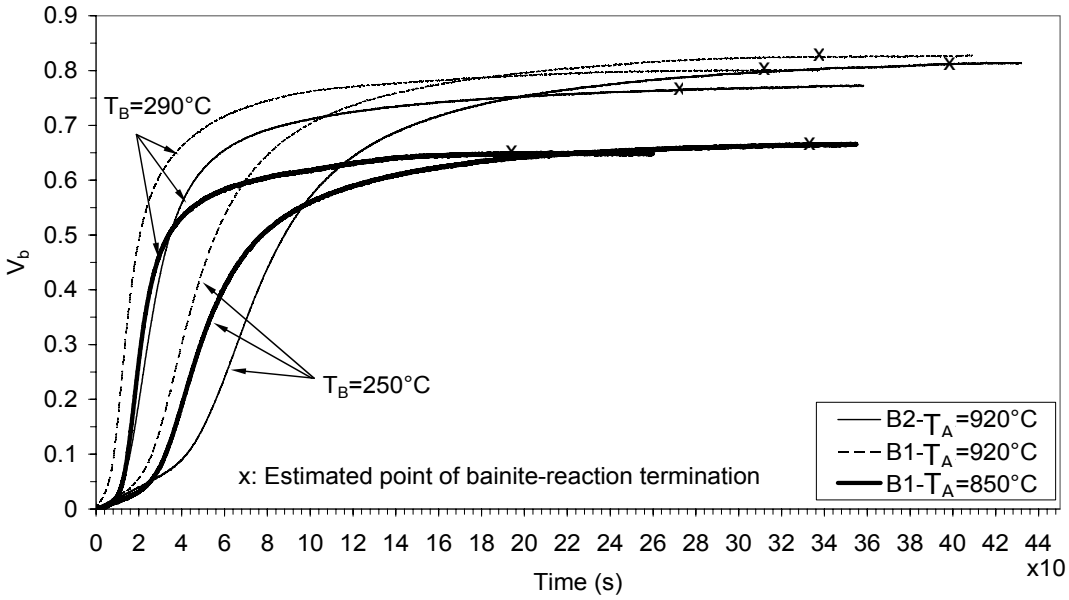

Fig. 5.6 V_b versus time curves observed during isothermal holding at T_B temperature after quenching from T_A temperature for alloys B1 and B2.

The current results demonstrate that, for the same heat treatment conditions, the alloy with lower carbon content (B1) proceeds to higher amounts of bainitic ferrite in shorter time frames compared with that of higher carbon. The holding times required for cessation of the bainite reaction for the investigated heat treatment conditions are illustrated in **Fig. 5.7**. It is important to mention here that the holding time required for termination of the bainite reaction is shorter than that reported in ref. [Gar03b, Gar05, Has06]. This is due to the lower carbon content used during the current research. Furthermore, much longer time-frames are required for alloys with higher carbon content and without

addition of the bainite-reaction accelerating elements, i.e. Al and Co [Cab02, Gar03a, Cab07].

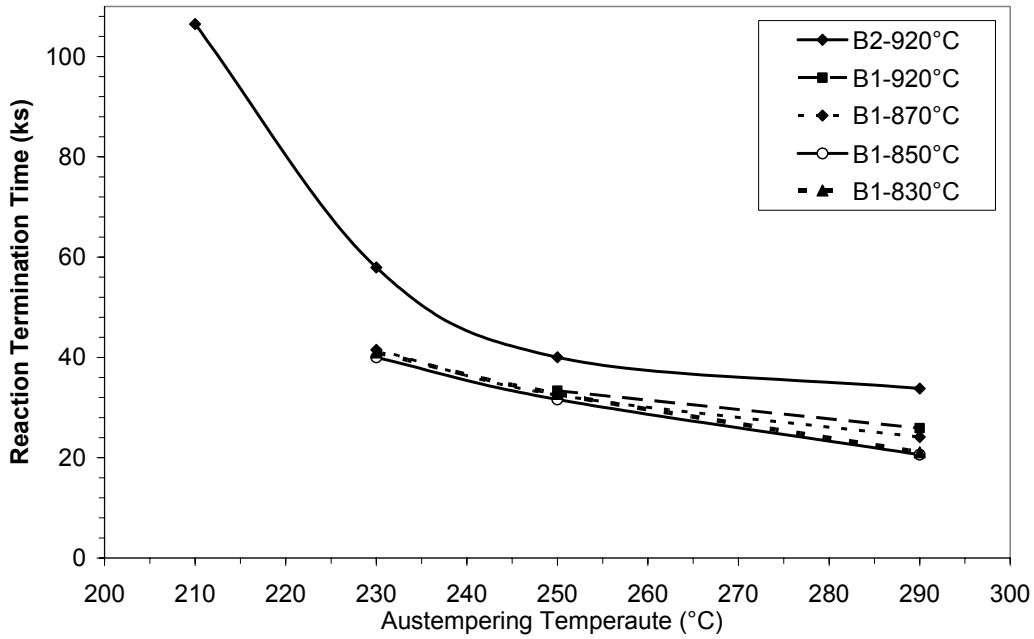

Fig. 5.7 Estimated holding time required for the cessation of the bainitic reaction for alloys B1 and B2 quenched from the prescribed annealing temperature.

The bainite transformation is therefore accelerated by both, lowering the carbon content of the alloy and the addition of the Al and Co elements. Calculations of the driving force for the transformation of austenite into ferrite ($\Delta G^{\gamma\alpha}$) for alloys B1 and B2 (cf. **Fig. 5.8**) confirm the thermal dilation results. Thus, the dilatometric results demonstrate that both rates of the bainite formation and its total amount would increase as a result of decreasing the carbon content. Of course, the reduction of the carbon content of the alloy is only as long useful as it does not lead to an unacceptable decrease in strength of the steel, i.e. by coarsening the structure.

Concerning the transformation times of alloy B1, it is to be mentioned that two contradicting factors are controlling them in the intercritical region. The formation of ferrite resulted in decreasing the total amount of bainite which consequently results in decreasing the transformation time, whereas increasing the ferrite amount results in enriching the austenite with carbon, (according to Thermo-Calc calculations: 0.420, 0.444 , 0.470 and 0.501%C at 920, 870, 850, and 830°C, respectively) the latter effect results in deceleration of the transformation process.

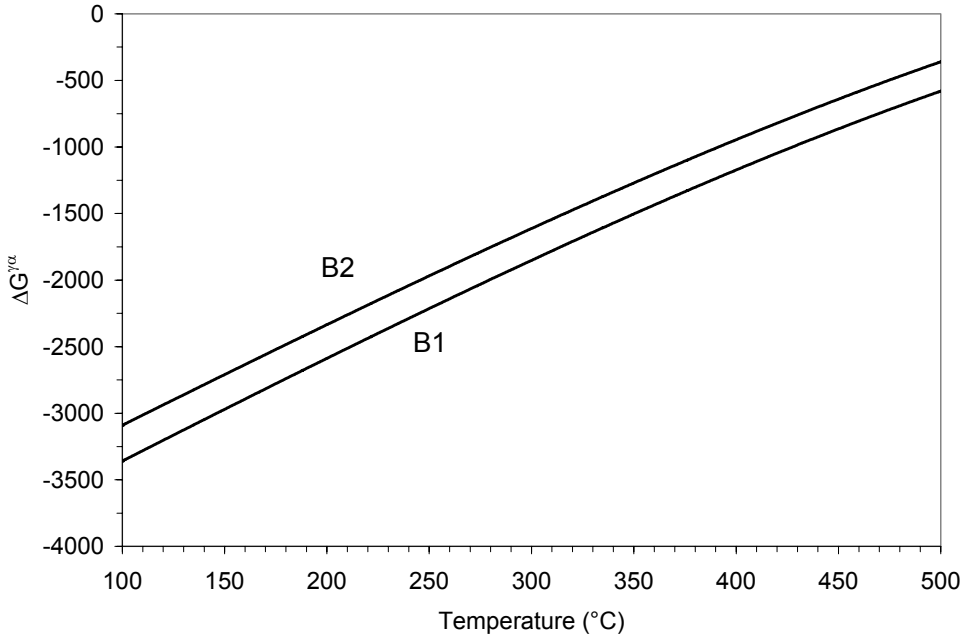

Fig. 5.8 Variation of the free energy change $\Delta G^{\gamma\alpha}$ with temperature for alloys B1 and B2.

5.4 Microstructural Features

5.4.1 Observed Phases

The micrographs in **Figs. 5.9** and **5.10** show the typical structure obtained after the isothermal transformation of austenite into bainitic ferrite. LePera etchant was used to differentiate the polygonal ferrite within the acicular ferrite aggregates (see **Figs. 5.9c** and **Fig. 5.9d**). As clearly to be seen in **Figs. 5.9** and **5.10** it is not possible to distinguish individual ferrite plates within the thin aggregates using the LOM. Therefore, SEM investigations had been conducted. **Figs. 5.11** and **5.12** show that the ferrite aggregates built up from many ferrite plates in the same crystallographic orientation.

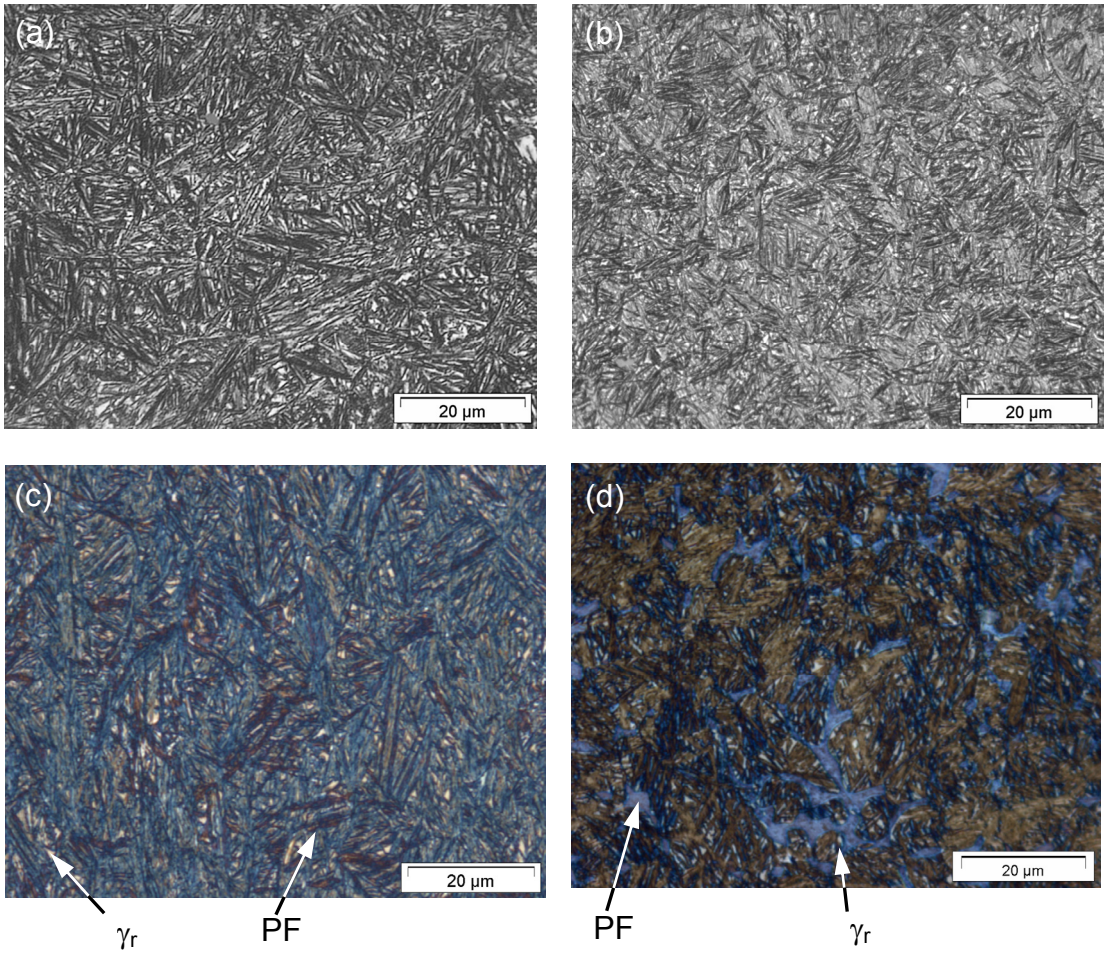

Fig. 5.9 Microstructure of alloy B1 formed by annealing at 920°C and isothermal transformation at: (a) 290°C (b) 250°C (nital etchant)), and by isothermal transformation at 250°C and austempering at (c) 870°C and (d) 830°C (LePera etchant). (PF: polygonal ferrite and γ_r: retained austenite).

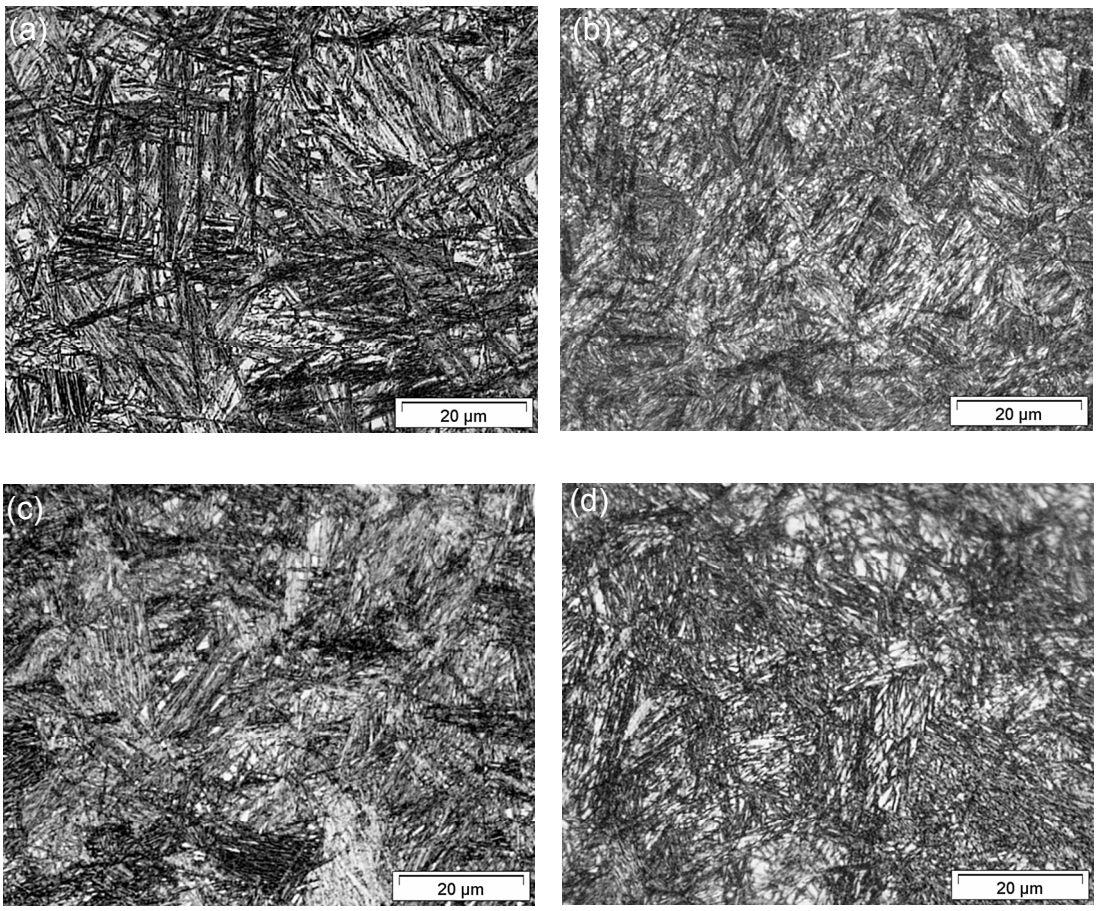

Fig. 5.10 Microstructure of alloy B2 formed by annealing at 920°C and isothermal transformation at: (a) 290°C (b) 250°C, (c) 230°C and (d) 210°C.

A decrease in the transformation temperature leads to a structure refinement, i.e. a reduction in the packet width and in the thickness of individual ferrite plates. Sandvik et al. have reported that the thickness of individual ferrite plates at a certain temperature is relatively uniform, regardless of the transformation time, while acicular-ferrite aggregate width is affected by the transformation time [San81].

The retained austenite is present in a form of homogenously distributed films along ferrite plate boundaries as well as in a form of small isolated austenite colonies. The polygonal-ferrite phase is easily distinguishable within the intercritically-annealed structure.

For the intercritically annealed material, the frequent observation of the retained austenite islands in the neighbourhood of the polygonal ferrite (cf. **Figs. 5.9c**, **5.9d**, **5.11c** and **5.11d**) can be justified by the stabilisation of the austenite particles as a result of the matrix constrains resulting from the partially coherent nature of the ferrite austenite interface [Rig79].

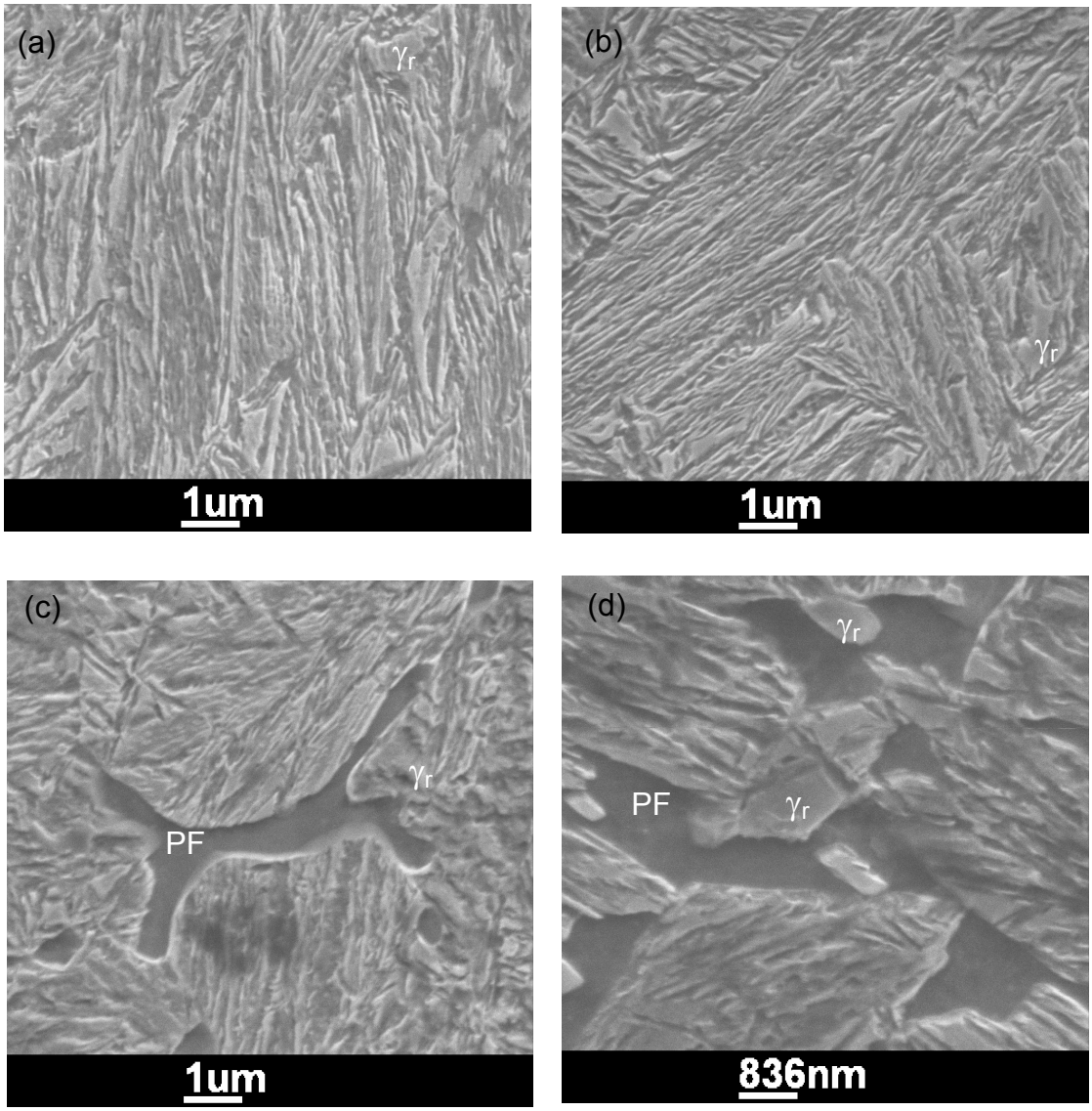

Fig. 5.11 Scanning electron micrographs of alloy B1- the microstructure is formed by annealing at 920°C and isothermal transformation at: (a) 290°C (b) 250°C, (c) annealing at 850°C and isothermal transformation at: (c) 250°C and (d) 230°C (PF: polygonal ferrite and γ_r: retained austenite).

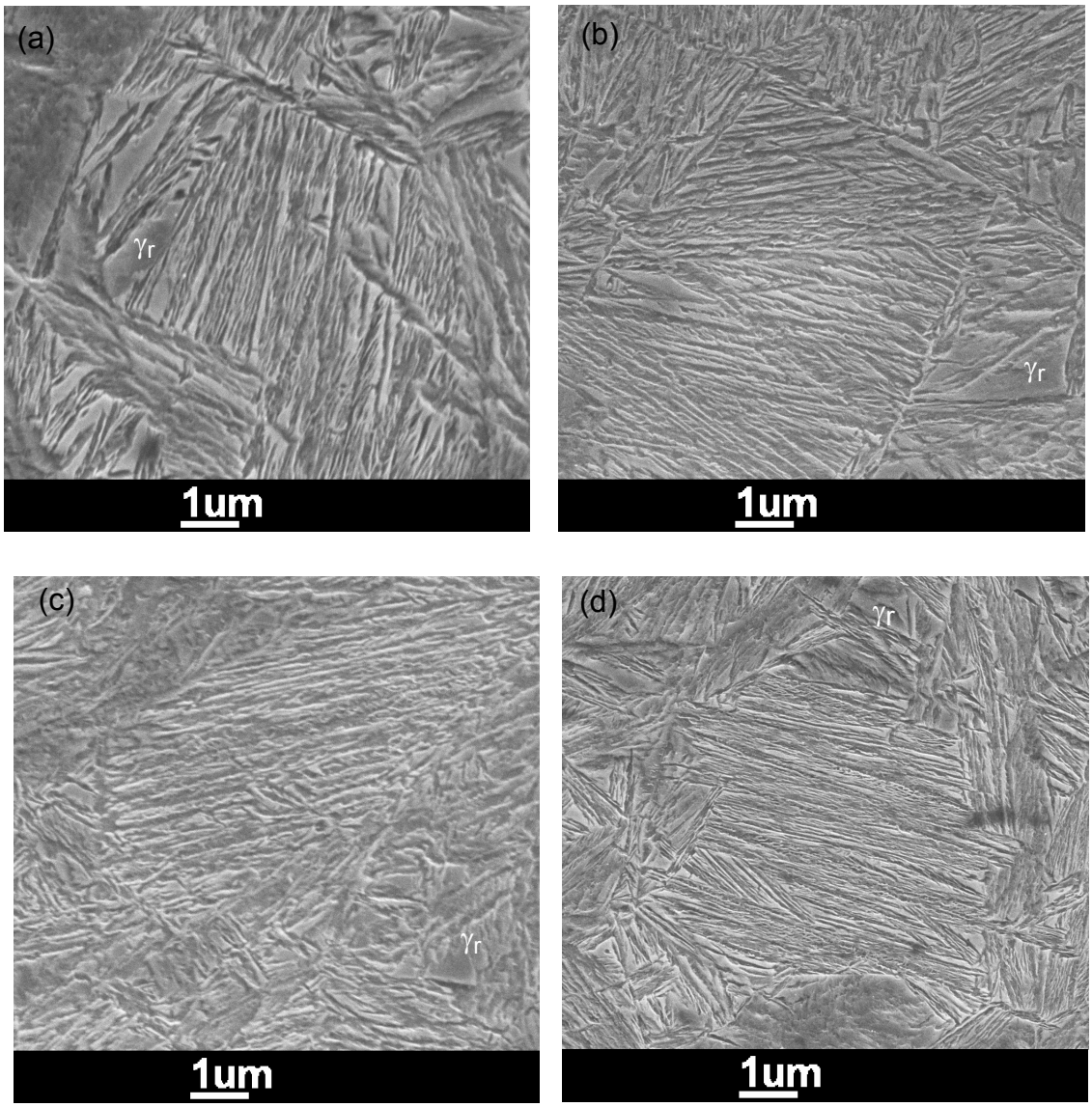

Fig. 5.12 Scanning electron micrographs of alloy B2 – the microstructure formed by annealing at 920°C and isothermal transformation at: (a) 290°C (b) 250°C, (c) 230°C and (d) 210°C (γ_r: retained austenite).

The existence of retained austenite islands, which have lower mechanical stability, in the vicinity of the soft polygonal-ferrite phase is of vital importance for the mechanical properties. In a recent publication, the authors have revealed the importance of the effect of polygonal ferrite and the interaction between polygonal ferrite, retained austenite, and strain-induced martensite during straining on the structure-property relationship [Jac01b].

5.4.2 Structure Fineness

SEM investigations were conducted on alloy B1 annealed at two temperatures of 920°C and at 850°C and on alloy B2 annealed at 920°C to determine the true

plate thickness “t”. This has been done by measuring the mean linear intercepts “L_t” in a direction normal to the plate length. The thickness t is related to L_t by the relationship $t = 2L_t/\pi$ [Gar03b].

Fig. 5.13 compares the plate thicknesses for the investigated structures. The strength of the austenite from which the ferrite plates are formed is the main factor controlling the plate thickness [Sin98]. As expected, the plates become thinner for the alloy with higher carbon content and with decreasing the transformation temperature due to the effect of both factors on enhancing the strength of the austenite. The observed thinner plate for alloy B1 annealed at 850°C in comparison with that annealed at 920°C is due to the carbon enrichment of the intercritical austenite, γ_i, during intercritical annealing at 850°C. This enrichment strengthens the γ_i from which bainitic ferrite is formed.

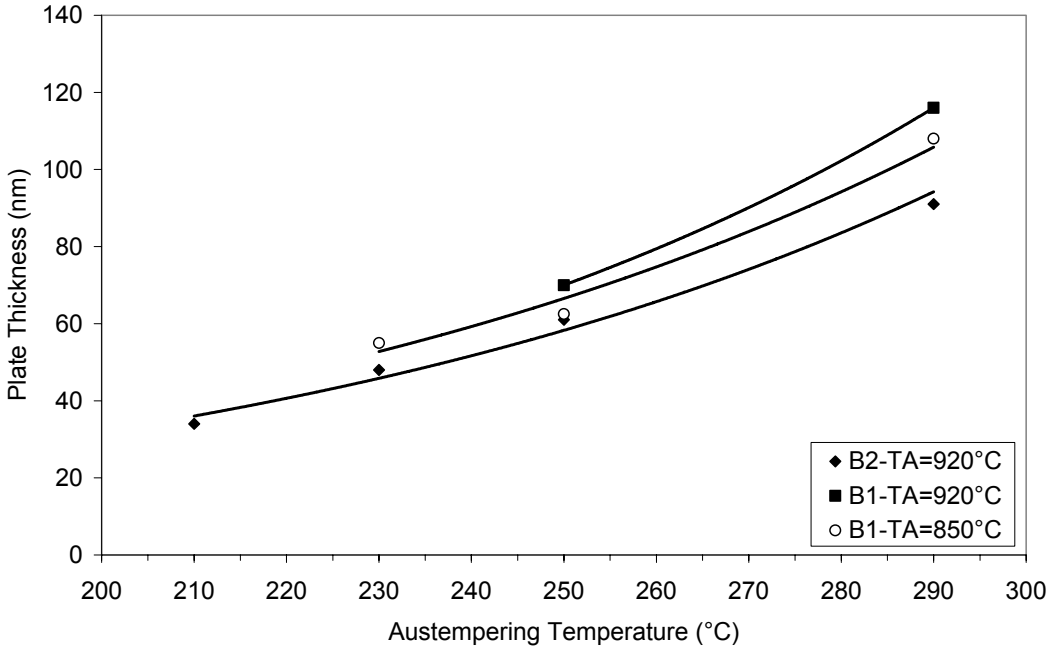

Fig. 5.13 Bainite plate thickness dependence on the transformation temperature.

5.4.3 Retained Austenite

X-ray analysis was used to estimate the retained austenite volume percentage, V_γ, and its carbon content, C_γ. **Fig. 5.14** shows representative results of the observed x-ray diffraction patterns.

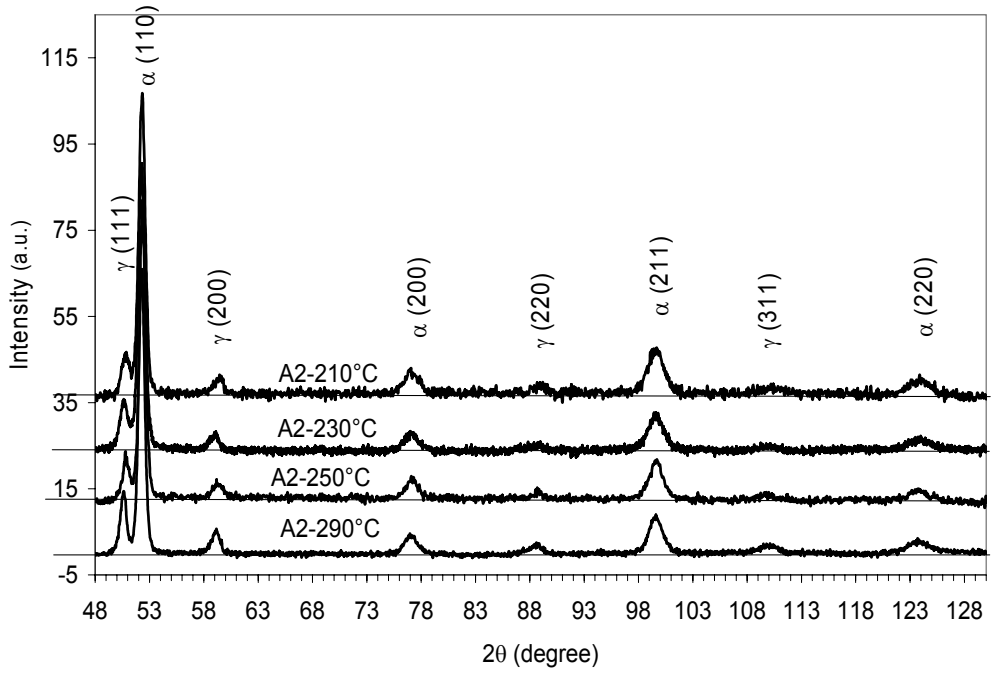

Fig. 5.14 XRD patterns for alloy B2- austenitized at 920°C and austempered at the prescribed temperatures.

The lattice parameter was calculated from the experimental peak position results. In order to estimate the "true" lattice parameter a_γ free from systematic random errors, plots were conducted of the calculated lattice parameter for each peak *vs*. $\cos^2\theta/\sin\theta$, thereby accounting for possible sample displacement in the diffractometer [Cul01]. The a_γ was determined from the y-intercept of a linear least-square fit through the data. **Fig. 5.15** shows a representative example of the method applied to alloy B2. The retained austenite carbon content, C_γ, was calculated by substituting a_γ in eq. (3.5).

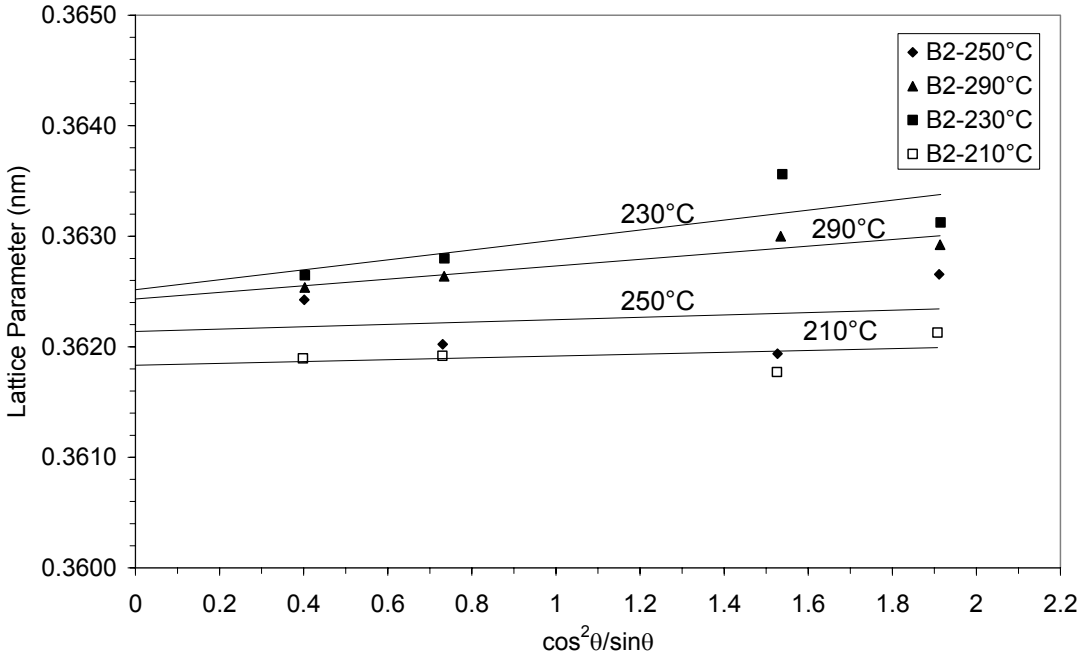

Fig. 5.15 Austenite lattice *vs*. the $\cos^2\theta/\sin\theta$ function for alloy B2-austenitized at 920°C.

Fig. 5.16 shows the influence of the bainitic holding temperature on the volume percentage of the retained austenite, V_γ, observed for both of alloys.

A comparison of experimentally measured C_γ against the calculated T_0 curve is shown in **Fig. 5.17**. During the course of the isothermal bainitic transformation, austenite is enriched with carbon, which is rejected from the bainitic acicular-ferrite. This reaction can take place only until reaching the point at which the free energy of ferrite equals the free energy of austenite (the T_0 boundary). At this point no further transformation of austenite to ferrite can take place. For lower transformation temperatures the reaction can proceed to higher carbon concentrations in austenite and consequently to higher amounts of bainite and lower amount of retained austenite.

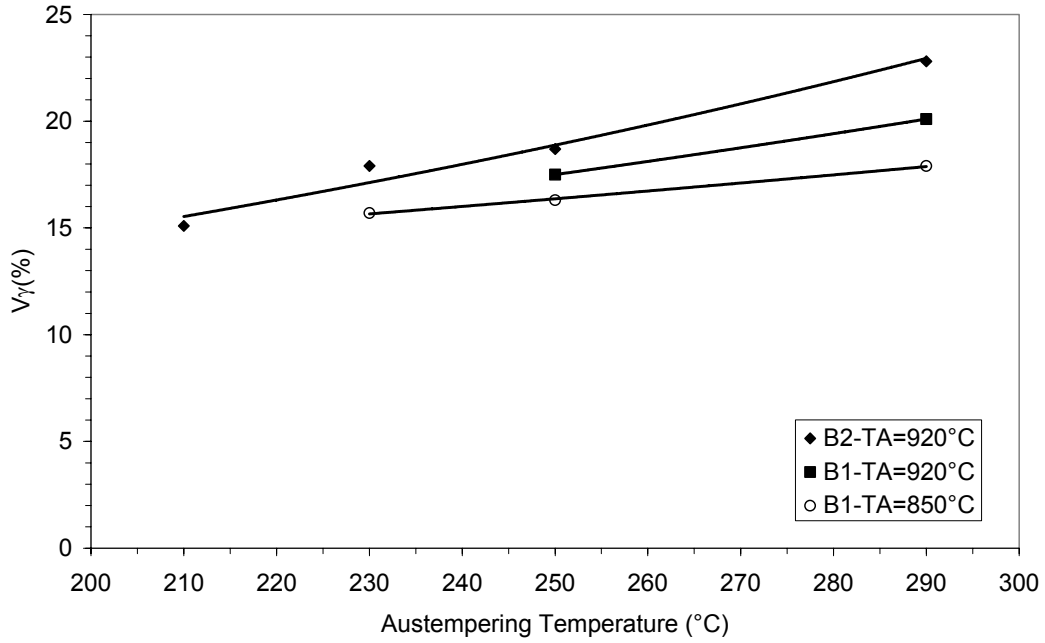

Fig. 5.16 Volume percentage of retained austenite as a function of the isothermal transformation temperature.

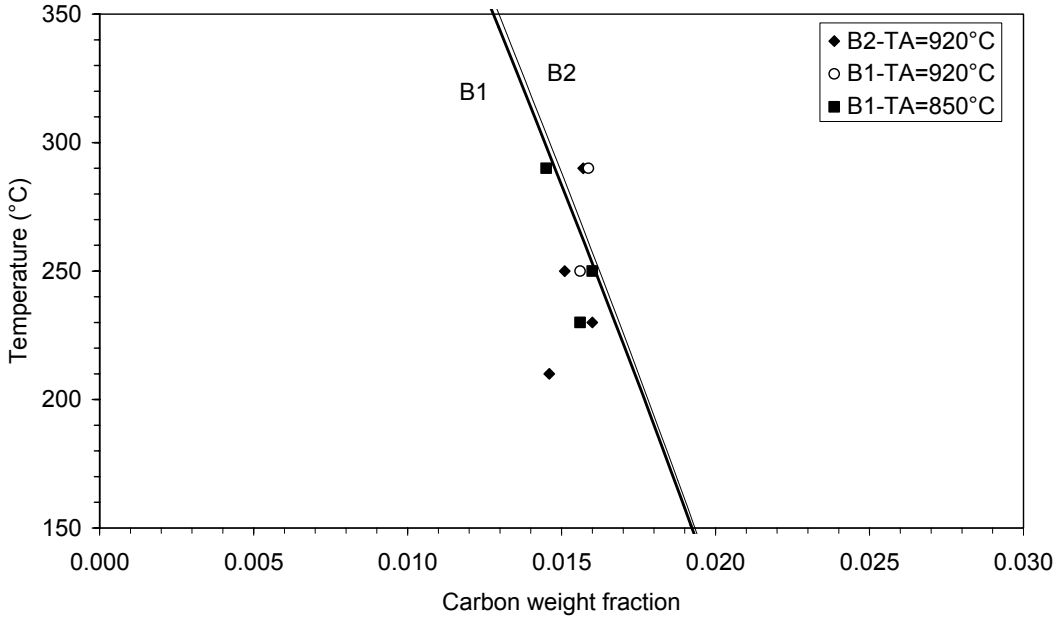

Fig. 5.17 A comparison of experimental carbon content data against the calculated T_0 curve.

On the other hand, decreasing the carbon content does not result in a significant change in the T_0 curve position, indicating that there is no significant variation in the maximum amount of carbon that can enrich the austenite at different bainitic

holding temperatures. One consequence of that is the increase of the bainite on the expense of the retained austenite by decreasing the alloy carbon content ($\overline{C}$) according to equation:

$$C_\gamma = \overline{C} + \mathrm{V_b}\frac{(\overline{C} - s)}{(1 - \mathrm{V_b})},$$

where *s* is the amount of carbon in the bainitic ferrite and V_b is the bainite volume fraction.

The previous analysis explains why the alloy B1 has proceeded to higher final amount of bainite compared with alloy B2 considering the same transformation temperature (**Figs. 5.5a**, **5.5c** and **5.6**).

For this type of steel, a relatively higher dislocation density was reported due to the transformation which is attributed to the fact that the shape deformation accompanying displacive transformations is accommodated partially by plastic relaxation [Gar05, Bha90]. Another reported fact is that as the transformation temperature decreases the amount of the formed bainite and hence the dislocation density increases [Gar05]. Atomic probe analysis of the carbon distribution in the structure revealed that a substantial quantity of carbon is trapped at these dislocations [Cab07, Pee04]. In the light of that, the deviation of the measured C_γ from the T_0 curve towards lower values, as the temperature decreases (**Fig. 5.17**), can be explained. The dependence of the redistribution of carbon between the solid solution and dislocations on the dislocation density, which is getting higher by decreasing the temperature, could be the reason for such deviation.

5.5 Mechanical Testing

5.5.1 Compression Properties

The bulk elastic and plastic deformation characteristics of polycrystalline materials are generally the same in compression and tension. As a result, the elastic modulus, yield strength and work hardening curves will be similar in compression and tension tests. Fracture strength, ultimate strength and ductility, on the other hand, depend on localized mechanisms of deformation and fracture, and are generally different in compression and tension testing [Asm00].

The mechanical properties for alloys B1 and B2 determined by the compression test are shown in **Figs. 5.18** and **5.19**. The very high strength of the materials corresponds to their very fine structure.

Lowering the transformation temperatures increases the ultimate compression strength which corresponds to a reduction in the ferrite-plates thickness together with a decrease in the volume fraction of the retained austenite. The results shown in **Fig. 5.18** indicate that the compression strength is controlled by the work-hardening properties of the austenitic structure component. The important results which can be concluded from **Fig. 5.18** is that the negative effect of the retained austenite content could be partially absorbed by the use of the strain hardening of a designed amount of ferrite in the structure. Together with the well known strong work-hardening effects caused by transformation induced plasticity (TRIP) effect, the existence of the retained austenite/transformed-martensite in the vicinity of the soft polygonal-ferrite (**Figs. 5.9c**, **5.9d**, **5.11c** and **5.11d**) can remarkably reduce its detrimental effect.

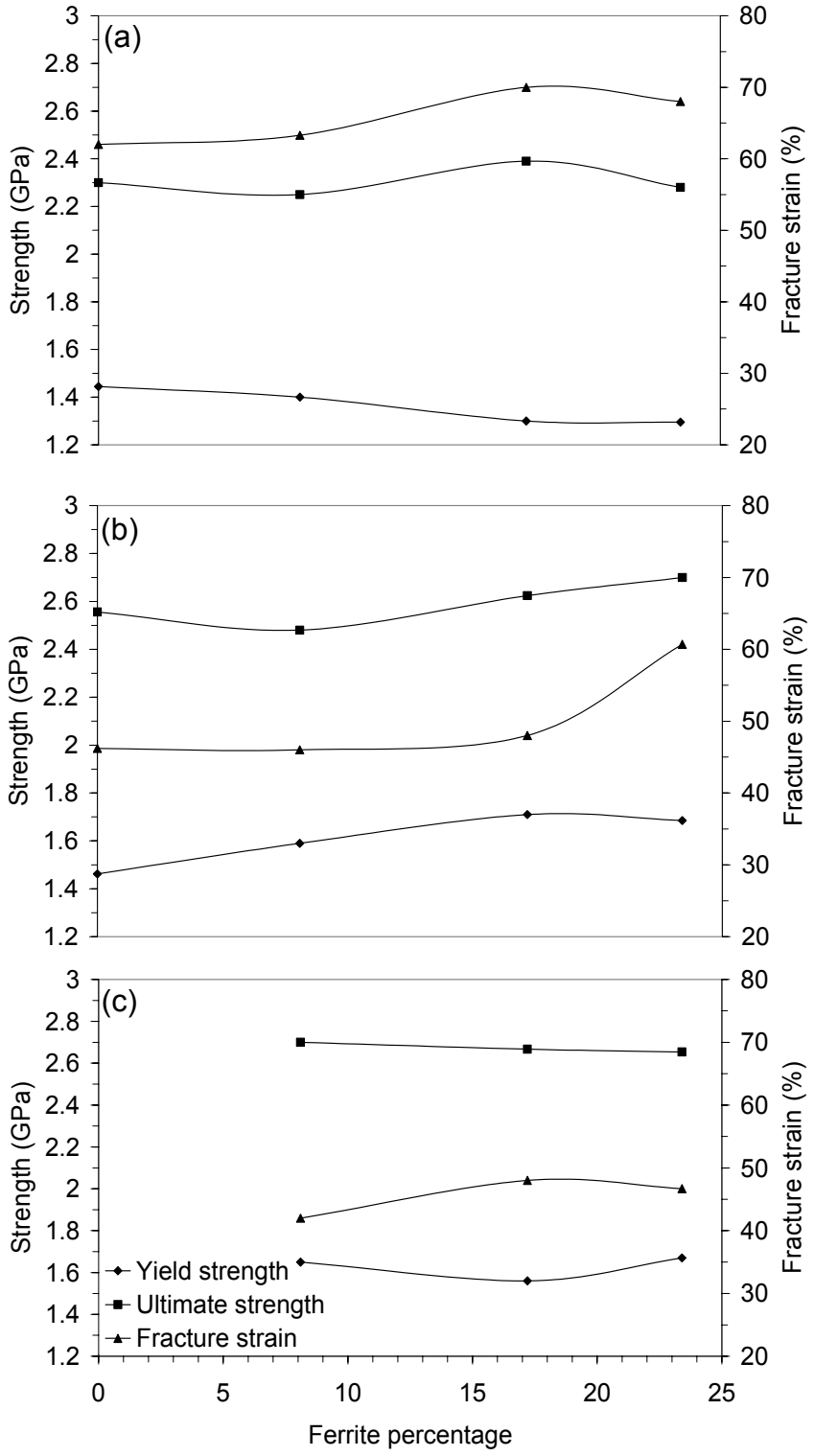

Fig. 5.18 Polygonal ferrite content dependence of the compression properties for alloy B1 isothermally treated at (a) 290°C, (b) 250°C and (c) 230°C.

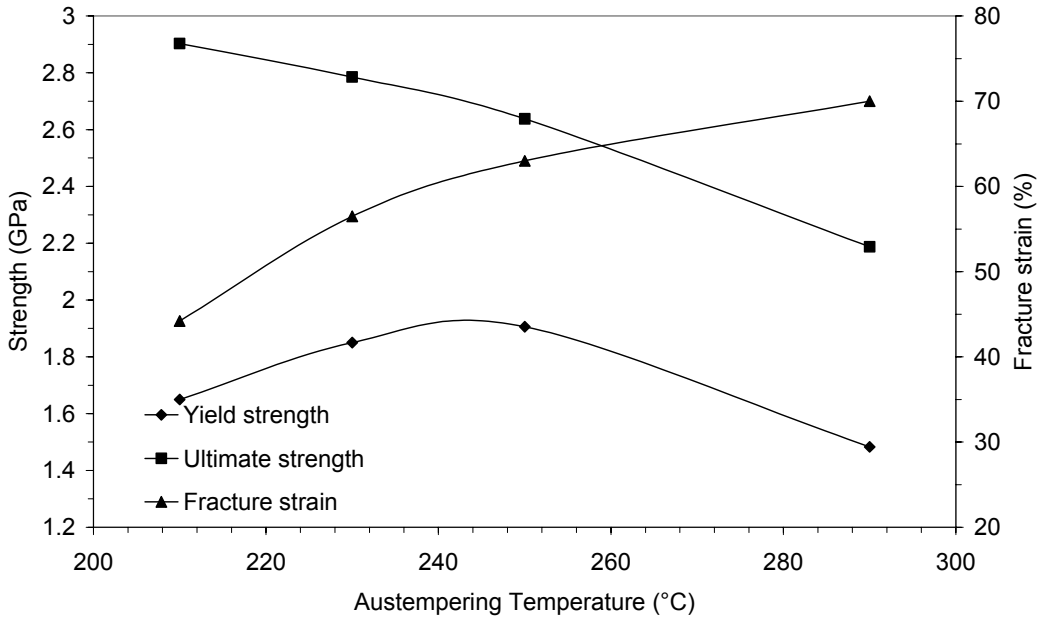

Fig. 5.19 Austempering temperature dependence of the compression properties for alloy B2.

5.5.2 Fracture Strain

During the current study, the axial compression testing has been used for comparing the *ductile fracture limits* of the material. This has been done by taking the advantage of the barrel formation and controlled stress and strain conditions at the equator of the barrelled surface when compression is carried out with friction. When friction exists at the die contact surfaces, material at the contact surfaces is retarded from moving outward while the material at the mid-plane is not constrained. As a result, barrelling occurs, as shown in **Fig. 5.20**. Under these conditions, for a given axial compressive strain, the bulge profile provides circumferential strain at the equator that is greater than the strain that occurs during homogenous compression (without friction). At the same time, due to the bulge profile, the local compressive strain at the equator is less than the strain that would have occurred during homogeneous compression. These stress and strain conditions lead to tensile stress around the circumference and reduce compressive stress at the bulge equator. Eventually, the surface is cracked due to the *tensile stress* in the circumferential direction at the bulge surface [Kuh73, Asm00].

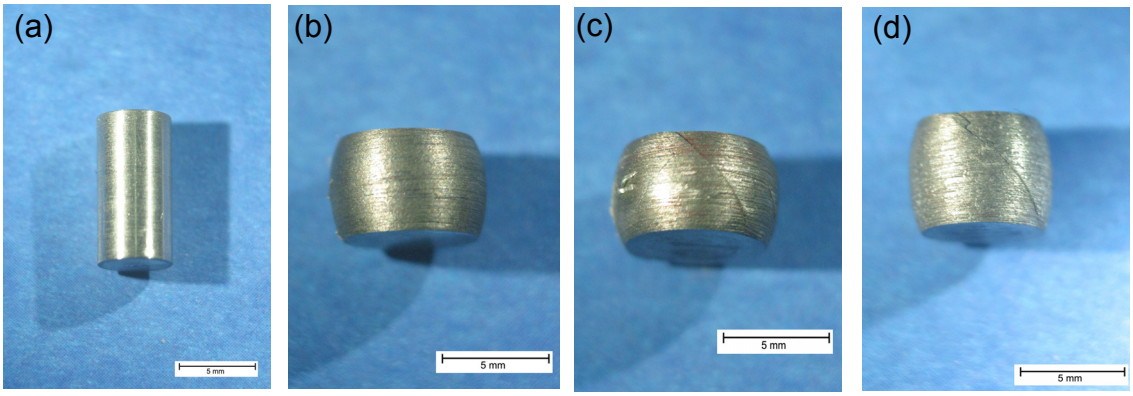

Fig. 5.20 Compressive test specimens of alloy B1, (a) undeformed specimen, (b)-(d) different responses of the samples according to their different ductilities. (b) ε = 50%-no cracks, (c) ε=50%-crack started and (d) ε = 40%-crack started.

It is clear from **Figs. 4.18 and 4.19** that the highest fracture strain values have been recorded for the highest bainite transformation temperature and the highest amount of ferrite. Ferrite serves to enrich the austenite with carbon, which helps to strengthen the bainite but it decreases its amount. In addition, the presence of ferrite in the final microstructure provides good ductility, i.e. deformation to fracture.

5.6 Conclusions

Ultra fine bainite structure had been obtained in two hypo-eutectoid steels by isothermal transformation at low temperatures (210-290°C). The major conclusions drawn from the present investigation are as follows:

1- Using the dilatometric analysis, a clear differentiation between pearlite dissolution process and $\alpha \rightarrow \gamma$ transformation was found in these steels. This allowed selecting the most appropriate intercritical temperature to obtain microstructures with optimum combination of mechanical properties.

2- Lowering the carbon content below the eutectoid composition provided the possibility of intercritical annealing of the alloy which resulted in a wider window of mechanical properties.

3- The redistribution of carbon between the retained austenite and dislocations was observed to be dependant on the dislocations density.

4- The negative effect of the retained austenite content could be partially accommodated by the use of the strain hardening of a designed amount of ferrite in the structure.

5- Axial compression testing is a useful technique for measuring the ductile fracture limits of a material. Measuring the ductile fracture limits takes advantage of the barrel formation and controlled stress and strain conditions at the equator of the barrelled surface when compression is carried out with friction.

Chapter 6
Summary

This work provides a detailed study of stabilisation of retained austenite by isothermal bainitic transformation aimed at further development of new categories of these steels in terms of strength and ductility via affordable addition of alloying elements together with optimisation of the processing routes.
Within the framework of the present study two groups of steels were investigated. In the first group, two Mo-Nb microalloyed TRIP steels with moderate aluminium content of 0.23 and 0.64 wt% and with carbon content of 0.25 wt% had been cast. The material was hot rolled using different schedules which were selected according to the non-recrystallisation temperature and additionally cold rolled. Thereafter, the specimens were intercritically annealed to obtain 30%, 50%, 70% polygonal ferrite content at the end of this process. The intercritical annealing temperatures were chosen on the basis of the dilatometric measurements. Subsequently, the material was quenched into a salt bath at different austempering temperatures. Dilatation tests under similar conditions to that of the heat treatment were also conducted to study the transformation behaviour. The microstructures had been investigated using light optical microscopy (LOM) and scanning electron microscope (SEM). The amount of retained austenite was determined by magnetometry.
It was possible to refine the cold-rolled TRIP-aided steel structure by controlling the deformation temperature and the degree of deformation below non-recrystallisation during the hot-rolling process. This structure refinement resulted in improving the strength-ductility balance. On the other hand, the intercritical annealing temperature has no significant effect on the grain size of ferrite and retained austenite.
A wide spectrum of mechanical properties was obtained mainly as a result of varying heat-treatment parameters, and to the less extent due to employing different hot-rolling schedules. The best strength-ductility balance and hence the highest formability index is recorded for the materials annealed to 50% polygonal ferrite.
It was found that increasing the aluminium content enhances the rate of transformation and increases the total amount of bainite fraction on the expense

of the retained austenite. The latter effect enhances formability through increasing the ductility.

In the second group, ultra-fine, carbide-free bainitic structure of plate thickness between 34 and 116 nm was obtained by low temperature austempering process of two hypo-eutectoid steels having 0.42 and 0.56 wt% of carbon. It was found that decreasing the carbon content results in accelerating the bainite transformation reaction together with decreasing the content of retained austenite, which is known to be detrimental to the mechanical properties. Furthermore, lowering the carbon content below the eutectoid composition allowed intercritical annealing of the material which resulted in a wider window for heat treatment parameters and consequently in a spread field for mechanical properties. Dilatometric measurements were used to find the suitable heat-treatment parameters including an estimation of the required time intervals for the cessation of the bainitic reaction. The final-structure was characterised using LOM, SEM and X-ray diffractometry. In order to investigate the effect of the microstructure parameters on the materials mechanical properties, compression tests had been conducted at room temperature.

For both groups of steels, through optimising composition and processing routes, a spectrum of mechanical behaviours was observed, outperforming many commercially available steel grades. The results had been verified by performing the thermodynamic calculations.

References:

[Aar06] H.I. Aaronson, W.T. Reynolds, Jr., G.R. Pury: The Incomplete Transformation Phenomenon in Steel, Met. Trans., 37A (2006), 1731-1745

[Aar90] H.I. Aaronson, W.T. Reynolds, Jr., G.J. Shiflet, G. Spanos: Bainite Viewed Three Different Ways, Met. Trans., 21A (1990), 1343-1380

[Ang04] J. Angeli, A.C. Kneissl: Charakterisierung von Dual-Phasen- und TRIP-Stählen mittels Nanohärte und Röntgendiffraktometrie, Z. Metallkd. 95 (2004) 7, 601-606

[Asm00] ASM Handbook, Vol. 8, Mechanical Testing and Evaluation, ASM International, Materials Park, OH 44073, (2000), 146

[Ast04] ASTM STANDARDS A 1033-04 2, “Practice for Quantitative Measurement and Reporting of Hypoeutectoid Carbon and Low-Alloy Steel Phase Transformations”, ASTM Int., USA, (2004)

[Bai93] D. Q. Bai, S. Yue, W. P. Sun, J.J. Jonas: Effect of Deformation Parameters on the No-Recrystallization Temperature in Nb-Bearing Steels, Metall. Trans., 24A (1993), 2151-2159

[Bar02] L. Barbé, L. Tosal-Martínez, B.C. De Cooman: Effect of Phosphorus on the Properties of a Cold Rolled and Intercritically Annealed TRIP-aided Steel, Proc. Int. Conf. on TRIP-Aided High Strength Ferrous Alloys, Gent, (2002), 147-151

[Bar88] R. Barbosa, F. Boratto, S. Yue, J.J. Jonas: Proc. Microstructure and Properties of HSLA Steels, ed. by A. J. DeArdo, Minerals, Mater. & Met. Soc. AIME, Warrendale, USA, (1988), 51

[Bas99a] A. Basuki, E. Aernoudt: Effect of Deformation in the Intercritical Area on the Grain Refinement of Retained Austenite of 0.4C TRIP Steel, Scr. Mater., 40 (1999), 1003-1008

[Bas99b] A. Basuki, E. Aernoudt: Influence of Rolling of TRIP Steel in the Intercritical Region on the Stability of Retained Austenite, J. Mater. Proc. Tech., 89-90 (1999), 37-43

[Bau81] H. Baumgart, H. F. de Boer, F. Heisterkamp, „Proceedings of the International Symposium on Niobium“, AIME, Warrendale, Pa, 1981, 883

[Bel04] H. Beladi, G.L. Kelly, A. Shokouhi, P.D. Hodgson, The Evolution of Ultrafine Ferrite Formation Through Dynamic Strain-induced Transformation, Mater. Sci. Eng., A 371 (2004), 343–352

[Bha01] H.K.D.H. Bhadeshia: (Bainite in Steel), IOM commercial Ltd, London, 2nd Edition, 2001

[Bha90] H.K.D.H. BHADESHIA, J.W. CHRISTIAN: Bainite in Steel, Metall. Trans., 21A (1990), 767-797

[Ble02] W. Bleck: Using the TRIP Effect - The Dawn of a Promising New Group of Cold Formable Sheets, Proc. Int. Conf. on TRIP-Aided High Strength Ferrous Alloys, Gent, (2002), 13-23

[Ble04] W. Bleck, E. Kechagias, J. Ohlert, J. Christen, A. Moulin, H. Hofmann, T.W. Schaumann: Optimisation of Microstructure in Multiphase Steels Containing Retained Austenite, Final Report, Technical Steel Research Series, Luxembourg, 2004

[Bou98] M. Bouet, J. Root, E. Es-Sadiqi, S. Yue: Effect of Mo in Si-Mn Nb Bearing TRIP Steels, Materials Science Forum, 284-286 (1998), 319-326

[Boz78] R.M. Bozorth: Ferromagnetism, Lucent Technologies Inc. IEEE Press, New York (1978)

[Bra77] J.R. Bradley, J.M. Rigsbee, H.I. Aaronson: Growth Kinetics of Grain Boundary Ferrite Allotriomorphs in Fe-C Alloys, Metall. Trans, 8A (1977), 323-333

[Bra93] M.L. Brandt, G.B. Olson: Bainitic Stabilization of Austenite in Low Alloy Steels, Iron Steelmaker, 5 (1993), 55-60

[Cab02] F. G. Caballero, H. K. D. H. Bhadeshia, K. J. A. Mawella, D. G. Jones, P. Brown: Very Strong Low Temperature Bainite, Mater. Sci. Technol., 18 (2002), 279-284

[Cab04] F.G. Caballero, H.K.D.H. Bhadeshia: Very Strong Bainite, Current Opinion in Solid States and Materials Science, 8 (2004), 251-257

[Cab07] F.G. Caballero, M.K. Miller, S.S. Babu, C. Garcia-Mateo: Atomic Scale Observations of Bainite Transformation in a High Carbon High Silicon Steel, Acta Mater., 55 (2007), 381-390

[Cap05] C. Capdevila1, F. G. Caballero, C. García De Andrés: Neural Network Model for Isothermal Pearlite Transformation. Part II: Growth Rate: ISIJ Int., 45 (2005), 238-247

[Che89] H.C. Chen, H. Era, M. Shimizu: Effect of Phosphorus on the Formation of Retained Austenite and Mechanical Properties in Si-Containing Low-Carbon Steel Sheet: Met. Mat. Trans., 20A (1989), 437-445

[Chr01] M. Christophe, J.Z. Zhao, V. Sven, B.C. DeCooman: An Improved Method for Determining the Continuous Cooling Transformation Diagram of C-Mn Steels, Steel res., 72 (2001) 7, 263-270

[Cul01] B.D. Cullity, S.R. Stock: Elements of X-ray Diffraction, Pearson/Prentice Hall, Inc., (2001)

[Dat81] D.P. Datta, A.M. Gokhale: Autenitization Kinetics of Pearlite and Ferrite Aggregates in a Low Carbon Steel Containing 0.15 wt pct C, Metall. Mater. Trans., 12A (1981), 443–450

[Dav 30] E.S. Davenport, E.C. Bain: Trans. AIME, 90 (1930), 117

[De03] A.K. De, J.G. Speer, D.K. Matlock: Color Tint-Etching for Multiphase Steels, Advanced Materials and Processes, 161 (2003), 27-30

[Dec99] M. DeMeyer, D. Vanderschueren, B.C. DeCooman: The Influence of the Substitution of Si by Al on the Properties of Cold Rolled C-Mn-Si TRIP Steels, ISIJ Int., 39 (1999) 8, 813-822

[Del65] J. Deliry: Mem. Sci. Rev Metall., 7-8 (1965), 524

[Dem02] M. De Meyer, J. Mahieu, B.C. De Cooman: Empirical Microstructure Prediction Method for Combined Intercritical Annealing and Bainitic Transformation of TRIP steel, Mater. Sci. Technol., 10 (2002), 1121-1132

[Egh06] B. Eghbali, A. Abdollah-zadeh: Influence of Deformation Temperature on the Ferrite Grain Refinement in a Low Carbon Nb–Ti Microalloyed Steel, Journal of Materials Processing Technology, 180 (2006), 44-48

[Ema06] E. Emadoddin, A. Akbarzadeh, Gh. Daneshi: Effect of Intercritical Annealing on Retained Austenite Characterization in Textured TRIP-Assisted Steel Sheet, Mater. Charact., 57 (2006), 408–413

[Pet01] R. Petrov, L. Kestens, Y. Houbaert: Recrystallization of a Cold Rolled Trip-assisted Steel during Reheating for Intercritical Annealling, ISIJ Int., 41(2001) 8, 883-890

[Gar02] FC. Garcı´a de Andre´s, F.G. Caballero, C. Capdevila, L.F. Alvarez: Application of Dilatometric Analysis to the Study of Solid–Solid Phase Transformations in Steels, Mater. Charact., 48 (2002), 101-111

[Gar03] C. Garcia-Mateo, F.G.Caballero, H.K.D.H. Bhadeshia: Acceleration of Low-temperature Bainite, ISIJ Int., 43 (2003), 1821-1825

[Gar03a] C. Garcia-Mateo, F.G. Caballero, H.K.D.H. Bhadeshia: Development of Hard Bainite, ISIJ Int., 43 (2003) 8, 1238-1243

[Gar05] C. Garcia-Mateo, F.G. Caballero: Ultra-high-strength Bainitic Steels, ISIJ Int., 43 (2003) 11, 1821-1825

[Gar98] C. Garcı´a de Andre´s, F.G. Caballero1, C. Capdevila1, H.K.D.H. Bhadeshia: Modelling of Kinetics and Dilatometric Behavior of Non-Isothermal Pearlite to Austenite Transformation in an Eutectoid Steel, Scr. Mater., 39 (1998) 6, 791-796

[Gir01] E. Girault, A. Metens, P. Jacques, Y. Houbaert, B. Verlinden, J. Van Humbeeck: Comparison of the Effect of Silicon and Aluminium on the Tensile Behaviour of Multiphase TRIP-Assisted Steels, Scr. Mater., 44 (2001), 885-892

[Gir98] E Girault, P Jacques, Ph. Harlet, K Mols, J Van Humbeeck, E Aernoudt, F. Delannay: Metallographic Methods for Revealing the Multiphase Microstructure of TRIP-Assisted Steels, Mater. Char., 40 (1998), 111-118

[God02] S. Godet, Ph. Harlet, F. Delannay, P.J. Jacques: Effect of Hot-Rolling Conditions on the Tensile Properties of Multiphase Steels Exhibiting a TRIP Effect, Proc. Int. Conf. on TRIP-Aided High Strength Ferrous Alloys, Gent, (2002), 135-140

[Gom03] M. Gómez, S. F. Medina, G. Caruana: Modelling of Phase Transformation Kinetics by Correction of Dilatometry Results for a Ferritic Nb-microalloyed Steel, ISIJ Int., 43 (2003) 8, 1228-1237

[Has04] S. Hashimoto, S. Ikeda, K. Sugimoto, S. Miyake: Effects of Nb and Mo Addition to 0.2%C-1.5%Si-1.5%Mn Steel on Mechanical Properties of Hot Rolled TRIP-aided Steel Sheets, ISIJ Int., 44 (2004) 9, 1590-1598

[Has06] K. Hase, C. Garcia-Mateo, H.K.D.H. Bhadeshia: Bimodal Size-distribution of Bainite Plates, Mater. Sci. Eng. A, 438-440(2006), 145-148

[Heh72] R.F. Hehmann, K.R. Kinsman, H.I. Aaronson: A Debate of Bainite Reaction, MT, 3 (1972), 1077-1094

[Jac01a] P.J. Jacques, E. Girault, A. Mertens, B. Verlinden, J. van Humbeek, F. Delannay: The Development of Cold-rolled TRIP-assisted Multiphase Steels. Al-alloyed TRIP-assisted Multiphase Steels, ISIJ Int. 9 (2001), pp. 1068-1074.

[Jac01b] P.J. Jacques, J. Ladrie` RE, F. Delannay: On the Influence of Interactions between Phases on the Mechanical Stability of Retained Austenite in Transformation-Induced Plasticity Multiphase Steels, Metall. Mater. Trans., 32A (2001), 2759-2768

[Jac04] P. Jacques: Transformation-induced Plasticity for High Strength Formable Steels, Current Opinion in Solid State and Materials Science, 8 (2004), 259-265

[Jeo85] W.C. Jeong, C.H. Kim: Formation of Austenite from a Ferrit-Pearlite Microstructure During Intercritical Annealing, J. Mater. Sci., 20 (1985) 12, 4392-4398

[Jeo92] W.C. Jeong, J.H. Chung: HSLA Steels: Processing, Properties and Applications", ed. by G. Tither and Z. Shoubua, Min., Met. And Mat. Soc., Warrendale, PA, (1992), 305-311

[Jia02] S. Jiao, F. Hassani, R.L. Donaberger, E.Essadiqi, S. Yue: The Effect of Processing History on a Cold Rolled and Annealed Mo–Nb Microalloyed TRIP Steel, ISIJ Int., 42 (2002) 3,299-303

[Kar95] L.P. Karjalainen, T.M. Maccagno, J.J. Jonas: Softening and Flow Stress Behaviour of Nb Microalloyed Steels During Hot Rolling Simulation, ISIJ Int., 35 (1995),1523-1531.

[Kim01] S.-J. Kim, C.-G. Lee, I. Choi, S. Lee: Effects of Heat Treatment and Alloying Elements on the Microstructures and Mechanical Properties of 0.15 Wt Pct C Transformation-Induced Plasticity–Aided Cold-Rolled Steel Sheets, Metall. Mater. Trans., 32A (2001), 505-514.

[Kop01] T.A. Kop, J. Sietsma, S. Van der Zwaag: Dilatometric Analysis of Phase Transformations in Hypo-eutectoid Steels, J. Mater. Sci., 36 (2001), 519-526

[Kuh73] H.A. Kuhn, P.W. Lee, T. Erturk: A Fracture Criterion for Cold Forging, J. Eng. Mater. Technol., 95 (1973), 213-218.

[Lee88] H.J. Lee, G. Spanos, G.J. Shiflet, H.I. Aaronson: Mechanisms of the Bainite (Non-Lamellar Eutectoid) Reaction and a Fundamental Distinction between the Bainite and Pearlite (Lamellar Eutectoid) Reactions, Acta Met., 36 (1988), 1129-1140.

[Lep80] F. S. LePera: Improved Etching Technique to Emphasize Martensite and Bainite in High-Strength Dual Phase Steel, Journal of Metals, 32 (1980), 38-39

[Leslie] W.C. Leslie, G.C. Rauch: Precipitation of Carbides in Low-Carbon Fe-Al-C Alloys, Met. Trans., 9A (1978), 343-349

[Mah02a] J. Mahieu, B.C. De Cooman, J. Maki, S. Claessens: Hot-Dip Galvanizing of Al Alloyed TRIP Steels, Iron & Steelmaker, 29 (2002), 29-34

[Mah02b] J. Mahieu, B.C. De Cooman, J. Maki: Phase Transformation and Mechanical Properties of Si-Free CMnAl Transformation-Induced Plasticity-Aided Steel, Metall. Mater. Trans., 33A (2002), 2573-2580

[Mak03] J. Maki, J. Mahieu, B.C. De Cooman, S. Claessens: Galvanisability of Silicon Free CMnAl TRIP steels, Mater. Sci. Technol., 19 (2003), 125–131

[Mar01] L. Tosal-Martiez, D. Vanderschueren, S. Jacobs, S. Vandeputte: Development of Hot Rolled Nb-bearing Si-TRIP Steel with Excellent Fatigue Behaviour for Automotive Applications, Steel Res. , 72 (2001) 10, 412-415

[Mat04] H. Matsuda, H.K.D.H. Bhadeshia: Kinetics of the Bainite Transformation, Proc. R. Soc. Lond. A, 460 (2004), 1707–1722

[Mat87] O. Matsumura, Y. Sakuma, H. Takechi: Enhancement of Elongation by Retained Austenite in Intercritical Annealed 0.4C-1.5Si-0.8Mn steel, Trans. ISIJ, 27 (1987) 7, 570-579

[Mey02] M. De Meyer, J. Mahieu, B.C. De Cooman: Empirical Microstructure Prediction Method for Combined Intercritical Annealing and Bainitic Transformation of TRIP Steel, Mater. Sci. Technol., 18 (2002) 10, 1121-1132

[Mey99] M. De Meyer, D. Vanderschueren, B.C. De Cooman: The Influence of the Substitution of Si by Al in the Properties of Cold Rolled C-Mn-Si TRIP Steels, ISIJ Int. 8 (1999), 813-822

[Min01] B. Mintz: Hot Dip Galvanizing of Transformation Induced Plasticity and Other Intercritically Annealed Steels, International Materials Reviews, 46 (2001), 169-197

[Ohl02] J. Ohlert, W. Bleck, K. Hulka: Control of Microstructure in TRIP Steels by Niobium, Proc. Int. Conf. on TRIP-Aided High Strength Ferrous Alloys, Gent, (2002), 199-206.

[Ohl03] J. Ohlert: Einfluss von Chemisher Zusammensetzung und Herrstellungsverlauf auf Mikrostruktur und Mechanische Eigenschaften von TRIP-Stählen, Dissertation, Shaker Verlag, Aachen, 2003.

[Pal07] H. Palkowski, M. Soliman, G. Kugler: Effect of Thermomechanical Processing Parameters on Bakehardening Ability of Hot Rolled Dual Phase Steels, Proc. TMS Annual Meeting & Exhibition, Orlando, USA, 2007.

[Pan95] R. Pandi, M. Militzer, E.B. Hawbolt T.R. Meadowcroft: Proc. Int. Symp. on Phase Transformations During the Thermal/Mechanical Processing of Steels, Vancouver, ed. by E.B. Hawbolt, S. Yue, CIM, Montreal, (1995), 459

[Pea67]W. B. Pearson: A Hand Book of Lattice Spacings and Structure of Metals and Alloys, volume 2, Pergamon Press, London, 1967

[Pee04] M. Peet, S.S. Babu, M.K. Miller, H.K.D.H. Bhadeshia: Three-dimensional Atom Probe Analysis of Carbon Distribution in Low-Temperature Bainite, Scr. Mater., 50 (2004) 10, 1277-1281

[Pol39] H. Polly: Approach of Magnetization to Saturation in Nickel, Ann. Physik, 36 (1939) 5, 625-650

[Pot90] M. Pott-Langemeyer, W. Riehemann, W. Heye: Magnetic Properties of Meltpsun Fe-Si-Al-Ribbons, Anales de Fisica, B86 (1990), 232-234

[Pri94] G.L. Prior: The Role of Dilatometry in the Characterisation of Steels, Mater. Forum, 18 (1994), 265-276.

[Qu02] J.B. Qu, Y.Y. Shan, M.C. Zhao, K. Yang: Effects of Hot Deformation and Accelerated Cooling on Microstructural Evolution of Low Carbon Microalloyed Steels, Mater. Sci. Tech., 18 (2002), 145–150.

[Ram01] D. Ramin, W. Riehemann: Automatic Measurements of the Magnetic Properties of Extreme Soft Magnetic Ferromagnetic Materials, Technisches Messen, 68 (2001) 3, 116-125

[Ray82] S.K. Ray, S. Mishra, O.N. Mohanty: TEM Study of Carbide Precipitation in a Phosphorus-Bearing Low-Carbon Steel, Scr. Met., 16 (1982), 43-47

[Ree92] G.I. Rees, H.K.D.H. Bhadeshia: Bainite Transformation Kinetics: Part I Modified Model, Mater. Sci. Technol., 8 (1992), 985-993

[Rig79] J.M. Rigsbee, P.J. VanderArend, Laboratory Studies of Microstruture and Strucure-Property Relationships in Dual-Phase HSLA Steels, in Formable HSLA Steels, AT Davenport, ed., TMS-AIME, (1979), 56-86.

[Rob29] J.M. Robertson: J. Iron and Steel Inst., 119 (1929), 391-419

[Sak91] Y. Sakuma, O. Matsumara, H. Takechi: Mechanical Properties and Retained Austenite in Intercritically Heat-Treated Bainite-Transformed Steel and Their Variation with Si and Mn Additions, Metall. Mater. Trans., 22A (1991) 2, 489-498

[Sak92] Y. Sakuma, D.K. Matlock, G. Krauss: Intercritically Annealed and Isothermally Transformed 0.15 Pct C Steels Containing 1.2 Pct Si-1.5 Pct Mn and 4 Pct Ni. II : Effect of Testing Temperature on Stress-Strain Behavior and Deformation-Induced Austenite Transformation, Metall. Mater. Trans., 23A (1992) 4, 1233-1241

[San81] B.P.J. Sandvik, H.P. Nevalainen: Structure-Property Relationship in Commercial Low-Alloy Bainitic-Austenitic Steel with High Strength, Ductility, and Toughness, Met. Technol., June (1981), 213-220

[San85] S. Sangal, N.C. Geol, K. Tangri: A Theoretical Model for the Flow Behavior of Commercial Dual-Phase Steels Containing Metastable Retained Austenite: Part II. Calculation of Flow Curves, Metall. Trans. A, 16A (1985) 11, 2023-2029

[Shi06] W. Shi, L. Li, C. Yang, R. Fu, L. Wang, P. Wollants: Strain-Induced Transformation of Retained Austenite in Low-Carbon Low-Silicon TRIP Steel containing Aluminium and Vanadium, Mater. Sci. Eng. A, 429 (2006), 247-251

[Sin98] S.B. Singh, H.K.D.H. Bhadeshia: Estimation of Bainite Plate-Thickness in Low-Alloy Steels, Mater. Sci. Eng. A, 245 (1998), 72-79.

[Str05] A.M. Streicher-Clarke, J.G. Speer, D.K. Matlock , B.C. De Cooman, D.L. Williamson: Analysis of Lattice Parameter Changes Following Deformation of a 0.19C-1.63Si-1.59Mn Transformation Induced Plasticity Sheet Steel, Metall. Mater. Trans., A36 (2005) 4, 907-918.

[Sug06] K. Sugimoto, T. Muramatsu , S. Hashimoto, Y. Mukaid: Formability of Nb Bearing Ultra High-Strength TRIP-aided Sheet Steels: Journal of Materials Processing Technology, 177 (2006), 390–395

[Sug92a] K. Sugimoto, M. Kobayashi, S. Hashimoto: Ductility and Strain-Induced Transformation in a High-Strength Transformation-Induced Plasticity-Aided Dual-Phase Steel, Metall. Mater. Trans., 23A (1992), 3085-3091

[Sug92b] K. Sugimoto, N. Usui: Effects of Volume Fraction and Stability of Retained Austenite on Ductility of TRIP-aided Dual Phase Steels, ISIJ Int., 32 (1992) 12, 1311-1318

[Sur98] C. Suryanarayanam: X-ray diffraction: A Practical Approach, Plenum Press, New York, 1998.

[Tak89] M. Takahashi, H.K.D.H. Bhadeshia: The Interpretation of Dilatometric Data for Transformations in Steels, Journal of Materials Science Letters, 8 (1989), 477-478

[Tak90] M. Takahashi, H.K.D.H. Bhadeshia: A Model for the Transition from Upper to Lower Bainite, Mater. Sci. Tech., 6 (1990) , 592-603

[Tim02] L.B. Timokhina, P.D. Hodgson, E.V. Pereloma: Effect of Alloying Elements on the Microstructure-Property Relationship in Thermomechanically Processed C-Mn-Si TRIP steels, Steel Res., 73 (2002) 6-7, 274-279

[Tim04] L.B. Timokhina, P.D. Hodgson, E.V. Pereloma: Effect of Microstructure on the Stability of Retained Austenite in Transformation-Induced-Plasticity Steels, Metall. Mater. Trans., 35A (2004) 8, 2004-2331

[Tra02a] S. Traint: Phase transformations and mechanical properties of low alloyed dual-phase and TRIP-steels, Dissertation, VDI Verlag, Düsseldorf, 2002

[Tra02b] S. Traint, A. Pichler, K. Hauzenberger, P. Stiaszny, E. Werner: Influence of Silicon, Aluminium, Phosphorus and Copper on the Phase Transformations of Low Alloyed TRIP-steels, Proc. Int. Conf. on TRIP-Aided High Strength Ferrous Alloys, Gent, (2002), 121-127

[Tse87] D. Tseng, Q. Y. Long, K. Tangri: An Acoustic Emission Study of Martensitic Transformation of Retained Austenite in Intercritically Annealed HSLA Steels, Acta Metall., 35 (1987) 7, 1887-1894

[Uls01] ULSAB Advance Vehicle Concepts, Technical Transfer Dispatch #6, ISIJ, Brussels, May 2001.

[Van84] G.F. Vander Voort: Metallography: Principles and Practice, McGraw-Hill, 1984

[Wan95] J-J Wang, H-S Fang, Z-G Yang, Y-K Zheng: Fine Structure and Formation Mechanism of Bainite in Steels, ISIJ Int., 35 (1995) 8, 992-1000

[Wir02] E. Wirthl, A. Pichler, R. Angerer, P. Stiaszny, K. Hauzenberger, Y.F. Titovets, M. Hackl: Determination of the Volume Amount of Retained Austenite and Ferrite in Small Specimens by Magnetic Measurements, Proc. Int. Conf. on TRIP-Aided High Strength Ferrous Alloys, Gent, (2002), 61-64

[Zac67] V.F. Zackay, E.R. Parker, D. Fahr, R. Bush: The Enhancement of Ductility in High-Strength Steels., T. Am. Soc. Metal., 60 (1967), 252-259

[Zae04] S. Zaefferer, J. Ohlert, W. Bleck: A Study of Microstructure, Transformation Mechanisms and Correlation Between Microstructure and Mechanical Properties of a Low Alloyed TRIP Steel, Acta Mat., 52 (2004) 9, 2765-2778

[Zar95] A. Zarei-Hanzaki, P.D. Hodgson, S. Yue: Hot Deformation Characteristics of Si-Mn TRIP Steels with and Without Nb Microalloy Additions, ISIJ Int., 5 (1995), 324-331

[Zha01a] J.Z. Zhao, C. Mesplont, B.C. De Cooman: Kinetics of Phase Transformations in Steels: A New Method for Analysing Dilatometric Results, ISIJ Int., 41 (2001) 5, 492-497

[Zha01b] L. Zhao, N.H. Van Dijk, E. Brueck, J. Sietsma, S. Van der Zwaag: Magnetic and X-ray Diffraction Measurements for the Determination of Retained Austenite in TRIP Steels, Mat. Sci. Eng. A, 313 (2001) 1, 145-152

[Zha02a] L. Zhao, J. Moreno, S. Kruijver, J. Sietsma, S. Van der Zwaag: Influence of Intercritical Annealing Temperature on Phase Transformations in a High Aluminium TRIP Steel, Proc. Int. Conf. on TRIP-Aided High Strength Ferrous Alloys, Gent, (2002), 141-145

[Zha02b] L. Zhao, T.A. Kop, V. Rolin, J. Sietsma, A. Mertens, P.J. Jacques, S. Van der Zwaag: Quantitative Dilatometric Analysis of Intercritical Annealing in a Low-Silicon TRIP steel, J. Mater. Sci., 37 (2002), 1585-1591

[Zha98] M.-X. Zhang, P.M. Kelly: Determination of Carbon Content in Bainitic Ferrite and Carbon Distribution in Austenite by Using CBKLDP, Mater. Charact., 40 (1998), 159-168

Eidesstattliche Erklärung

Hiermit erkläre ich an Eides statt, dass ich die vorliegende Arbeit selbständig ohne unerlaubte Hilfe verfasst und die benutzten Hilfsmittel vollständig angegeben habe und noch keine früheren Promotionsversuche unternommen habe.

Mohamed Soliman

Bisher sind erschienen:

Band	Verfasser / Titel
1/01	Thorsten Anke Bake Hardening von warmgewalzten Mehrphasenstählen
1/02	Günther Lange Beitrag zum Umformverhalten von dreischichtigen austenitischen Sandwichverbunden mit polymerer Kernschicht
1/03	Mohamed Soliman Phase Transformation and Mechanical Properties of New Austenite-Stabilised Bainite Steels
3/01	Markus Krieger Mechanical properties and bake hardening behaviour of cold rolled dual phase steels subjected to advanced galvanising process routes
3/02	Michail Popov Enhancement of mechanical properties of different Magnesium alloys due to grain refinement by severe plastic deformation processing
3/03	Udo Brüx Mikrostrukturen und Eigenschaften ultrahochfester Leichtbaustähle auf der Basis Fe-Mn-Al-C

Band X / yy

X: 1 Metallurgie und Werkstoffumformung
2 Polymerwerkstoffe und Werkstofftechnik
3 Werkstoffkunde und Werkstofftechnik
4 Nichtmetallisch-anorganische Werkstoffe

yy: fortlaufende Nummer

ISBN 3-923605-58-7